Order Number 9108086

# Spectroscopic studies of the structure and orientational effects of electroresponsive polymeric and Langmuir-Blodgett films

Chen, Jiming, Ph.D.

City University of New York, 1990



U·M·I
300 N. Zeeb Rd.
Ann Arbor, MI 48106

# SPECTROSCOPIC STUDIES OF THE STRUCTURE AND ORIENTATIONAL EFFECTS OF ELECTRORESPONSIVE POLYMERIC AND LANGMUIR-BLODGETT FILMS

by

**Jiming Chen**

A dissertation submitted to the Graduate Faculty in Physics in partial fulfillment of the requirements for the degree of Doctor of Philosophy, The City University of New York.

1990

This manuscript has been read and accepted for the Graduate Faculty in Physics in satisfaction of the dissertation requirement for the degree of Doctor of Philosophy.

| | |
|---|---|
| 5/15/90 | Marten L. denBoer |
| Date | Chair of Examining Committee |
| 5/15/90 | Joel I. Gersten |
| Date | Executive Officer |
| | Terje A. Skotheim |
| | Steve Greenbaum |
| | Robert A. Marino |
| | Myriam Rafailovich |
| | Supervisory Committee |

The City University of New York.

**Abstract**

**SPECTROSCOPIC STUDIES OF THE STRUCTURE AND ORIENTATIONAL EFFECTS OF ELECTRORESPONSIVE POLYMERIC AND LANGMUIR-BLODGETT FILMS**

by

Jiming Chen

Advisor: Professor Marten L. denBoer

The microscopic structure, bond length, orientation, and coordination number of a series of electroresponsive molecular and polymeric systems were studied by several spectroscopic techniques: Extended X-ray Absorption Fine Structure (EXAFS) spectroscopy, Near-Edge X-ray Absorption Fine Structure (NEXAFS) spectroscopy, X-ray diffraction, and Fourier-Transform Infra-Red (FTIR) spectroscopy. The studies concern ion complexation in poly(ethylene oxide), and the structure and orientation of pyrrole and thiophene based Langmuir-Blodgett (LB) films and electrochemically polymerized poly(3-methylthiophene) films. The temperature dependence of the coordination number of oxygen around the cation $K^+$ in the ion-conducting polymer complex of poly(ethylene oxide) and potassium iodide was studied with EXAFS and NEXAFS spectroscopies. NEXAFS spectroscopy also is a sensitive probe of the orientational behavior of LB films. The relative intensities of the absorption peaks from the core level ground state to $\sigma^*$ and $\pi^*$ anti-bonding states at different incident angles of the x-ray beam can be used to calculate the orientation of the

molecules. In the near-edge C *K*-edge spectra of various LB films, a charge transfer interaction between a polymer film and its metallic substrate was also observed. The layer structure and in-plane structure of LB films were studied by x-ray diffraction. A clear superlattice structure was observed in Y-type LB films. The temperature dependance of the structure of LB film also was studied by x-ray diffraction. The orientation and ordering of thin films of the electron conducting polymer poly(3-methylthiophene) were also studied by NEXAFS, and FTIR spectroscopic techniques. The results of the NEXAFS and the FTIR experiments are consistent.

In memory of

my father, Lian-Kang Chen

**Acknowledgements**

I would like to express my gratitude to Prof. Marten L. denBoer, my thesis advisor, and Dr. Terje A. Skotheim, my supervisor, for their close guidance, support and encouragement during this thesis work as well as for my personal growth.

I thank Prof. R. Marino, Prof. S. Greenbaum and Prof. M. Rafailovich.

I also want to thank Dr. X. Q. Yang who has always been helpful during my thesis work for the past three years and H. S. Lee who has provided various chemical compounds for preparing LB films as well as sharing his knowledge of chemistry.

I thank Prof. M. Rubner's group at MIT and Prof. S. Tripathy's group at Lowell University for providing LB films and for interesting discussions on sample preparation.

I want to express my appreciation to C. L. Lin, D. Fischer, D. Chapman, S. Ehrlich, and to Cornell University Light Source for their support on the beamline works at NSLS and at CHESS.

Finally, I want to express my great appreciation to my mother, my family, my uncle, and all of my friends for their constant support and inspiration in my life.

This work was supported by the Division of Materials Science, U. S. Department of Energy under contract No. DE-AC02-76CH00016.

**Table of Contents**

**List of Tables**

**List of Figures**

# Chapter 1. Introduction

In modern society, polymers provide the necessities and the amenities of life. Some polymers are found in nature in the form of wood, hide, wool, cotton, silk, and rubber. Others are synthetic and are used in our everyday life in the form of plastics, fibers, rubbers, packaging material, writing paper, paints, and coatings. Polymers such as carbohydrates, proteins, and nucleic acids are fundamental to the biological sustenance of life and are the essence of life itself.

Although polymeric substances have been used by humans for many centuries and although the structural principles of organic chemistry were developed in the 1850s, it is only relatively recently that the polymer concept has been recognized and accepted. The possibility that covalent structures comprising thousands of atoms could exist as stable, well-defined entities was not easily conceived. Part of the difficulty was that what we now recognize as polymers could not be readily analyzed by the prevailing classical methods of chemistry. In the second half of the nineteenth century and the early part of the twentieth, the study of polymers was virtually neglected since they could not be easily purified by the accepted methods of distillation and crystallization. Polymers were thought of as a collection of small molecules held together by some peculiar and mysterious intermolecular forces not present in the simpler compounds of low molecular weight.

At about this time physical and physical-chemical methods of analysis were being developed and were achieving a respectability comparable to the more classical methods. Through the Herculean efforts of a few pioneers, notably H. Staudinger in Germany, the

polymer concept began to emerge and to be gradually, although in some instances grudgingly, accepted. By the mid-1940s the study of polymers was well on its way to becoming the quantitative science that it is today. The acceptance of the concept that polymers are true molecular species of very high molecular weight is the primary reason that great advances have been made recently in the chemistry and physics of these substances.[1]

In recent years, polymer science has played a more and more important role in science and technology. A great deal of research has been done on numerous polymeric materials. Both electroactive polymers (semiconductor or conjugated polymer) and ion conducting polymer electrolytes, as new classes of polymer materials, are of interest to polymer scientists, physicists, and chemists for practical application such as chemical or biological sensors, polymer electrolytes, for high energy density storage batteries, and nonlinear optical systems.

## 1.1. Ion Conducting Polymeric Materials (PEO/KI)

Charged polymers are salt-bearing solvating polymer complexes. They are known to be solid solutions of a salt in the polymer since the work of Wright.[2,3] The starting point for Wright's research was polyethylene oxide (PEO), which forms solid-state complexes with various alkaline salts as a result of cation solvation by the polymer. Wright also pointed out that these complexes can have precise stoichiometries and that they are ion conducting, which means that cations and anions are the charge carriers. These complexes have triggered the recent development of polymer electrolytes now being studied in various electrochemical devices, including rechargeable lithium batteries.

Other charged complexes of the type: polymer + salt + solvent have been known for a long time. However, in these complexes the polymer does not necessarily contribute

to the conductivity. Rather, it tends to take the role of a gelling agent, and conductivity is provided by the salt dissolved in the liquid electrolyte. These systems are sometimes applied in aqueous-electrolyte batteries and have also been proposed for lithium batteries.[4] Their electrochemical performance is essentially the same as that of liquid electrolytes.

Ion conducting solids have been the object of intense study motivated by the possibility of electrochemistry without inconvenient liquid solvents. Historically, solid-state ion conductivity has been studied primarily in inorganic materials, such as β-alumina and silver salts.[5,6] However, since the discovery of ionic conductivity in poly(ethylene oxide) (PEO) complexed with alkali-metal salts,[2,7] research on this class of materials has grown rapidly. An important near-term application is the fabrication of high-energy-density rechargeable lithium batteries. However, the relationship between ionic conductivity and the microscopic structure of polymer-salt complexes is not completely understood. Originally, it was suggested that ionic conduction in PEO was due to cation hopping within the helical PEO crystal structure, reminiscent of the hopping responsible for ion conductivity in inorganic materials. Later work showed that in the polymer complex, which consists of crystalline and amorphous phases, the ionic conductivity is associated with the amorphous phase,[8,9] not the crystalline phase. This finding implies that the conduction mechanism for this polymer complex is quite different from that for inorganic materials.

In the PEO-salt system, the alkali-metal cation and the oxygen atoms in the ether group form a complex in which the oxygen atoms construct a "cage-like" structure around the cation, leading to dissociation of the anion-cation pair.[10] However, the cage size formed by the PEO chain can be adjusted to the size of the cation by taking advantage of the high degree of flexibility of the chain. The complexation is reversible. This reversibility and conformational flexibility allow the ions to migrate from one solvating site to another,

resulting in ionic conductivity.[11] Therefore, studying the complexation is crucial for understanding the ionic conductivity. However, the absence of long-range order in the amorphous phase responsible for conductivity precludes investigations of the microscopic structure using conventional x-ray diffraction. X-ray absorption spectroscopy, on the other hand, especially near-edge x-ray absorption fine structure (NEXAFS), is sensitive to local structural properties such as interatomic spacings and coordination number, even in the absence of long-range order, and it is therefore well suited to a study of the amorphous conducting phase. In particular, by using the alkali atom as an absorber, the structure of the cation-polymer complex can be studied.

The ion transport properties of the polymer-salt complex are strongly dependent on the polymer chain. This dependency is described by the VTF (Vogel-Tamman-Fulcher) equation based on free volume theory:

$$\sigma = AT^{1/2}\exp[-E_a/(T-T_0)], \qquad (1)$$

where $E_a$ is the pseudoactivation energy, $T_0$ is related to the experimentally measured glass transition temperature $T_g$ by a constant, and A is proportional to the carrier concentration. Figure 1 shows the conductivity of PEO-KI complexes for three different concentrations of KI (n = 4, 8, 20) as a function of temperature. When the conductivity is plotted as $\ln\sigma$ versus 1/T, the slope of the curve is proportional to the pseudoactivation energy $E_a$. The change of slope around 60-80°C indicates a change of activation energy in this temperature range.

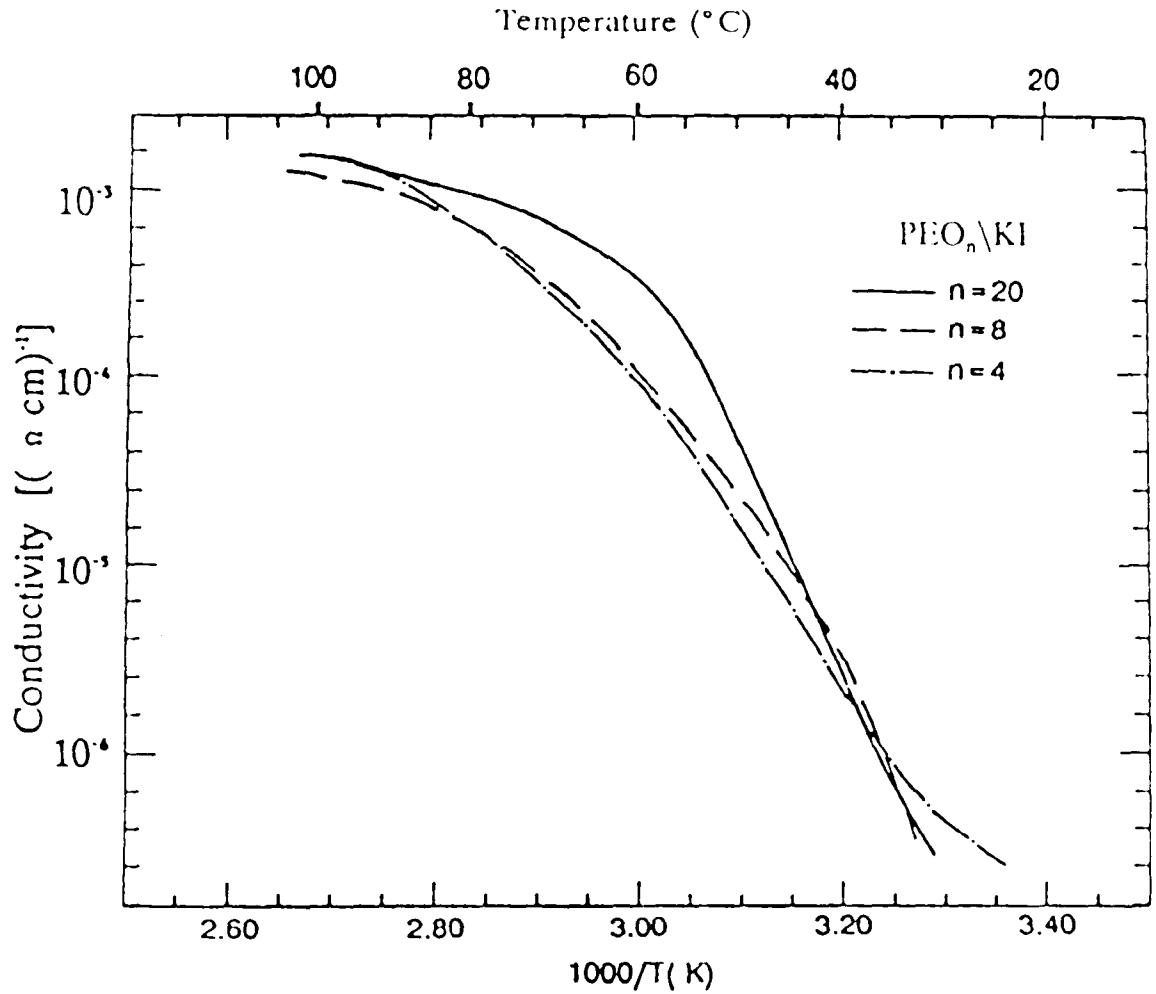


Figure 1. Ac conductivity of P(EO)$_n$-KI complexes as a function of temperature, where n = 4, 8, 20 are the ratios of oxygen atoms to potassium ions. The change of slope around 60-80°C indicates a change of activation energy in this range.

## 1.2. Langmuir-Blodgett Films

A classical dipping technique for making single layer organic films was developed by Irving Langmuir and Katharine Blodgett between 1917 and 1935. As early as 1920, Langmuir[12] reported the transfer of such molecules from a water surface onto a solid support. However, the first detailed description of sequential monolayer transfer was given fifteen years later by Blodgett.[13] These built-up monolayer assemblies are now called Langmuir-Blodgett(LB) films. The publications resulting from the pioneering experiments carried out by these two investigators from 1934 to 1952 have been summarized by Gaines,[14] whose book[15] provides a comprehensive treatment of the subject up to 1966.

In thin film technology, multilayer organic films (Langmuir-Blodgett films) have become important because of their precise thickness and the degree of control over their molecular architecture. Many investigators are interested in these Langmuir-Blodgett (LB) films which have a potentially wide range of applications, including molecular electronics, microelectronics, integrated optics, and micro-lithography. LB films, with nano-meter dimensions and a high degree of structural order, may also have broad applications in microelectronic devices on the nano-meter scale.

To transfer a monolayer of molecules from a water surface onto a solid support requires a specific substrate treatment and a high-quality floating monolayer. The surface of the substrate has to be chemically treated to become either hydrophilic or hydrophobic, depending upon the types of LB films to be made, and the quality of the floating monolayer is extremely sensitive to the ion concentration in the water subphase, the pH value of the water, and the water temperature. The dipping speed is also extremely critical to the transfer ratio. The detailed procedure for fabricating a Langmuir-Blodgett film of

monomer, polymer, or a mixture of monomer and polymer materials is provided in chapter 4, section 3: The Fabrication of Langmuir-Blodgett films.

## 1.3. Electron Conducting Polymeric Materials

The first conducting polymers were obtained by mixing insulating polymers with solid particles up to a volume fraction sufficient to induce electrical conductivity through percolation of the dispersed conductive phase. The conductive materials selected for this purpose can be carbon blacks or various metallic particles, such as stainless steel fibers. These composite plastics are used mostly as electromagnetic or radiofrequency barriers, among other applications, or for their antistatic properties.

More recently, a new category of electronic conducting polymers, so-called "conjugated unsaturated polymers",[16,17] was developed. These materials have a highly anisotropic, quasi-one-dimensional structure, which makes such systems fundamentally different from conventional inorganic semiconductors. Their chain-like structure leads to strong coupling of the electronic states to conformational excitations (solitons) peculiar to a one-dimensional system.[18] Moreover, the relatively weak interchain coupling allows diffusion of dopant molecules into the structure (between chains), while the strong intra-chain carbon-carbon bonds maintain the integrity of the polymer. The prototype example of these conducting polymers is polyacetylene, $(CH)_x$.

Polyacetylene consists of weakly coupled chains of CH units forming a pseudo-one-dimensional lattice. Three of the four carbon valence electrons are in $sp^2$ hybridized orbitals. The 120° bond angle between these three electrons can be satisfied by two possible arrangements of the carbons, trans-$(CH)_x$ and cis-$(CH)_x$, with two and four CH monomers per unit cell, respectively. In either isomer the remaining valence electron has

the symmetry of a $2p_z$ orbital, with its charge density lobes perpendicular to the plane defined by the other three. In terms of an energy band description, the $\sigma$ bonds form low-lying completely filled bands, while the $\pi$ bonds give the partially filled energy band structure responsible for the important electronic properties.

The conjugated unsaturated polymers are generally intrinsic semiconductors that can be given a metallic character by n-type ($Na^o$, $Li^o$) or p-type ($AsF_5$, $Br_2$, $FeCl_3$) chemical doping.[19] These organic metals offer many possible applications,[20] although chemical stability and processing problems have somewhat delayed their development. The use of polyacetylene and polypyrroles is now being investigated for their potential as electrode materials or as collectors in various battery configurations.[21,22]

# Chapter 2. Review of Spectroscopic Studies of Conducting Polymeric and Langmuir-Blodgett Thin Films

Many complementary spectroscopic techniques for studying the microscopic structure of conducting polymers and LB films have been developed, including infrared spectroscopy,[23,24] Raman scattering spectroscopy,[25] electron diffraction,[26] and x-ray diffraction.[27] Recently, the technique of near-edge x-ray absorption fine structure (NEXAFS) spectroscopy has been applied to the study of classical monolayer LB films of arachidic acid and cadmium and calcium arachidate.[28,29] The studies also have been performed on multilayer films, since nondestructive techniques to study monolayers are scarce. Based on the materials that we have concentrated on, the review in this chapter will be separated into three categories: ion conducting polymers, Langmuir-Blodgett films, and electron conducting polymers.

Ion Conducting Polymeric Materials

High molecular weight poly(ethylene oxide)(PEO) was studied with x-ray diffraction measurements by Sauter and his colleagues as early as 1933.[30,31] A highly crumpled helical structure of PEO was then suggested by the x-ray measurements. Twenty years later, the infrared spectra of the polymer in the amorphous and the crystalline state were used to study the configuration of the PEO chains.[32,33] By probing $CH_2$-rocking modes at 844 and 960 $cm^{-1}$, a structural picture consistent with the x-ray measurements was obtained.

The infrared spectrum of PEO complexed with low molecular weight compounds

provided more detailed information about the structure of PEO than the polymer alone.[34,35,36] More studies of PEO complexes were done by x-ray diffraction[37] as well as Raman scattering spectroscopy.[38] In the late 1960's, Koenig and his co-workers did numerous Raman studies of PEO in solutions.[39,40,41] A disordered structure was observed in the molten polymer and in chloroform solutions.

Since Wright pointed out that PEO with alkaline salt complexes are solid solutions and ion conducting,[2,3] the structure of PEO complexed with alkali-metal salts has become an object of study for polymer scientists interested in improving the ion conductivity of polymers. Besides x-ray diffraction and vibrational spectroscopy, the technique of extended x-ray absorption fine structure (EXAFS) was applied to study the local environment of cations in the $RbI(PEO)_x$ ($x=4$, 8) complexes by Catlow *et.al.*[42] They showed that the majority of the cations occupy sites of fixed geometry throughout the temperature range 80K to 453K. The Rb ions are coordinated by four oxygen atoms with the actual configuration of the Rb-O bonds being anion dependent. The four nearest oxygen neighbors are split into two short and two long Rb-O bonds. There are RbI pairs[43] in these compounds with Rb-I distances of 3.7 Å. The existence of RbI pairs has important consequences for cation and anion transport in these materials, influencing the energetics of their conductivity.

## Langmuir-Blodgett Films

The structure of Langmuir-Blodgett films has been of interest to physicists, electronic engineers, chemists, and biologists alike, because of their wide range of applications, including molecular devices, and microelectronics. However, after a LB film has been transferred to a substrate, ordering in the direction normal to the plane must be confirmed by x-ray diffraction. Since the pioneering work of Holley and Bernstein,[44,45] many studies

have been made of the structure of the lead, barium, cadmium, and silver salts of several fatty acids. An extensive investigation of x-ray diffraction from mixed fatty acid systems was made by Matsuda *et.al.*[46]

A full understanding of the three dimensional structure of LB films requires supplementary information to determine the in-plane structure, which can be studied by other techniques such as electron diffraction, neutron diffraction, infrared spectroscopy, and in-plane x-ray diffraction. The earliest studies of LB films using electron diffraction were made by Havanga and de Wael,[47] and Germer and Storks.[48] Recently, improvement of the technique allowed Bonnerot *et al*,[49] and Garoff *et al*[50] to obtain electron diffraction from monolayers of fatty acids. These studies showed that the first layer of material deposited has a hexagonal symmetry. There is a transition over the next few layers to an orthorhombic or monoclinic structure depending on the material used. Neutron diffraction was used by Nicklow *et al.*[51] to study manganese stearate with a view to observing two-dimensional magnetic ordering. Infrared Raman spectroscopy has also been used to study ordering in LB films; Recently, Knoll *et al.*,[52] and Naselli *et al.*[53] used this technique to assess the degree of order in multilayers of cadmium arachidate. They found that order within a layer decreases with the number of layers. An x-ray diffraction study at glancing angles of the in-plane structure of various LB films made by M. Prakash *et al.*[54] showed that in LB films of lead stearate, the lead atoms form plane arrays identical to one set of planes in a bulk crystal, but with little correlation between the planes.

More recently, the technique of near-edge x-ray absorption fine structure (NEXAFS) was applied to determine the orientation of arachidate chains in LB monolayers on Si(111) by Outka *et al.*[28,29] The observed NEXAFS resonances were assigned to transitions to excited states which are localized on individual $CH_2$ groups or C-C bonds. Using curve-

fitting techniques of the angular dependence of the various spectral peaks, the orientation of the hydrocarbon chains of the cadmium arachidate monolayer could be accurately determined. The hydrocarbon tails were found to be tilted by about 33° from the surface normal.

Electron Conducting Polymeric Materials

The interfaces of polymeric thin films (polythiophene, polypyrrole,...) and their metallic substrates (Pt, Ni,...) have been of major interest to physicists and polymer scientists studing the adsorption bonding to the surface. Many studies have been done on the interaction between polymers and metal surface and on the molecular geometry of polymers on metal surface, using surface science techniques such as NEXAFS,[55] x-ray photoemission spectroscopy,[56,57,58](XPS) ultraviolet photoemission spectroscopy,(UPS) infrared spectroscopy,[59] Raman spectroscopy,[60] electron spin resonance[61](ESR), low energy electron diffraction(LEED), and thermal desorption spectroscopy[62](TDS).

For example, a recent NEXAFS study of the chemisorption geometry of poly(3-methylthiophene) electrochemically deposited on Pt substrate was done by Tourillon *et al.*[63] They found that the polymeric chains are well ordered on the metallic surface, even for thicknesses up to 50 Å. In an undoped state, the polymeric layers lie flat on the Pt with a strong interaction between electron states of the metal and the antibonding $\pi^*$ band of the PMeT. When PMeT is electrochemically doped to its conducting state, the first layer lies essentially flat on Pt, while the other layers are randomly oriented. The ordering and the homogeneity of the first layers strongly depend on the electric field applied at the Pt-electrolytic medium interface during the electrochemical synthesis.

The techniques of EELS and TDS have been used to study the adsorption of pyrrole

and thiophene on Cu(100).[62] Adsorption is molecular and reversible with no evidence for dissociation. At low exposures, each molecule is weakly π-bonded to the Cu(100) surface with the molecular ring parallel to the surface plane. At higher exposures, the results with TDS and EELS suggest two different models for adsorption prior to the onset of multilayer formation. Pyrrole forms a stable second layer (bi-layer) in which the molecular rings are inclined toward the surface normal. The bi-layer and the π-bonded monolayer can be separately isolated by thermal treatment. However, thiophene appears to increase the monolayer coverage by "compression" on the Cu(100) surface, with the average tilt angle of the rings changing with coverage. At higher exposures at 85 K, multilayer condensation is initiated for all molecules.

# Chapter 3. Theories of Experimental Techniques

We applied four different types of spectroscopy to study electroactive polymeric materials: extended x-ray absorption fine structure, near edge x-ray absorption fine structure, Fourier-transform infra-red spectroscopy, and x-ray diffraction. A brief description of the theoretical foundation of these spectroscopies is given in this chapter.

## 3.1 Basic Theory of EXAFS.

Extended x-ray absorption fine structure (EXAFS) refers to the oscillations in the x-ray absorption coefficient spectrum as a function of photon energy in the energy range from about 30 eV to as far as 1000 eV above the absorption edge in an x-ray absorption spectrum.(Figure 2) This simple picture of EXAFS has been formulated theoretically and generally accepted as a short-range single-electron single-scattering theory.[64,65] This single scattering model[65,66] agrees very well with experimental results. The multiple scattering of the photoelectron is not important at these energies.[64,67,68]

EXAFS in the single scattering model is a final state interference effect, involving scattering of the outgoing photoelectron from the neighboring atoms. In the absence of neighboring atoms, a photoelectron ejected by an x-ray photon will travel as an outgoing spherical wave with a wavelength $\lambda = 2\pi/k$, where

$$k = \sqrt{\frac{2m}{\hbar^2}(E-E_0)} \qquad (2)$$

Here, E is the incident photon energy, and $E_0$ is the energy threshold of the particular absorption edge involved. In the presence of neighboring atoms, this outgoing photoelectron

can be backscattered from these atoms. Such backscattering produces an incoming wave which can interfere either constructively or destructively with the outgoing wave near the origin, resulting in an oscillatory modulation of the absorption rate ($\mu$). The amplitude and frequency of the sinusoidal modulation of $\mu$ as a function of E depends on the type (and bonding) of the neighboring atoms and their distances from the absorber.

In the single scattering approximation, for reasonably high energies ($E - E_0 \geq 60$ eV) and moderate thermal or static disorder, the modulation of the absorption rate ($\mu$) in EXAFS, normalized to the background absorption ($\mu_0$) is given by

$$\chi(E) = \frac{\mu(E) - \mu_0(E)}{\mu_0(E)} \tag{3}$$

To relate $\chi$(E) to structural parameters, it is necessary to convert the energy E into the photoelectron wavevector $k$ defined in Eq.2. This transformation of $\chi$(E) gives $\chi(k)$ in $k$ space, where

$$\chi(k) = \sum_j N_j S_i(k) F_j(k) e^{-2\sigma_j^2 k^2} e^{-2r_j/\lambda(k)} \frac{\sin(2kr_j + \phi_j(k))}{kr_j^2} \tag{4}$$

Here $F_j(k)$ is the background backscattering amplitude from each of the $N_j$ neighboring atoms of the jth type at a distance $r_j$. The Debye-Waller factor $\sigma_j$ accounts for thermal vibration (assuming harmonic vibration of the atoms) and static disorder (assuming Gaussian distribution pairs). $\phi_j(k)$ is the total phase shift experienced by the photoelectron. The term $e^{-2r_j/\lambda(k)}$ is due to inelastic losses in the scattering process (due to neighboring atoms and the intervening medium), with $\lambda$ being the electron's mean free path. $S_i(k)$ is the amplitude reduction factor due to many-body effects such as shake up and shake off

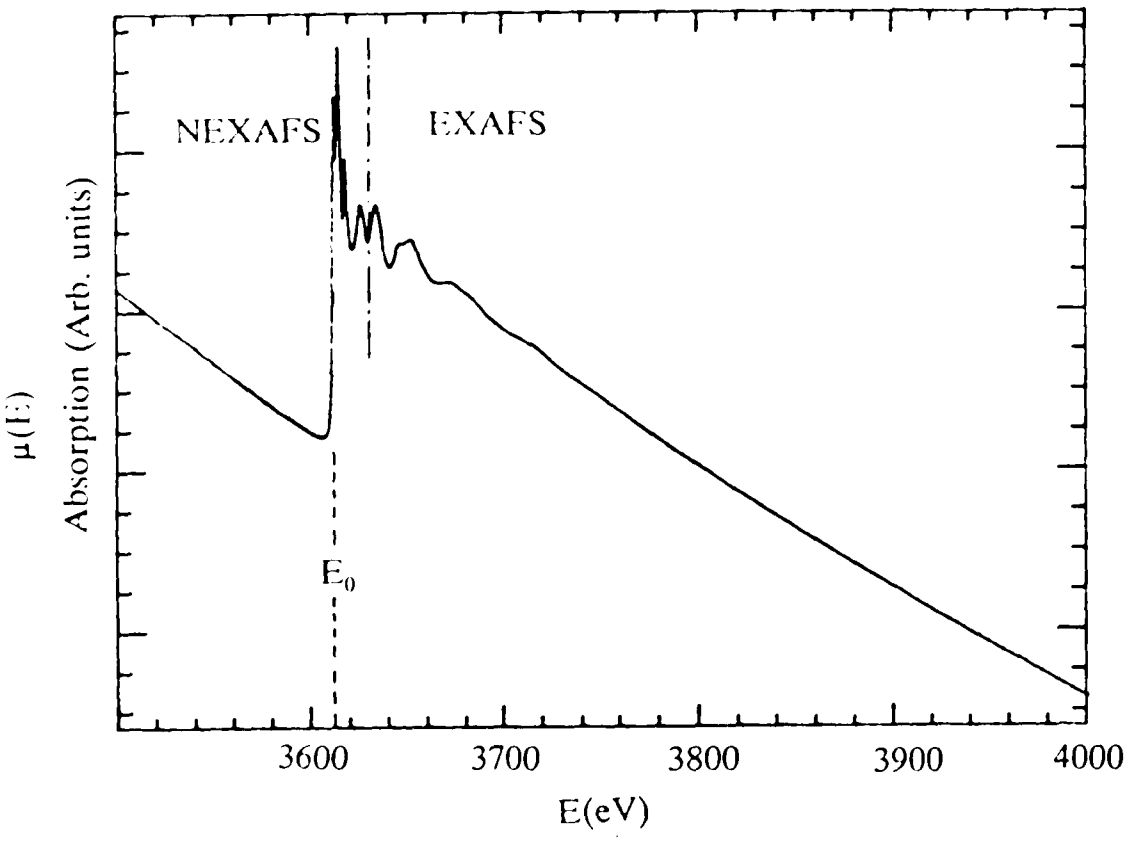


Figure 2. X-ray absorption spectrum of potassium iodide. $E_0$ is the energy threshold of the potassium *K*-edge. In the energy range $E - E_0 \leq 30 \sim 50$ eV, the spectrum is regarded as near-edge x-ray absorption fine structure (NEXAFS). In the range ~ 30 eV to 1000 eV above $E_0$, the spectrum is regarded as extended x-ray absorption fine structure (EXAFS).

processes at the central atom. It is clear that each EXAFS wave is determined by the backscattering amplitude, interatomic distances $r_j$, and the sinusoidal oscillation which is a function of interatomic distances $2kr_j$ and the phase shift $\phi_j(k)$. While the amplitude function $F_j(k)$ depends only on the type of backscattering atoms, the phase function contains contributions from both the absorbing atom and the backscattering atom.

$$\phi_{ij}^{l}(k) = \phi_{ij}^{l}(k) + \phi_j(k) - l\pi \tag{5}$$

where $l = 1$ for $K$ and $L_1$ edges. Here $\phi_i(k) = 2\delta_l'$ is the $l$ phase shift of the absorber and $\phi_j = \theta$ is the phase of the backscattering amplitude.

By comparing the EXAFS spectrum of an unknown compound to a model compound, one can determine the coordination number $N_j$ of the absorber, the bonding length $r_j$ between the absorber and its neighboring atoms, and the Debye-Waller factor $\sigma_j$ which counts for thermal vibrations and static disorder of the central atom. Unlike x-ray diffraction which probes long-range ordered structure, the EXAFS technique probes the local environment of the absorbing atom. Therefore, this technique can be applied to study the microscopic structure of disordered materials, such as many polymeric systems.

### 3.1.1 Amplitude Function and Phase Shifts in EXAFS

Equation 4 shows that each EXAFS wave contains two sets of highly correlated variables: { F(k), $\sigma$, $\lambda$, N } and { $\phi$(k), $E_0$, r }. Significant correlations can occur within and between these two sets of variables, as well as between different scattering terms. To determine the coordination number, N, and the Debye- Waller factor $\sigma$, the amplitude function F(k) must be known reasonably well. To determine the interatomic distance $r$, the phase shift function $\phi$(k) must be known accurately.

While both F(k) and $\phi$(k) can be determined empirically from model compounds,

they also can be calculated from first principles. Using an electron-atom scattering model,[67] these functions, which vary systematically with atomic number, have been calculated for most elements in the periodic table.[69] These theoretical functions and their parameterized versions[70,71] are widely used in EXAFS analysis, resulting in better than 0.5%, 10%, and 20% accuracy in r, $\sigma$, and N determinations, respectively.

It should be noted that the phase shifts are unique only if the energy thresholds, $E_0$, are specified. Changing $E_0$ by $\Delta E_0 = E'_0 - E_0$ will change the wavevector k to

$$\begin{aligned} k' &= [\, k^2 - ( \frac{2m}{\hbar^2} (E'_0 - E) ) \,]^{1/2} \\ &= [\, k^2 - 0.262\ (\Delta E_0) \,]^{1/2} \end{aligned} \tag{6}$$

where k is in $\text{Å}^{-1}$ and $\Delta E_0$ in eV. The corresponding modification of the phase shift function will be

$$\begin{aligned} \phi'(k') &= \phi(k) - 2(k' - k)r \\ &= \phi(k) + 0.262\ r(\Delta E_0)/k \end{aligned} \tag{7}$$

for $0.262(\Delta E_0) \ll k^2$. Thus, the difference $\Delta\phi(k) = \phi'(k') - \phi(k)$ decreases with increasing k, indicating that phase shifts are more sensitive to a change in $E_0$ at small k than at large k.

### 3.1.2 Static Disorder and Thermal Vibrations

The Debye-Waller factor $\sigma$ plays an important role in EXAFS spectroscopy. It contains structural and chemical information which is otherwise difficult to obtain, yet it comes as a bonus in the EXAFS determination of interatomic distances. In general, the Debye-Waller factor $\sigma$ includes both static disorder $\sigma_{stat}$ and thermal vibrations $\sigma_{vib}$. They are uncorrelated and both can be derived from the pair distribution function g(r) through the following equation

$$\chi(k) = \frac{F(k)}{k} \int_0^\infty g(r) e^{-2r/\lambda(k)} \frac{\sin(2kr + \phi(k))}{r^2} dr \qquad (8)$$

In general, g(r) depends on the interatomic potential. For $\sigma_{vib}$ in particular, g(r) depends on the vibrational frequency and the absolute temperature.

Assuming that the static disorder is small with a symmetric pair distribution function and that thermal disorder is due to harmonic vibrations, we may write

$$\sigma^2 = \sigma_{stat}^2 + \sigma_{vib}^2 \qquad (9)$$

The term $\sigma_{stat}$ is related to the symmetric Gaussian pair distribution function

$$g(r) = \frac{1}{\sqrt{2\pi}\,\sigma_{stat}} e^{-(r - r_0)^2 / 2\sigma_{stat}^2} \qquad (10)$$

where $r-r_0$ is the deviation from the mean distance $r_0$.

Assuming a harmonic motion for a diatomic system, the vibrational contribution to the Debye-Waller factor in the Debye approximation is given by[72,73]

$$\sigma_{vib}^2 = \frac{\hbar}{2M_r} \int \rho_j(\omega) \coth\left(\frac{\hbar\omega}{2k_B T}\right) \frac{d\omega}{\omega}; \qquad M_r = \frac{M_i M_j}{M_i + M_j}$$

$$\textit{where} \qquad (11)$$

$$\rho_j(\omega) = \frac{3\omega^2}{\omega_D^2}\left(1 - \frac{\sin(\omega R_j/v)}{\omega R_j/v}\right); \qquad \omega_D = \frac{k_B \Theta_D}{\hbar}$$

and is derived from the Debye temperature $\Theta_D$, $v = \omega_D/k_D$, where $k_D = (6\pi^2 N/V)^{1/3}$ and V is the crystal volume.

In principle, these two components ($\sigma_{stat}$ , $\sigma_{vib}$) of the Debye-Waller factor can only be separated by a temperature-dependent study of $\sigma(T)$. However, if $\sigma_{vib}$ can be estimated from vibrational spectroscopies or if $\sigma_{stat}$ is known from other studies, the other term can be calculated from the experimentally determined $\sigma$.

3.1.3 Data Analysis

To obtain accurate structural information with EXAFS, three assumptions must be made: (1) EXAFS is a simple sum of waves due to various types of neighboring atoms (this assumption implies that multiple scattering is relatively unimportant); (2) the amplitude function is transferable for each type of backscatterer B; and (3) the phase function is transferable for each pair of atoms A - B (where A is the absorber and B is the backscatterer). Transferability[74] implies that these functions are relatively insensitive to chemical bonding for energies 60 - 1000 eV above the absorption edge, such that once determined for a known systems, these functions can be applied to unknown systems which contain the corresponding elements.

Data analysis in EXAFS is a relatively complex. The EXAFS data is converted into $\chi(k)$ versus k, where $k=[(2m/\hbar^2)(E-E_0)]^{1/2}$ is the wavevector of the outgoing electron, by normalizing the pre-edge background using the expression $\chi(E) = [\mu(E)-\mu_0(E)]/\mu_0(E)$. Then $\chi(k)$ is multiplied by some power of k, (commonly $n=3$) to compensate for the diminishing amplitudes at high k values, to give $k^n\chi(k)$. The data is truncated at low and high k before Fourier transformation, to avoid edge effects and poor signal-to-noise at high energies.

The Fourier transform technique is used to convert the fine structure oscillation spectrum $k^n\chi(k)$ in momentum (k) space over the finite k range $k_{min}$ to $k_{max}$ into the radial distribution function $\rho_n(r')$ versus r' in distance space. The variable r' is related to the true interatomic distance r by a "phase shift" $\alpha = r-r'$. The phase shift $\alpha$ can be obtained from model compounds and transferred to the unknown systems to predict distances. Fourier filtering then is used to select the distance range of interest with some smooth window function, and the $k^n\chi(k)$ data is backtransformed into k space. The filtered EXAFS

spectrum can then be fitted with model compounds using conventional curve fitting techniques.

The curve-fitting technique is to best fit the EXAFS spectra in k space with some phenomenological models. There are several ways of dealing with data fitting. The refinement procedure can be based on commonly used least-squares or absolute-difference minimization. One could fit the entire EXAFS spectrum directly, or fit the experimental amplitude and phase function separately in cases where strong correlation exists between the amplitude and the phase. Finally, although the amplitude and the phase shifts can be dealt with numerically, it may be convenient to parameterize these functions with simple analytical forms.

This latter approach has the advantage of reducing these functions to a few parameters. These parameters can be obtained either by fitting the experimental EXAFS of structurally known model compounds or from the theoretical calculations, and then transferring them to the unknown system for structural determination.

## 3.2 Theoretical Background of NEXAFS.

The range from 0 to roughly 50 eV above the absorption edge is designated as Near-edge x-ray absorption fine structure (NEXAFS)(Figure 2). It is distinguished from the higher energy EXAFS regime by stronger scattering of the excited electron by the surrounding atoms. In general, the standard single-scattering EXAFS analysis is not valid, and multiple scattering must be treated accurately. This means, on the one hand, that the near-edge structure is more difficult to interpret than EXAFS, but, on the other hand, that it contains extra information. From a structural point of view, NEXAFS is usually

interpreted in terms of the appropriate component of the local density of states. NEXAFS is sensitive to multi-atom positional correlations, and, in principle, can be used to determine such quantities as bond angles, and site symmetries, which are unobtainable from EXAFS.

In the low energy NEXAFS range, the effects of multiple scattering become important due to much stronger electron-electron scattering, large modulation of the absorption cross-section, and strong interaction of the electron with the solid. Therefore, in this energy range, it is more appropriate to regard the electron as being excited into a localized antibonding state of the system (Figure 3) rather than to describe it as an outgoing plane wave as in EXAFS.

### 3.2.1. Polarization Dependence of the Near-edge Spectrum

Although multiple scattering is the main cause of the difficulties in establishing a clear theoretical model of NEXAFS, the probability of photo-excited transitions from an initial state to unoccupied molecular states is, nevertheless, governed by dipole selection rules

$$P \propto |\langle \psi_f | E \cdot p | \psi_i \rangle|^2 \qquad (12)$$

For a $\sigma$ or $\pi$ symmetry of the final state, the transition probability depends on the orientation of the electric field **E** of the photon with respect to the molecular axis,[75,76] It has been calculated that the transition probability from the initial state to a final state of $\sigma$ symmetry is proportional to $\cos^2\delta$, where $\delta$ is the angle between the polarized **E** vector and the molecular axis(figure 4), and to a final state of $\pi$ symmetry is proportional to $\sin^2\delta$ as:

$$N_\sigma = \left(\frac{3N_0}{4\pi}\right) \cos^2\delta \qquad (13)$$

$$N_\pi = \left(\frac{3N_0}{8\pi}\right) \sin^2\delta \qquad (14)$$

By taking advantage of the horizontal polarization of synchrotron radiation, the near-edge spectrum can be used to probe the orientation of the molecule relative to the surface by varying the angle between the E vector and the molecular axis.

3.2.2. Data Fitting

Theoretical calculations of NEXAFS spectrum close to threshold (within approximately 50 eV) were carried out by P. J. Durham, J. B. Pendry, and C. H. Hodges[77,78,79] using multiple scattering theory. The multiple scattering is calculated by a real-space cluster approach, which is considerably more flexible than band structure methods. However, in our experiments to determine the orientation of molecular bonding by comparing spectra taken at different angles of incidence of a highly polarized x-ray beam, an accurate theoretical calculation may not be needed. Instead, the spectra are often analyzed by a data-fitting procedure with a least-squares analysis of peak profile widths and positions. The data-fitting procedure we used to analyze our NEXAFS spectra is described below.

Background Removal

The spectrum is normalized to the 'background' absorption ($\mu_0$), as done in EXAFS, by applying the formula $\chi(E)=[\mu(E)-\mu 0(E)]/\mu_0(E)$, where $\mu$ and $\mu_0$ are the observed and

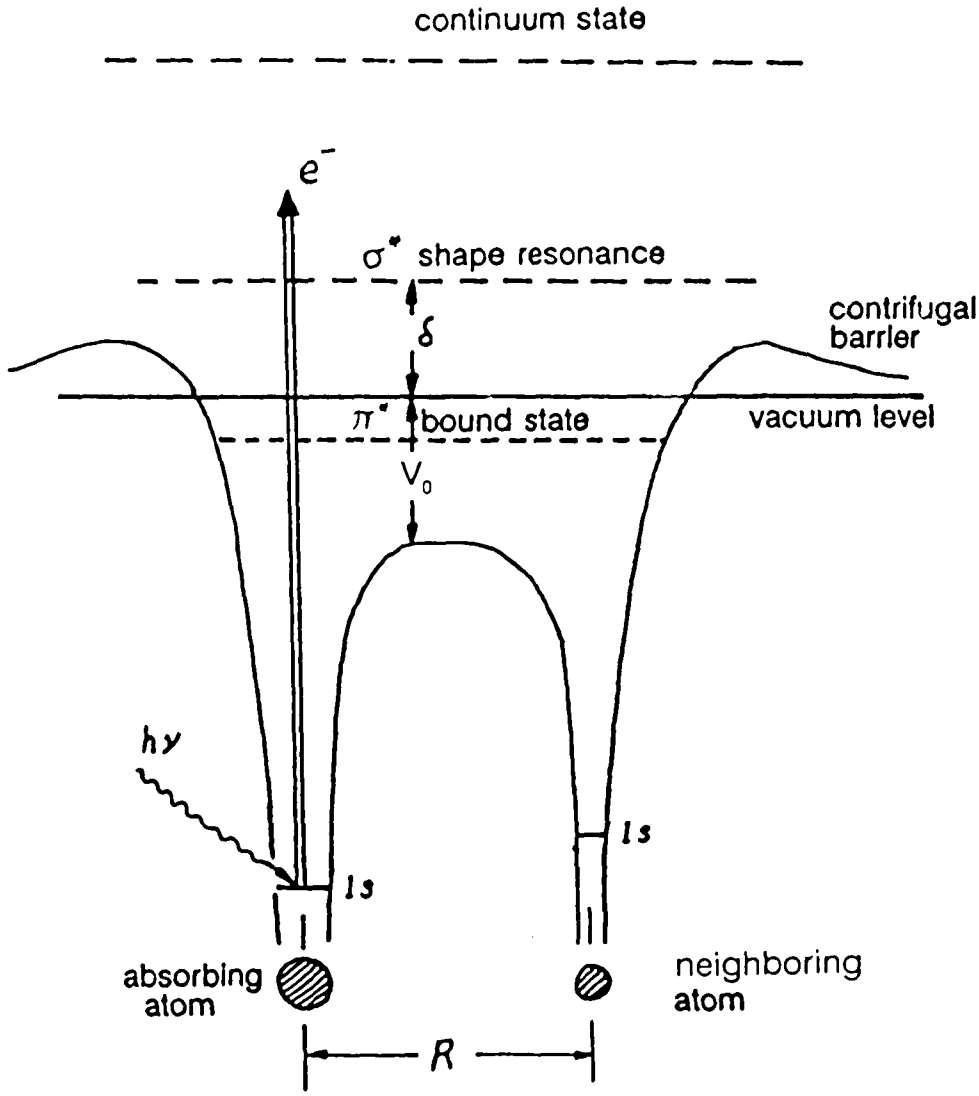


Figure 3. Schematical diagram of $\pi^*$ and $\sigma^*$ resonances in a diatomic molecule with an intramolecular bond length R. The $\pi^*$ resonance corresponds to a transition of a core electron to an empty or partially filled molecular orbital (bound state). The $\sigma^*$ shape resonance involves a quasi-bound state in the continuum.

'free atom' absorption coefficients, respectively. The determination of $\chi$ is by no means straightforward since $\mu_0$ is generally not known. A commonly used procedure is to approximate $\mu_0$ by a smooth curve (typically a polynomial or cubic spline) fitted to $\mu$. In transmission experiments, $\mu$ generally drops off monotonically, due primarily to the energy dependence of the ionization chamber efficiency and absorption due to other atoms. On the other hand, in fluorescence experiments the baseline rises as a function of energy due to increasing sample penetration, increased Compton scattering, reduced absorption of the scattering, and other effects.

Peak Fitting and Step Function

The NEXAFS spectrum has two groups of features, one group representing transitions to the continuum states, and the other representing transition to discrete states. Apparently, some angle-dependent peaks are symmetric, such as $\pi^*$ transition peaks, and some asymmetric, such as $\sigma^*$ shape resonances. In general, the resonances below or near the ionization limit are well described by a Lorentzian distribution if the resolution of the peaks is limited by its life-time. The resonances are described by a Gaussian line shape, while the FWHM (full-width at half-maximum) of the Gaussian distribution is slightly larger than the resolution of the monochromator (approximately 1.2 eV). The asymmetric resonant peak can be described by an asymmetric function.[29] For our experiments, we selected a Lorentzian distribution because of the fitting program, to fit the angular dependent peaks.

The spectral feature which represents transitions to the continuum states is essentially step-like. In the study of the C 1s edge of diamond by Morar *et al.*[80] and in the study of the $L_{2,3}$ near-edge region of Pt and Ir compounds by Horsley,[81] the step was

modelled by an arctan function which is the integral of a Lorentzian function. In a study of the C *K*-edge of LB films by D. A. Outka *et al.*[29] the error function was chosen to represent the transitions to the continuum because this function is the result of a convolution of a vertical step with the Gaussian output of the monochromator. Figure 4 shows an example of our data fitting. Five Lorentzian distributions are used to fit the angular dependent peaks, which represent the transitions to discrete states, and an arctan function is used as a step function to fit the feature that represents the transitions to the continuum states.

Although the positions and widths of angle-dependent NEXAFS peaks can be obtained from the different spectra, their intensities cannot be so easily derived; indeed, obtaining the intensities is the principal difficulty in analyzing the original spectra. The reason for this is that the exact shape of the background is unknown. Therefore, the information we can reliably obtain from data fitting is the relative area of the peaks, which can be used to determine the bonding angle by comparing spectra at different angle of incidence,[79,82] or to study the micro-structure of polymeric materials by comparing the spectrum of the sample to the spectrum of model compounds.[11]

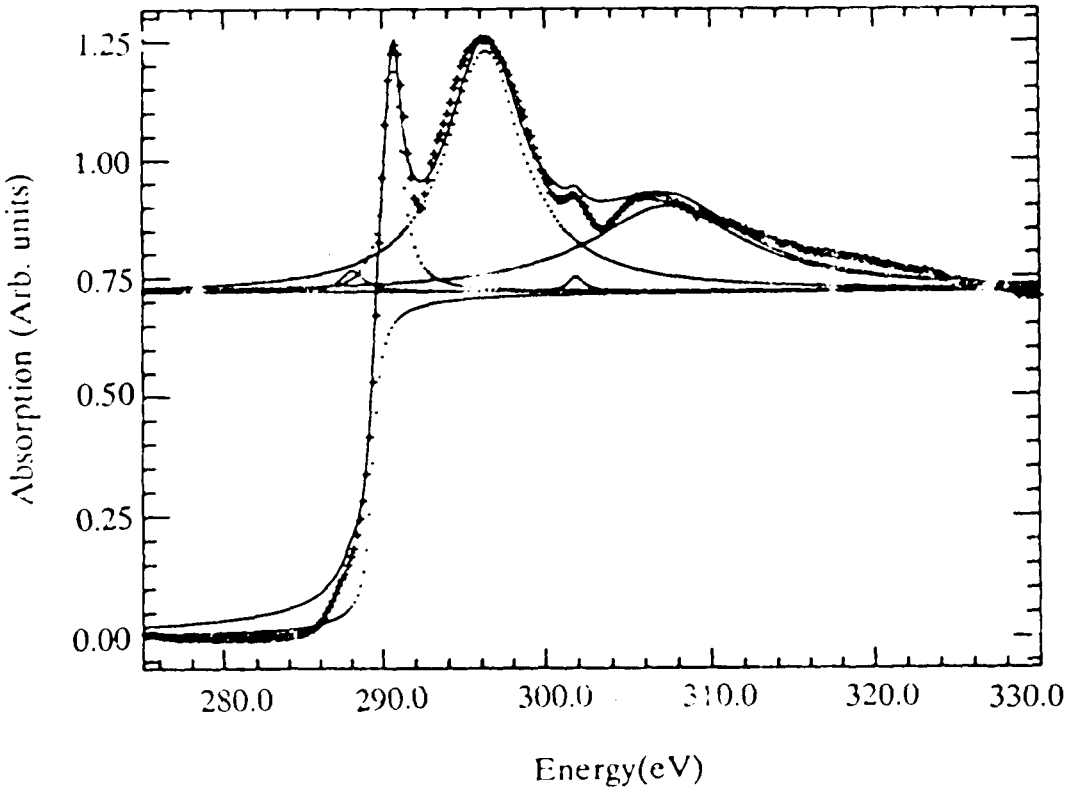


Figure 4. Carbon *K*-edge NEXAFS spectra of a 3-layer LB film of a mixture of ferrocene-derivatized alkylpyrroie and 3-hexadecylpyrrole (HDP) in 1:5 ratio on Pt substrate. The experimental data (+ + +) is fitted with a solid curve (—) which consists of five Lorentzian distributions and an arctan function (···).

3.3 Theory of Fourier-transform Infra-red Spectroscopy (FTIR)

By convention, the infrared region is split up into three parts: the near infrared (wavelength $\lambda$ = 0.78 - 3.0 $\mu$; wave number $\nu$ = 12,820 - 3333 $cm^{-1}$; photon energy E = 1.58 - 0.41 eV), the middle infrared ($\lambda$ = 3-30 $\mu$; $\nu$ = 3333 - 333 $cm^{-1}$; E = 0.41 - 0.041 eV), and the far infrared ($\lambda$ = 30 - 300 $\mu$; $\nu$ = 333 - 33 $cm^{-1}$; E = 41 - 4.1 meV). The energy of most molecular vibrations corresponds to that of the infrared region of the electromagnetic spectrum in the frequency range 400 $cm^{-1}$ to 4000 $cm^{-1}$. Spectroscopy in this region has been useful in identifing polymeric materials for both qualitative and quantitative determination of the chemical polymer and groups, chain branching, configuration and conformation, as well as steric and geometric isomerism.

In general, the absorption of infrared light can occur only if the dipole moment of the molecule in its initial state is different from that in the final state to which it is excited by the absorption of the infrared light. Such a transition is said to be infrared active. The variation of the dipole moment with the change in interatomic distance during the vibration corresponds to an oscillating electric field that can interact with the oscillating electric field associated with electromagnetic radiation. The requirement that absorption of a vibrational quantum is accompanied by a change in dipole moment is known as a selection rule. Vibrational transitions that do not result in a change of dipole moment of the molecule are not observed directly and are referred to as infrared inactive transitions. Therefore, molecules such as $H_2$, $O_2$, $Cl_2$, and $N_2$, will not yield any useful infrared absorption spectra because no change in dipole moment occurs during their vibrations, which are electrically symmetrical.

A complex molecule has many vibrational modes, which can be divided into two

separate categories: stretching modes including symmetric and asymmetric modes, and bending modes including scissoring, rocking, twisting and wagging modes. The molecular vibrations are complex and any specific mode is influenced by all the atoms in the molecule. However, the harmonic oscillator approximation can help us to identify the general frequency range of these modes. By considering the motion of a few atoms relative to one another and ignoring the rest of the atoms in the molecule, the vibration frequency $\nu$ ($cm^{-1}$) of a bond may be related to the masses of the vibrating atoms and the force constant f (dyne/cm) as

$$\nu = \frac{1}{2\pi c}\left(\frac{f\cdot(m_1 + m_2)}{m_1 m_2}\right)^{1/2} \qquad (15)$$

where c is the speed of light, and $m_1$ and $m_2$ (g) are the masses of two atoms. Thus, for example, the force constant for a carbon related single bond, double bond, and triple bond are approximately $5\times10^5$, $10\times10^5$, and $15\times10^5$ (dyne/cm), respectively.

Vibrational spectroscopy of surface species can provide direct information about structure and bonding. An advantage of this technique is that infra-red photons are not limited to vacuum. Therefore, it is possible to study surface and interfacial systems that are inaccessible to electron spectroscopies.

### 3.3.1. Polarization

Infra-red light is absorbed when the dipole moment due to a molecular vibrational mode interacts with the electric vector of the infra-red beam. If a polarized infra-red beam is applied at a certain incident angle, only those vibrational modes with a compound along the electric field will be detected. For example, if a beam is applied at a normal (grazing) incident angle, only those vibrational modes parallel (normal) to the sample surface will be

detected. Thus, one can determine the orientation of a particular functional group with respect to the surface normal.

Electrochemically polymerized poly(3-methylthiophene) (P3MeT) thin films on Pt substrates were studied by infrared reflection absorption spectroscopy (IRRAS). A detailed description of the IRRAS technique can be found elsewhere.[83,84,85] When light is reflected from a flat metal surface, the component polarized perpendicular (s wave) to the plane of reflection (the plane which contains both the incident and the reflected beams and is perpendicular to the metal surface) undergoes a phase shift of about 180 degrees at virtually all angles of incidence(Figure 5). Hence, the reflected beam will destructively interfere with the incident beam, producing a node at the reflective surface. The component polarized parallel to the plane of reflection (p wave) experiences a phase shift on reflection which varies from zero degrees at small incident angles to about 180 degrees at large angles. For grazing incident angles, the net result is an electric field vector polarized normal to the reflecting surface. At a grazing incident angle, only the vibrational modes with a component of the dipole transition moment oriented along the surface normal will be excited. This surface selection rule and its sensitivity can be used to study the orientation of thin films on metal substrates.

### 3.3.2. Polymer Studies

In general, for polymer molecules with large, complex, repeat units such as cellulose and polyethylene terephthalate, the differences between the spectra of the monomer and the polymer are quite small. Hence, vast collections of infrared spectra of organic molecules are used to interpret the spectrum of a polymer in terms of its organic functional components. On the other hand, for simple polymer molecules such as polyethylene and

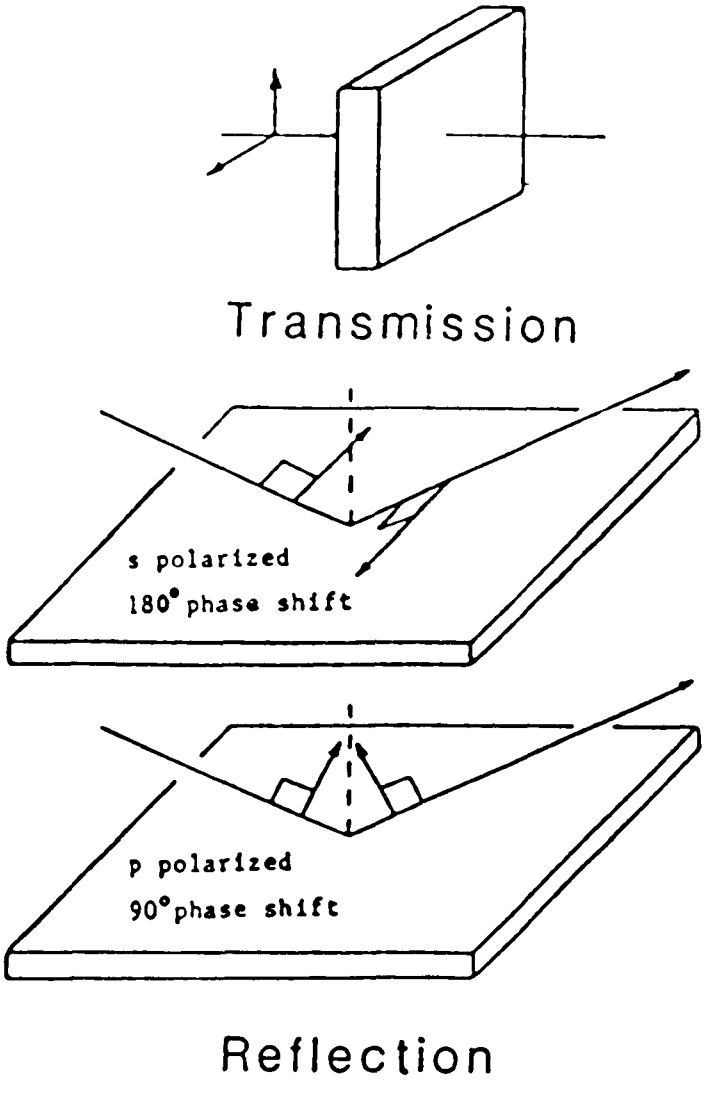


Figure 5. Electric field vector geometries for transmission and reflection at grazing incident at a metal surface.

polyoxymethylene, the spectra of the monomer and the polymer are very different from each other.

The interpretation of the vibrational spectrum of an isolated repeat unit or monomer usually has been approached in two ways. First, by performing a normal coordinate analysis,[86] the energies of the vibrational normal modes of simple molecules are calculated. If the appropriate structural model and parameters are used, the frequencies calculated will agree with the experimentally observed frequencies and constitute evidence in support of the structure.

The second and most common method of interpreting the spectrum of a molecule is to use structure-frequency correlations,[87] which are possible because the vibrational modes of a complex molecule fall into two classes, "intragroup" modes, and "skeletal" modes. There is a wealth of spectroscopic evidence to support the assumption that these two classes are distinct. The interactions of the "intragroup" modes with neighboring groups are generally small. These "internal" modes generally have a characteristic frequency range irrespective of the molecular framework to which the group is attached. Empirical studies of these group frequency variations in a series of molecules have led to useful structure-frequency correlations that are useful in the interpretation of the spectra of a new molecule. The "skeletal" modes generally result from extensive interaction of the modes with the molecular framework, and are characteristic of the particular molecule. Hence, these "external" modes are not useful for correlations, but do "fingerprint" the spectrum of the particular molecule, making it possible to identify almost any molecule. Extensive collections of spectra are used to identify an unknown sample.

Similar considerations of "internal" and "external" modes apply to the study of the spectrum of macromolecular repeat units. The lattice couples the chemical repeat units so

they behave as coupled harmonic oscillators. The vibrational pattern depends on the number of coupled oscillators or cells, the normal modes of an isolated repeat unit, and the extent of coupling of the vibrational modes with other repeat units. For N coupled cells containing M atoms, there are 3NM degrees of freedom. The three translational degrees of freedom give null vibrations and the rotation of the polymer molecule about its own axis can be ignored, so 3NM - 4 normal modes are important.

The salient features of the polymer spectrum may be demonstrated by analyzing a uniform one-dimensional lattice of point masses elastically bound to each other. The N-frequencies for a linear chain of N atoms acting as parallel dipoles with fixed ends (including only nearest neighbor interactions) are given by the following equation:

$$W_K^2 = W_0^2 + W_1^2 (1 + \cos\theta), \qquad \theta = k\pi/(N + 1), \quad k = 1, 2, 3... \qquad (16)$$

where $W_0$ = frequency of the uncoupled mode, and $W_1$ = interaction parameter. Thus, for this model $W_K$ is a function of the phase ($\theta$) only. Each of the modes for an isolated monomer generates N bands in the chain of N units. If the interaction parameter $W_1$ for the mode is small, all of the normal vibrations fall in the neighborhood of $W_0$ and a "characteristic" polymer group frequency is observed. This is the case, for example, with the carbohydrogen stretching modes which occur at the same frequencies irrespective of the polymer. For a large $W_1$, a wide range of frequencies can occur and a "skeletal" frequency is observed.

## 3.4. Theory of X-ray Diffraction

The characteristic of a LB film is its oriented and well-defined layers. However, once a LB film is deposited on a solid substrate, the high degree of ordering in the direction

normal to the substrate is not inevitable, and must be confirmed by x-ray diffraction, which is a powerful technique to study the material with a long-range ordered structure.

Studies of layer structure require the energy of an x-ray photon in the 10 to 50 keV [0.28-1.24 Å] range. Its energy can be related to its wavelength $\lambda$ by $\epsilon = hc/\lambda$, or $\lambda(\text{Å}) = 12.4/\epsilon(\text{keV})$. X-rays are generated both by the deceleration of electrons in metal targets and by the excitation of the core electrons in the atoms of the target. For a conventional laboratory x-ray diffraction experiment, a bombarded copper target generates a CuK$\alpha$ x-ray beam at 1.5418 Å [8.3 keV], which is in the middle of the relevant range. Most of our experiments were carried out using the synchrotron radiation source, which is generated by the acceleration of relativistic electrons, at the National Synchrotron Light Source (NSLS) at Brookhaven National Laboratory. The x-ray photon wavelength selected was $\lambda$ = 0.9 Å.

### 3.4.1. Crystal

Considering that the incident waves of x-ray are reflected specularly from parallel planes of atoms in the crystal, the beams are diffracted when the reflections from parallel planes of atoms interfere constructively. If parallel lattice planes are spaced a distance (d) apart, the path difference for rays reflected from adjacent planes is $2d\sin\theta$, where $\theta$ is the angle of incidence measured from the plane. Constructive interference of the radiation from successive planes occurs when the path difference is an integral number n of wavelengths $\lambda$, so that $2d\sin\theta = n\lambda$, which is the Bragg law. (Bragg reflection can occur only for wavelength $\lambda \leq 2d$.) The integer n is known as the order of the corresponding reflection.

If the Bragg peak is associated with a change in wave vector which equals reciprocal

lattice vector $\mathbf{k}' - \mathbf{k} = \mathbf{K}$, then the path difference between the rays scattered at $\mathbf{d}_i$ and $\mathbf{d}_j$ will be $\mathbf{K}\cdot(\mathbf{d}_i - \mathbf{d}_j)$ and the phases of the two rays will differ by a factor $\exp(i\mathbf{K}\cdot(\mathbf{d}_i - \mathbf{d}_j))$. Thus, the phases of the rays scattered at $\mathbf{d}_1$, ..., $\mathbf{d}_n$ are in the ratios $\exp(i\mathbf{K}\cdot\mathbf{d}_1)$, ..., $\exp(i\mathbf{K}\cdot\mathbf{d}_n)$. The net ray scattered by the entire primitive cell is the sum of the individual rays, and will, therefore, have an amplitude containing the factor

$$S_k = \sum_{j=1}^{n} \exp(i\mathbf{K}\cdot\mathbf{d}_j). \tag{17}$$

The quantity $S_k$ is known as the geometrical structure factor[88] and is defined as a summation over a single cell. The amplitude of the wave scattered from a volume element is proportional to the local electron concentration $n(\mathbf{r})$. The total amplitude of the scattered wave in the direction of $\mathbf{k}'$ is proportional to the integral over the crystal of $n(\mathbf{r})dV$ times the phase factor $\exp(i\mathbf{K}\cdot\mathbf{d})$. Therefore, the scattering amplitude is defined by the quantity:

$$A = \int dV\, n(\mathbf{r}) \exp(i\mathbf{K}\cdot\mathbf{r}),$$

where $\mathbf{K} = \mathbf{k}' - \mathbf{k}$.

### 3.4.2. Superlattice Structure

A superlattice structure is defined as a multilayer structure formed by different materials in a high degree of one-dimensional structure order, in which the average composition of each layer along the growth direction is defined by a translation vector and a modulation wavelength. Within a given plane there can be long-range order. The resulting multilayer film has a high degree of chemical order and one-dimensional structural order.[89,90] The films generally have good coherence along the growth direction but poor lateral coherence between different regions. In the middle of a layer, the structure and lattice parameters correspond to those of the pure bulk materials.[91]

X-ray diffraction provides the most easily interpreted structural data characterizing a broad range of existing multilayers. This technique is nondestructive, and most of the measurements can be done in a reflection geometry leaving the sample on the substrate. The evolution of one-dimensional order along the growth direction can be studied on a standard diffractometer, but the detailed evolution of three-dimensional order necessitates scans in general directions in reciprocal space. The positions and line shapes of the Bragg reflections of the average lattice and of the surrounding satellite reflections are used to calculate the average lattice constants and the average modulation wavelength, and to obtain a measure of fluctuations in both quantities that may be caused by composition gradients and by loss of coherence. The intensities of the reflections are used to obtain the composition and the strain wave profiles.

In our experiments, Y-type Langmuir-Blodgett films (Figure 7c) proved to be ideal multilayer films with sharp interfaces and an integral number of layers. The diffraction from this structure can be calculated for an idealized model. Suppose that a and b are the thicknesses of two adjacent layers formed with different textures, respectively. The intensity of N alternating layers with height d = a + b can be approximated by regions of constant scattering power $g_a$ and $g_b$. If a = b, then the intensity as a function of the scattering vector along the modulation direction q is given by[91,92]

$$I(q) \propto \frac{4}{q^2}\sin^2\left(\frac{qd}{4}\right)\left[\frac{\sin^2(Nqd/2)}{\sin^2(qd/2)}\right]\left[g_a^2 + g_b^2 + 2g_a g_b \cos\left(\frac{qd}{2}\right)\right]. \qquad (18)$$

Reflections occur at values of $q = 2\pi l/d$ for odd integer values of $l$ with an intensity of $I(l) = (Nd/\pi l)^2(g_a - g_b)^2$, and for even integer values of $l$ with an intensity of $I(l) = (Nd/\pi l)^2(g_a + g_b)^2$. We observed this periodic variation of the intensity of the x-ray diffraction pattern in our experiments (discussed in chapter 5.2.3).

3.4.3. In-plane Structure

The three-dimensional structure of a multilayer film can be considered as a combination of the structure along the growth direction, called the z-direction structure, and the structure within the layers, called the in-plane structure. The in-plane x-ray diffraction pattern is probing the order of interfaces between layers. If the difference between the lattice parameters of the two materials is sufficiently small, then the layers can be constrained to match perfectly by introducing a coherency strain into each layer. The strain energy is balanced by the energy needed to introduce a misfit dislocation that would relieve part of the coherency strain.[93]

There is a phase transition when dislocations develop and their number increases continuously until all the coherency strain is relieved and the interfaces are incoherent. This is called a commensurate-incommensurate (CI) transition.[91] In the case of multilayers, the transition occurs because the balance between coherency strain energy and dislocation energy changes with the modulation wavelength. The coherency strain energy per unit volume is constant, whereas the dislocation energy varies as the number of interfaces per unit volume. Since the dislocation energy decreases with increasing wavelength, a CI transition occurs in all multilayer systems, but the critical wavelength $\lambda_c$ will depend on the mismatch between the two components and on their elastic properties. If the symmetry of the layers on each side of the interface is different, then the CI transition is anisotropic.

When the mismatch across the interface is small (below some critical modulation wavelength), the interfaces are coherent; i.e., there is a single lattice parameter that describes the interplanar spacings perpendicular to the direction of growth. This results in a coherency strain as the material with the larger lattice parameter is compressed and vice versa for material with the smaller parameter. The presence of coherency strains can be

observed directly by measuring the d spacings of planes perpendicular to the film.[94]

### 3.4.4. Temperature Dependence of X-ray Diffraction

Most crystals maintain their basic structures at elevated temperatures up to the limit of a phase transition. However, this is not generally true for polymeric materials, which comprise mixed crystalline and amorphous phases. This structural change of the material in a crystalline or an amorphous phase at elevated temperature can be probed with x-ray diffraction by observing amplitude changes, peak position shifts, or the appearance of new peaks. Amplitude changes are caused mainly by thermal oscillations; peak shifts indicate a change in d spacing; and the appearance of new peaks indicates that there is a phase transition or phase separation in the sample.

To consider the temperature dependence of the amplitude of the x-ray diffraction, we let the position of the atom nominally at $\mathbf{r}_j$ include a term $\mathbf{u}(t)$ fluctuating in time: $\mathbf{r}(t) = \mathbf{r}_j + \mathbf{u}(t)$. We suppose that each atom fluctuates independently about its own equilibrium position. Then the scattered intensity can be shown to be[95]

$$I = I_0 \exp(-\frac{1}{3}\langle u^2 \rangle K^2), \tag{19}$$

where $I_0$ is the scattered intensity from the rigid lattice. The exponential factor is the Debye-Waller factor, and $\langle u^2 \rangle$ is the mean square displacement of an atom. The thermal average potential energy $\langle U \rangle$ of a classical harmonic oscillator in three dimensions is 3/2 $k_B T$, whence

$$\langle U \rangle = \frac{1}{2} M \omega^2 \langle u^2 \rangle = \frac{3}{2} k_B T, \tag{20}$$

where M is the mass of an atom, and $\omega$ is the frequency of the oscillator. Thus the

scattered intensity of a peak at *hkl* as a function of temperature is

$$I(hkl) = I_0 \exp\left(-\frac{k_B T K^2}{M\omega^2}\right), \tag{21}$$

where *hkl* are the indices of the reciprocal lattice vector **K**.

Based on Bragg's diffraction law, $2d\sin\Theta = n\lambda$, it is clear that peak shifts in the diffraction pattern indicate a change in d spacing in the lattice spacing. This change d-spacing is more due to the thermal expansion or contraction than due to thermal vibration. Thermal vibrations already have been counted into the temperature dependence of the amplitude. The d-spacing change due to thermal expansion or contraction shifts towards smaller or larger diffraction angles, respectively, which indicates a lattice constant change at different temperatures.

There are cases that in which a peak splits into two peaks or a new peak appears in x-ray diffraction pattern at different temperatures. The appearance or disappearance of a new peak in the diffraction pattern indicates a phase transition, such as a phase transition structural reordering or a CI transition as discussed in section 3.4.3.

# Chapter 4. Sample Preparation

Several techniques for sample preparation have been used, depending on the nature of the material. Each technique has advantages and disadvantages, so the type of information desired often dictates the method of preparation. Identification of a polymer sample requires a high quality spectrum, free from extraneous bands in infrared spectroscopy. Quantitative structural studies require a sample of adequate thickness to yield strong bands in the region of interest: this may demand an extremely thin or thick sample.

For our work, samples were prepared in the form of thin films in four different ways, depending on the nature of the polymer: solution casting, spin-coating, electrochemical polymerization on metal substrates, and Langmuir-Blodgett films.

## 4.1. Solution Casting and Spin-coating

In the solution casting and spin-coating methods, a solution of the desired polymer or polymer-salt complex is used to cast or spin-coat a thin film on a substrate, which is normally cleaned with ethanol and dried with $N_2$ gas. Spin-coating is used for thinner films. Polyimide tape is often used to prepare samples for x-ray transmission experiments because it is transparent to x-rays. After a small amount of solution is cast or spin-coated on a substrate, samples are normally kept in a vacuum oven for about 2 hours, then moved to a dry box to prevent contamination from moisture.

### Poly(ethylene oxide)/Potassium iodide (PEO/KI)

Poly(ethylene oxide) (PEO) with an average molecular weight of 600,000 and of

99.5% purity was obtained commercially (Aldrich Chemical). Reference compounds, including potassium iodide(KI), potassium tert-butoxide[$(CH_3)_3COK$], potassium acetate($C_2H_3O_2K$), and dibenzo-18-crown-6 ($C_{12}H_{24}O_6$, 18-crown-6) of similar purity were obtained from the same source. Complexes of PEO/KI and 18-crown-6/KI were formed in acetonitrile solution, and then cast as a film of about 100 μm thick on Kapton tape. The other reference compounds $(CH_3)_3COK$, $C_2H_3O_2K$, and KI, in the form of fine powders, were brushed on Scotch tape.

## 4.2. Electrochemical Polymerization

A working electrode, a reference electrode, and a counter electrode were enclosed in a sealed cell containing a solution of the desired monomers and the salt tetraethyl-ammonium tetrafluoroborate $(TEA)^+(BF_4)^-$ (Figure 6). The cell was kept under an $N_2$ atmosphere to prevent any undesirable chemical reaction due to $O_2$. If a positive potential is applied to the working electrode with respect to the reference electrode, which is a saturated calomel electrode (SCE) in our experiment, the anions $(BF_4)^-$ will move to the working electrode, and cations $(TEA)^+$ to the counter electrode. If the working electrode and the counter electrode are made of stable metals so that the electrode is not oxidized, a monomer, such as 3-methylthiophene, will be oxidized at a sufficiently positive potential, and a conducting polymer film will grow on the working electrode. In our preparations, the working and counter electrodes are both made of platinum-coated glass. The solvent most often used is acetonitrile and the monomers are pyrrole or thiophene. The anodic potential applied on the working electrode is 1.2 V/SCE for pyrrole, and 1.4 or 1.8 V/SCE for thiophene. The thickness of the sample can be estimated by calculating the product of the current monitored on the counter electrode, the oxidization time, and the area of the coated

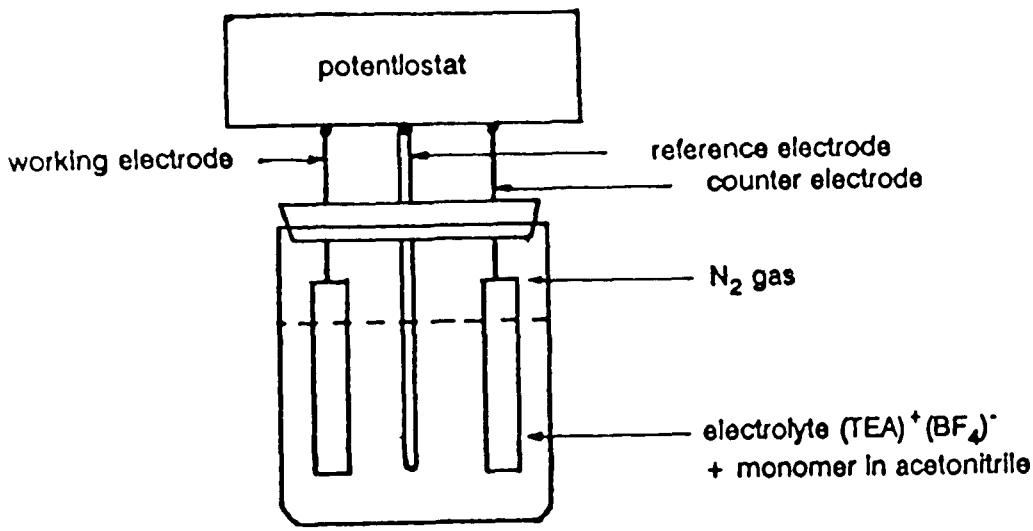


Figure 6. Experimental setup of electrochemical polymerization cell. The cell consists of a working electrode, a counter electrode, and a reference electrode. During oxidation, a positive potential is applied on the working electrode with respect to the reference electrode. The electrolyte is $(TEA)^+(BF_4)^-$ in acetonitrile.

sample. By way of example, a charge of 20 $mC/cm^2$ corresponds to a film about 1000 Å thick for polypyrrole, and 60 $mC/cm^2$ corresponds to a film of about 1000 Å for poly(3-methylthiophene).

Poly(3-methylthiophene) (PMeT)

Thin films of PMeT were electrochemically polymerized on sputtered Pt electrodes from an acetonitrile solution consisting of 0.5M 3-methylthiophene, 0.2M (tetraethylammonium tetrafluoroborate) ($TEABF_4$) with an anodic potential of + 1.4 to + 1.8 V versus the saturated calomel electrode (SCE). This reaction grafted oxidized blue PMeT films on to the electrode surface. The thickness of the film could be controlled by monitoring the electric charge transferred during polymerization, by extrapolating the relationship of 10 Å/mC-$cm^2$, as determined with a DEKTAK profilometer for films greater than a few hundred angstroms, to thinner films. After polymerization, the potential was reversed to -0.2 V/SCE to obtain the red, reduced, semiconducting state of the film. All experiments discussed in chapter 5.3 were performed using such reduced samples. The samples were subsequently rinsed with ethanol and dried in a stream of nitrogen.

## 4.3. Fabrication of Langmuir-Blodgett Films

Langmuir-Blodgett films are formed by a molecule such as stearic acid ($C_{18}H_{36}O_2$) containing a hydrophilic group (-COOH) at one end (head) and a hydrophobic tail. On a water surface, when the film is compressed and the surface pressure is constantly monitored, the hydrophobic group will be oriented away from the water. Thus, an oriented monolayer

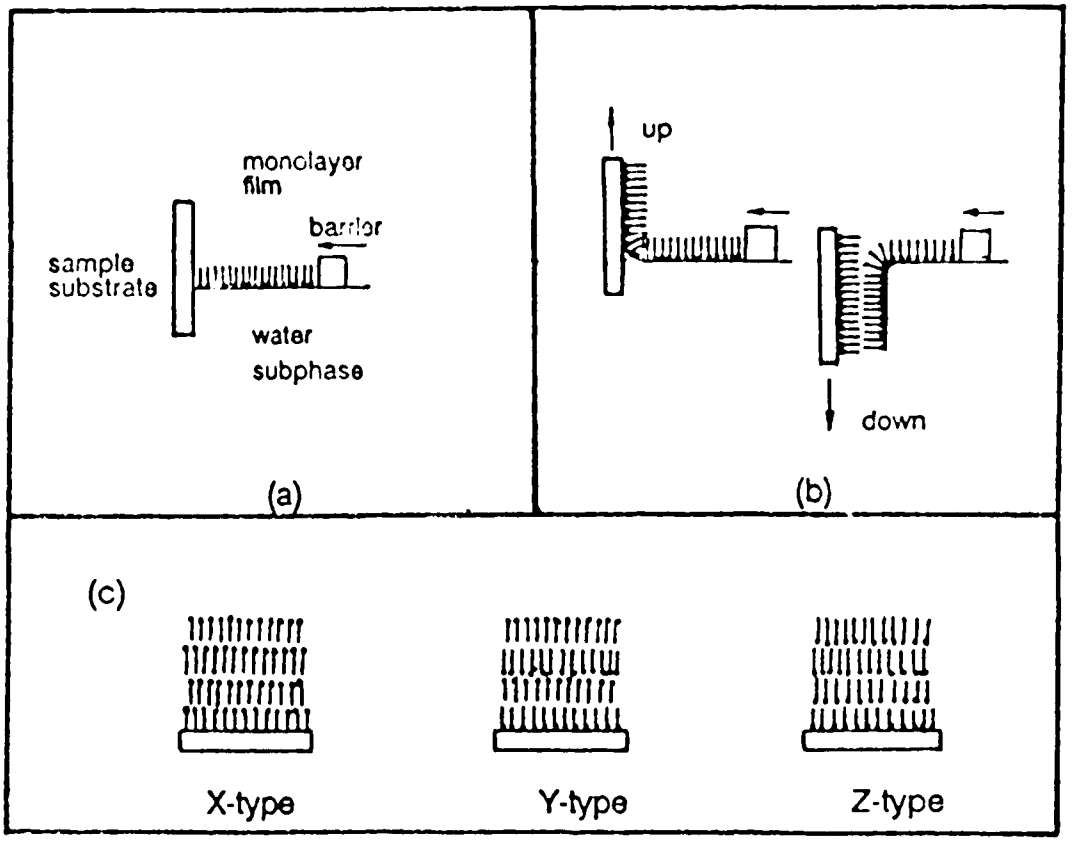


Figure 7. Preparation of a LB film. (a) A monolayer molecular film on a water surface. (b) Multilayer deposition on a solid substrate. (c) Three types (X, Y, and Z-type) of solid LB films.

molecular film is formed at the air-water interface.(Figure 7a) A solid film can be formed from this monolayer molecular film by dipping a substrate into the film on the water while maintaining a constant surface pressure. If, for example, a hydrophilic substrate is used, then a monolayer is deposited on the substrate when the substrate is moved upwards. A multilayer film can be built up by repeatedly dipping the substrate (Figure 7b). This head-to-head, tail-to-tail formation is called a Y-type film (Figure 7c). If deposition only takes place during the downward movement of the substrate, an X-type film is produced; deposition only during upward movement gives a Z-type film.[96]

The orientation of the tail and the uniformity of the film are very sensitive to the dipping speed, the pH of the subphase, the ion concentration in the subphase, and the water temperature. To make a high quality LB film, all these factors have to be carefully adjusted according to the nature of the molecular species. Slow dipping speeds of the order of 10 ~ 50 mm/min are normally required.

### 4.3.1. Isotherm Studies of LB Films at the Air-Water Interface

The surface pressure isotherm of a floating monolayer film (Langmuir-Blodgett film) at air-water interface must be carefully studied before fabricating a solid LB film on a substrate. The information provided by the isotherm can help to determine whether or not a solid LB film has been made. To produce a good floating monolayer on a water surface, the LB trough must be very clean and dust free. Highly purified water is normally used as a water subphase. The pH of the subphase is carefully adjusted, based on the nature of the material of the monolayer. The ion concentration in the subphase also strongly affects the isotherm curve (Figure 11).

The isotherm curve of stearic acid deposited from hexane solvent on a milli-Q water

subphase (Figure 8) clearly shows that there is a sharp break point ($A_c$) at about 20 ($Å^2$/mol) area per molecule. This point indicates the highest surface pressure a monolayer film can sustain. Beyond this point, the monolayer floating film collapses. There are two phase transitions, as indicated in Figure 8, from gas to liquid and from liquid to solid. In the solid region the film is closely packed with an area $A_0$ per molecule. The LB film is usually transferred to a substrate in this region at a surface pressure of about 30 mN/m.

In contrast to monomer materials such as stearic acid, in general, a polymer materials will not form a stable monolayer at the air-water interface. Therefore, there is no sharp break point in their isotherm curves. For example, Figure 9 shows an isotherm curve of ferrocene-substituted siloxane polymer. The surface tension increases gradually with the decrease of the area per molecule (Figure 7a). No stable film is formed on the water surface. This instability of the floating film on the water surface is basically due to an absence of hydrophilic moieties and the flexibility of long polymer chains which are usually in a coiled spring-like form. The polymer film can, therefore, be expanded or compressed easily on the water surface without inducing a phase transition.

To solve the difficulty of making a polymer LB film, a mixture of polymers and amphiphilic monomers was used. Figure 10 shows the isotherm curve of a mixture of poly(3-hexylthiophene) (P3HT) and stearic acid in a monomer ratio of 1:2. P3HT is not, by itself, sufficiently surface-active. However, a mixture of P3HT and stearic acid produces a sharp isotherm curve, which means that a stable monolayer film has been formed. The break point and the area per molecule of this film are close to that of pure stearic acid. The solid LB films of P3HT have been characterized by x-ray diffraction.[97]

The ion concentration and pH value of the subphase are two important factors in producing a high quality LB film, because they can change the chemical properties of the

organic compound on the water surface. By changing the pH value of the subphase,[13] the hydrophilicity of the molecules can be varied, which may facilitate uniform spreading rather than the formation of small islands on the water surface, as well as adhesion to the substrate during dipping. Similarly, the change of the ion concentration in the subphase changes the segregation of an organic film on the water's surface[98] (Figure 11). The isotherm curve of the compound 4-[4-(N-n-dodecyl-N-methylamine)phenylazo]-3-nitrobenzoic acid (DPNA) with $Cd^{++}$ has a sharp slope increase at 45 $Å^2$/molecule. Unlike pure DPNA, which has a broad phase transition near a surface pressure of 25 mN/m, the DPNA with $Cd^{++}$ has a break point at pressure 60 mN/m, implying that it has formed a more rigid solid film on the water surface. In the water subphase, the head group (COOH) of DPNA forms $(COO)^-$ and $H^+$, resulting a negatively charged $(DPNA)^-$ and $H^+$. The $Cd^{++}$ ions in the water subphase couple two $(DPNA)^-$ molecules with $Cd^{++}$. This coupling effect increases the stability of the DPNA molecules and, consequently, a rigid monolayer film forms on the water surface. This new conformation of the material is the cause of the difference between the isotherm curves of DPNA with and without $Cd^{++}$.

Water temperature is also an important factor in determining the quality of the LB films. Figure 12 shows a set of isotherm curves of siloxane mixed with stearic acid at a monomer ratio of 3:10 at temperatures 18°C, 25°C, and 30°C. Clearly, the isotherm curve shifts towards smaller area per molecule with increasing temperature, indicating that the monolayer film on the water surface changes from an expanded to a condensed phase with increasing temperature. This phase transition from an expanded to a condensed monolayer was observed by Nakahara *et al.*[99]

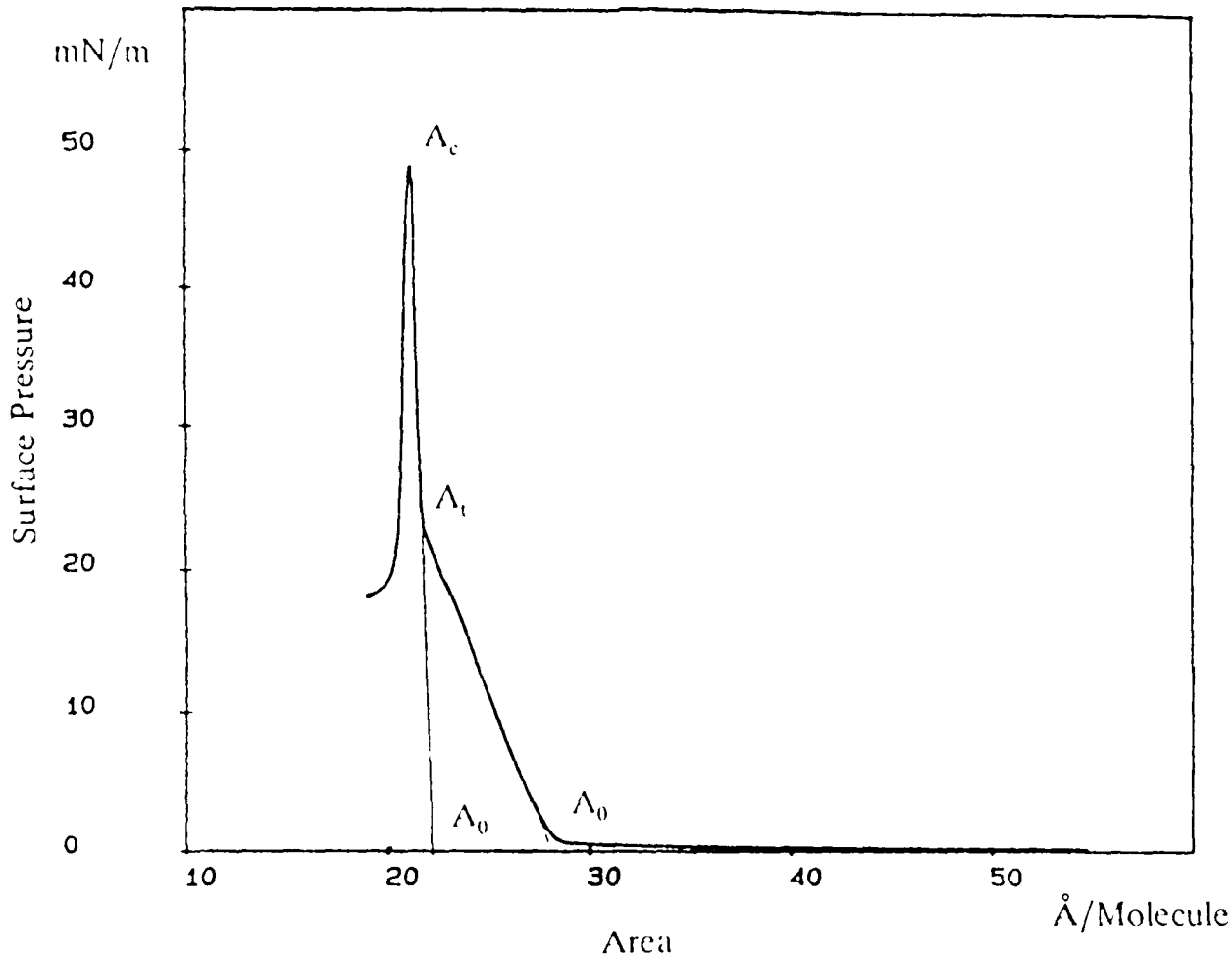


Figure 8. Pressure-area isotherm of stearic acid. $A_c$ indicates the break point of a monolayer film at the air-water interface; $A_0$ indicates the area per molecule covered by a closely packed monolayer film; $A_t$ designates the transition from liquid phase to solid phase.

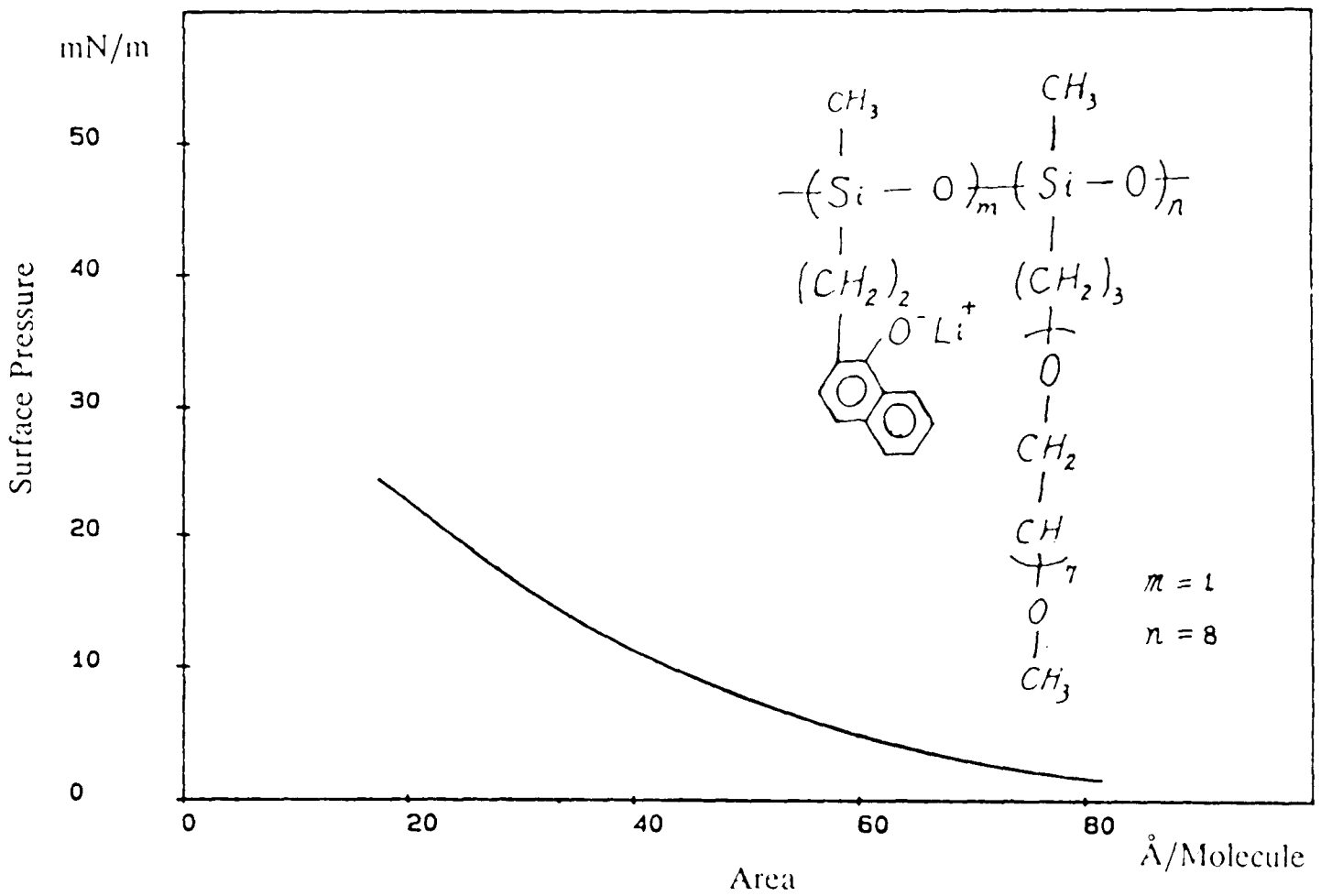


Figure 9. The pressure-area isotherms of ferrocene-substituted siloxane polymers show that they do not form a stable monolayer at the air-water interface.

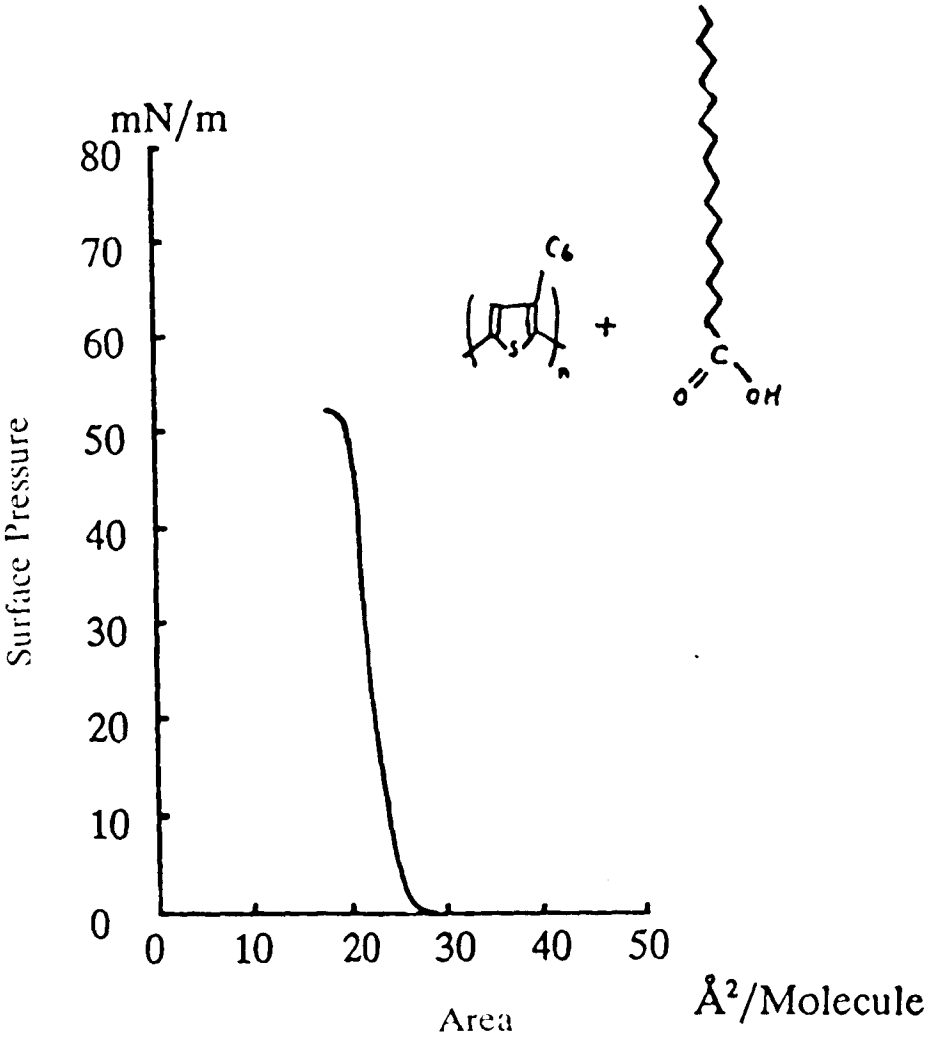


Figure 10. Pressure-area isotherms of poly(3-hexylthiophene) (PHT) mixed with stearic acid in 1:2 ratio. The break point is at pressure of 53 mN/m. The solid LB film is normally fabricated at pressure of 25 mN/m.

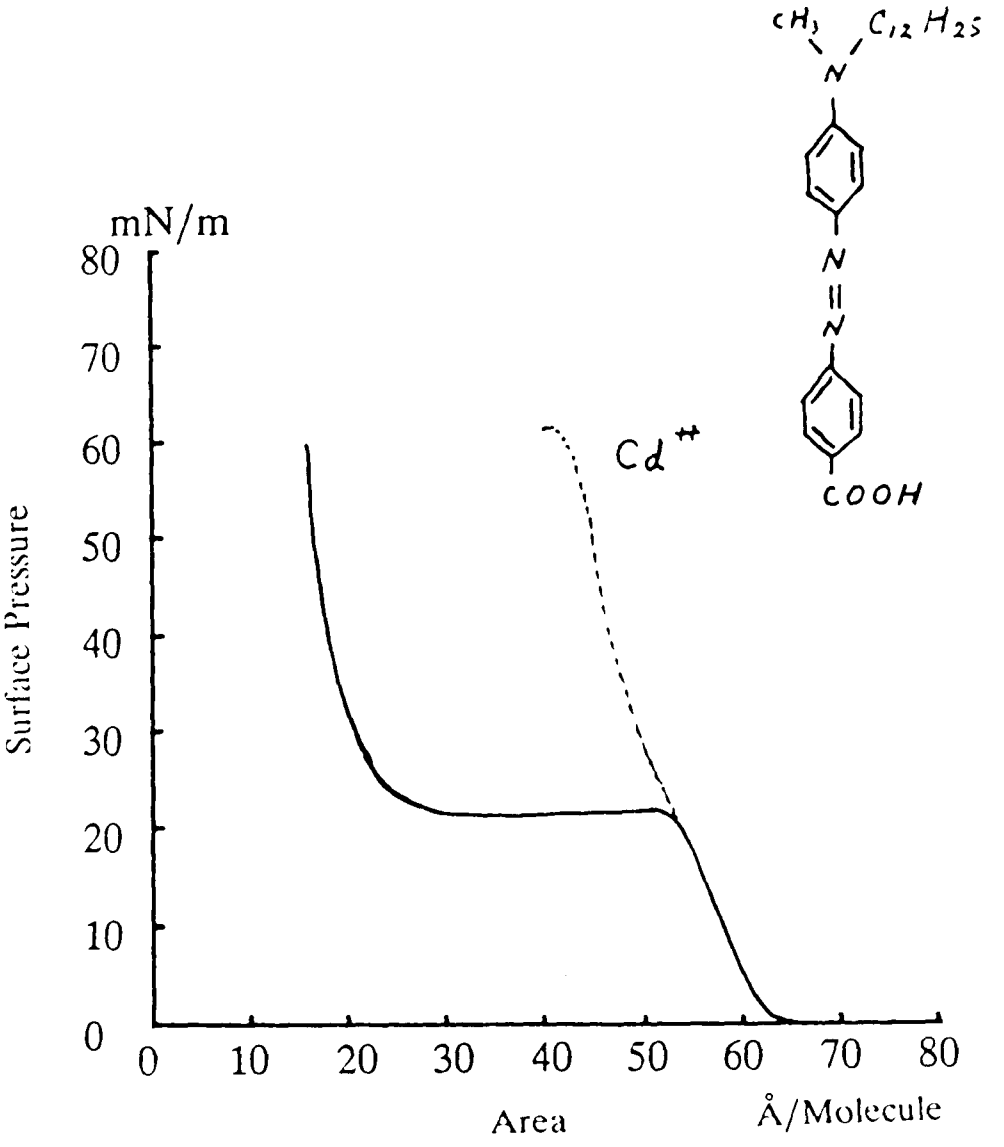


Figure 11. Pressure-area isotherms of DPNA and of DPNA with $Cd^{++}$. Unlike the isotherm of pure DPNA which has a breaking point at a pressure of 22 mN/m, the isotherm of DPNA with $Cd^{++}$ has a sharp slope and a high breaking pressure of about 60 mN/m, indicating that a stable monolayer film has formed at the air-water interface.

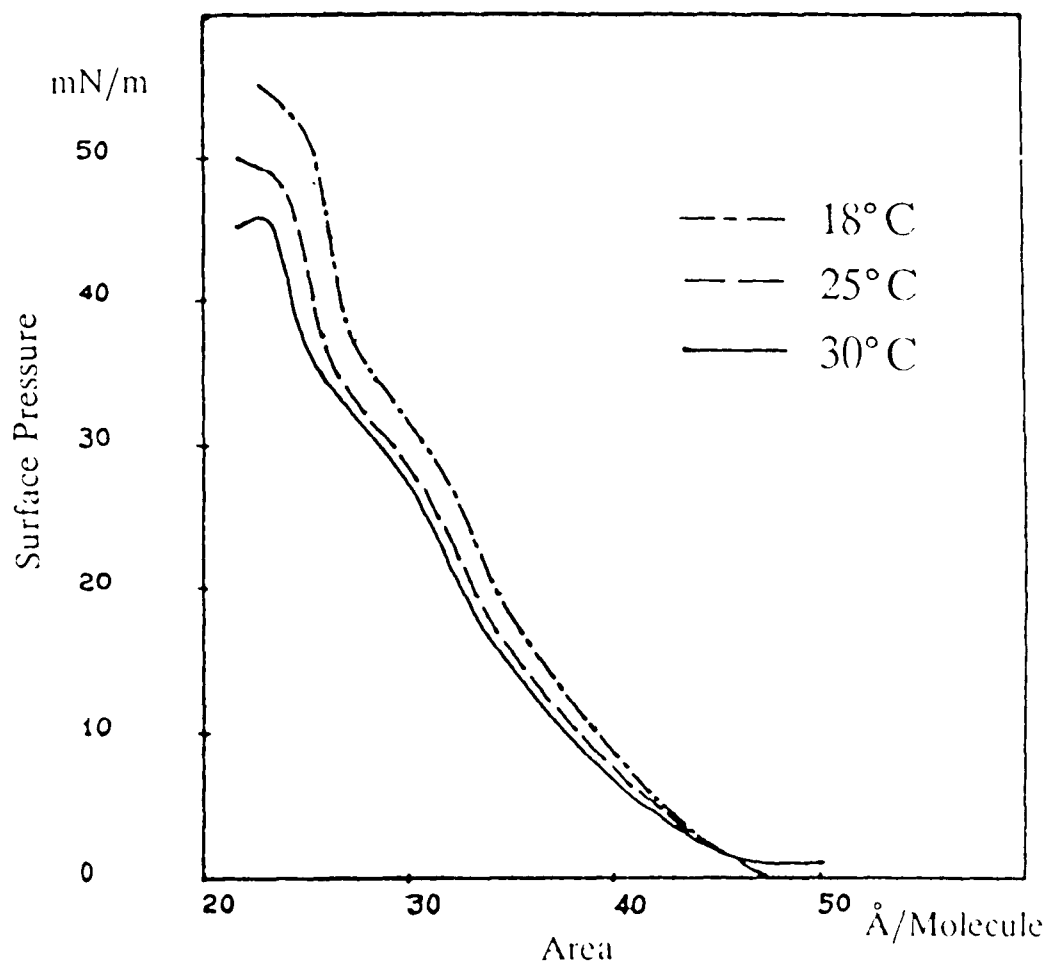


Figure 12. Pressure-air isotherms of polysiloxane mixed with stearic acid at a monomer ratio of 3:10. The isotherm curve shifts towards decreasing area per molecule with increasing temperature.

4.3.2. Fabrication of Solid LB Films

The technical procedure of fabricating a solid LB film was described in the introduction of this chapter (Figure 7). However, the setting of parameters and the substrate treatment differ, depending on the individual organic compound. The substrate treatment can generally be divided into two cases: metallic, such as platinum, and non-metallic, such as glass. For each case, the substrate surface can be chemically treated to render the surface hydrophilic or hydrophobic. A special substrate treatment is essential to fabricate a solid LB film. The following procedures are for several organic compounds.

Poly(3-hexylthiophene) (P3HT)/stearic acid

A LB film of P3HT mixed with stearic acid at a 1:2 ratio with a concentration of 0.2 mg/ml in chloroform solvent was transferred at a surface tension of 25 mN/m at 30°C in the subphase of Milli-Q purified water with $CdCl_2$ ($2x10^{-4}$ molar) ion concentration. The glass substrate was cleaned with detergent, then treated with $HNO_3$ (50/50), and NaOH ($10^{-3}$ molar) ultrasonically for 20 minutes each. After treatment, the glass substrate is expected to be hydrophilic. For the first layer, the dipping speed is set at 10 mm/min with the barrier speed at 7 mm/min. A waiting time of about two hours or longer is necessary for the layer to dry and to ensure a good transfer ratio for second or subsequent layers. The transfer ratio for all the layers were basically maintained at 0.95-1.0. A thin LB film transferred uniformly on a glass substrate has a reddish color, the darkness of which is a rough optical estimate of the thickness of the film.

4-[4-(N-n-dodecyl-N-methylamine)phenylazo]-3-nitrobenzoic acid (DPNA)

A LB film of DPNA was made to study its non-linear optical properties. A solution of DPNA is used with 0.5 mg/ml concentration in chloroform ($CHCl_3$) in the subphase of milli-Q purified water with $CdCl_2$ ($10^{-3}$ molar) at pH 6.8. The glass substrate is treated with chloroform and methanol ultrasonically for 20 minutes each. The glass surface is hydrophilic after this treatment. A Y-type LB film was transferred at a surface tension of 24 mN/m at a temperature of 29.7°C with a dipping speed 10 mm/min with the barrier moving at a speed of 7 mm/min. After the first layer was deposited, the film was dried with $N_2$ gas. The transfer ratio remained at 1.07 for the first layer and the following layers. For a Z-type LB film, because of the amphiphilic nature of the molecules, the film will be made alternately head (hydrophilic group) to tail (hydrophobic group) (see Figure 7c). The Z-type film was transferred at a surface pressure of 15 mN/m with a dipping speed of 20 mm/min with the barrier moving at 25 mm/min. To make multilayer films for the second harmonic generation, a noncentrosymmetric structure is required; therefore, a Z-type film is required.

# Chapter 5. Experimental Results and Discussion

We used EXAFS, NEXAFS, and FTIR techniques to study various ion and electron conducting polymers, and Langmuir-Blodgett films to determine: the microscopic structure and transport properties of ion-conducting polymers (PEO/KI); the ordering of thin films of the electron conducting polymer PMeT and dependence of the ordering on thickness; and the orientation of LB films and interactions between monolayer films and metallic substrates. We also studied the superlattice structure of LB films with x-ray diffraction, as well as the temperature dependence of the structure of LB films.

## 5.1. Ion Conducting Polymers

The ion conducting polymer, poly(ethylene oxide) mixed with alkali salts, e.g. potassium iodide (PEO/KI), was studied by EXAFS and NEXAFS spectroscopies. Recently, it was found that poly(ethylene oxide) can form solid solutions with alkali metal salts, resulting in ionic conductivity. The conductivity of PEO complexes increases with increasing temperature. However, the relationship between the conductivity of PEO and its microscopic structure is not fully understood. To improve the conductivity of PEO complexes, we studied the microstructure of PEO with EXAFS and NEXAFS techniques.

### 5.1.1. EXAFS Study of PEO/KI

The conductivity of PEO/KI increases at elevated temperatures and there is a phase

transition at about 60°C (Figure 1). This phase transition broadens as a function of the potassium concentration. It is known that polymer-salt complexes are normally mixtures of crystalline and amorphous phases, and that only the amorphous phase contributes significantly to conductivity. Unlike x-ray diffraction of pure PEO and pure KI which are crystalline, x-ray diffraction of PEO complexes ($PEO_8$/KI) show that they are completely amorphous (Figure 13). Therefore, EXAFS spectroscopy is the more suitable technique to study the microscopic structure of these materials.

Most measurements were performed at beam line X23B at the National Synchrotron Light Source at Brookhaven National Laboratory (Upton, New York), using a Si(200) double-crystal monochromator. The harmonic intensity was monitored and minimized by detuning the monochromator when appropriate. Some measurements were also made at beam line C3 at the Cornell High Energy Synchrotron Source at Cornell University (Ithaca, New York). The absorption was computed as $\ln(I/I_0)$, where $I_0$ is the x-ray flux incident on the sample and $I$ is the transmitted flux, both of which were measured by ionization chambers using a mixture of helium and nitrogen gas. The samples were prepared by casting a thin film on polyimide tape. Spectra were obtained at the potassium $K$-edge at 3612 eV in the range of 3500 eV to 3900 eV, and at 25, 50, 75, and 100°C.

Figure 14a shows the EXAFS spectrum at potassium $K$-edge of $PEO_4$/KI at 25°C. The spectrum is then edge-normalized by removing the background and converted to k-space by using equation 2. The experimental data $\mu(E)$ is fitted with the smooth curve $\mu_0(E)$(Figure 14b). The fine structure spectrum $\chi(k)$ is multiplied by a factor of $k^3$, to enhance the oscillations at high k value. Figure 14c shows the resulting EXAFS spectrum of $k^3\chi(k)$ in k-space.

Figure 15 shows the Fourier transformed spectra of $PEO_4$/KI at temperatures 25,

50, 75, and 100°C in radial space. It is clear that peaks A and B in figure 15 correspond to the first shell of backscatterers and the second shell of backscatterers, respectively. The first shell of backscatterers are oxygens around the potassium cation (K-O), and the second shell of backscatterers are iodines and/or carbons. The amplitude of peak A decreases with increasing temperature, while peak B is normalized. There are two possible reasons for this change of the amplitude. One possible cause is the Debye-Waller factor. In a completely amorphous phase, static disorder is no longer important and is not a function of temperature. However, the vibrational contribution to the Debye-Waller factor will reduce the amplitudes of both peak A (K-O) and peak B (which corresponds to iodine and carbon atoms). Because iodine is heavier than oxygen, the vibrational contribution due to iodine is less affected, and because carbon is lighter than oxygen, the vibrational contribution due to carbon is more affected. Therefore, on the average, the amplitude of peak A (K-O) may be reduced more than that of peak B at elevated temperature because of the heavy backscatterer iodine. A definitive conclusion can not be reached until a complete comparison is made of the experimental results with model compounds whose structures are known.

Another cause of the change in peak amplitude could be the symmetry of the structure, or the coordination number of oxygen around potassium could be reduced at elevated temperatures. In the amorphous phase, the flexible PEO chains allow the cations to migrate by exchanging ligands, i.e. K-O bonds are broken and reformed continuously (Figure 16). The structure of the complexes is not fixed and the oxygen coordination number can change at elevated temperatures, as can the structural symmetry about the K ion. The change of amplitude of the K-O peak suggests a reduction of the coordination number of oxygens around the potassium ion (i.e. a local environment change) that could reduce the

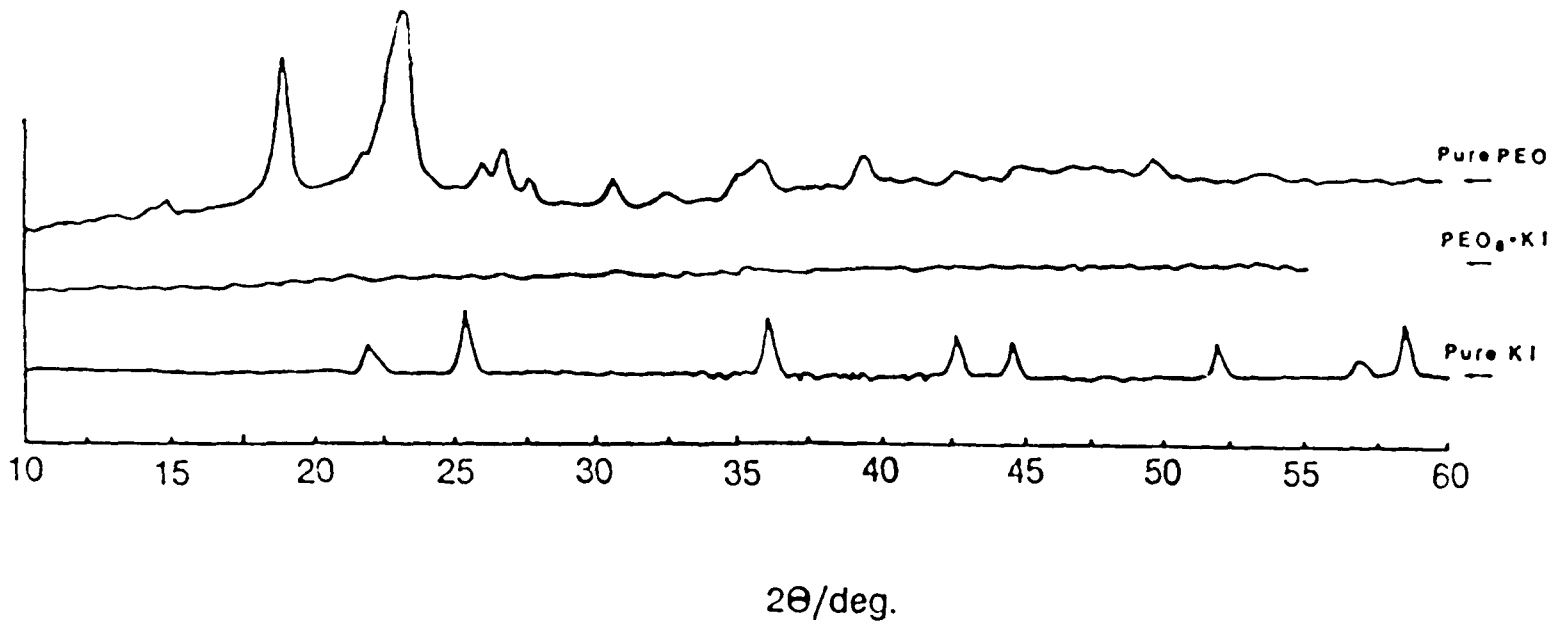


Figure 13. X-ray diffraction patterns of pure PEO, $P(EO)_8KI$ and pure KI salt, plotted as intensity versus scattering angle $2\Theta$, where $2\Theta$ is from 10° to 60°. The diffraction pattern of KI indicates a crystalline phase and the diffraction pattern of PEO indicates a mixture of crystalline and amorphous phases. In contrast, the diffraction pattern of $P(EO)_8KI$ shows only an amorphous phase

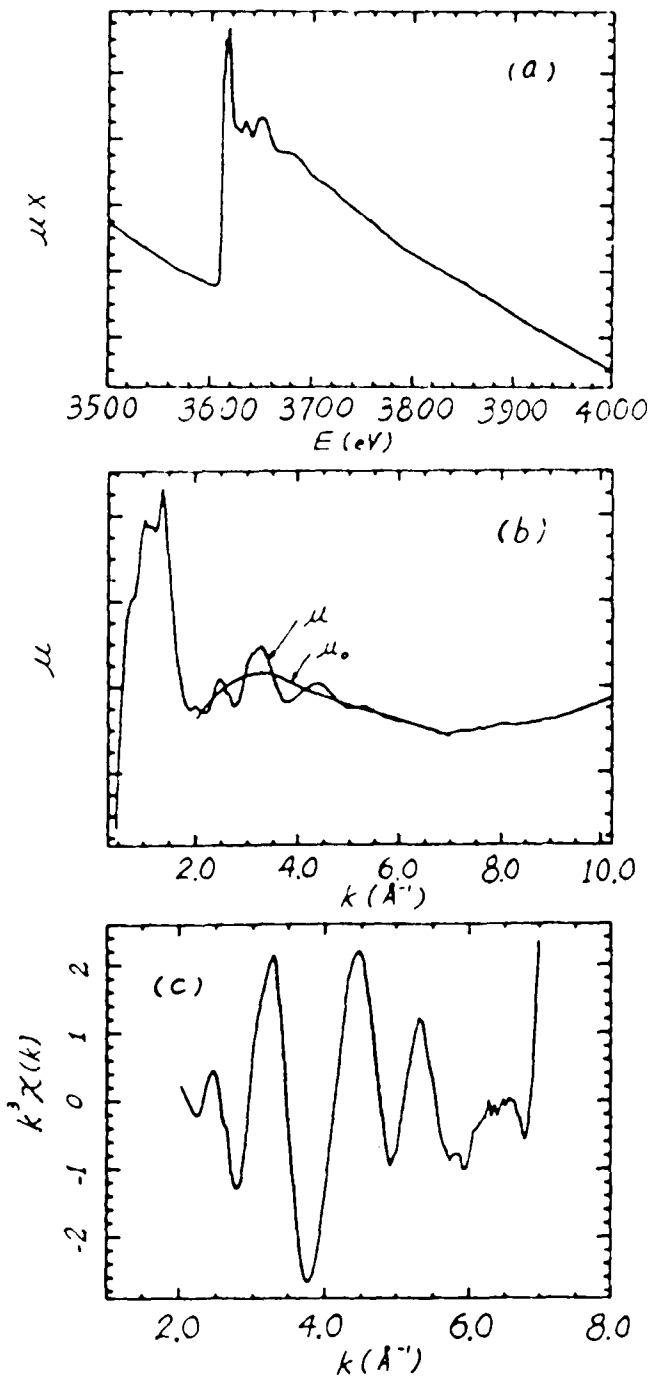


Figure 14. (a) The EXAFS spectrum of the *K*-edge of potassium in $P(EO)_4/KI$ at 25°C. (b) The edge normalized spectrum in K-space. The curve $\mu_0(E)$ is the best fit to the experimental curve $\mu(E)$. (c) The EXAFS spectrum of $k^3\chi(k)$ in *k*-space, where $\chi(k)$ is defined in equation 4.

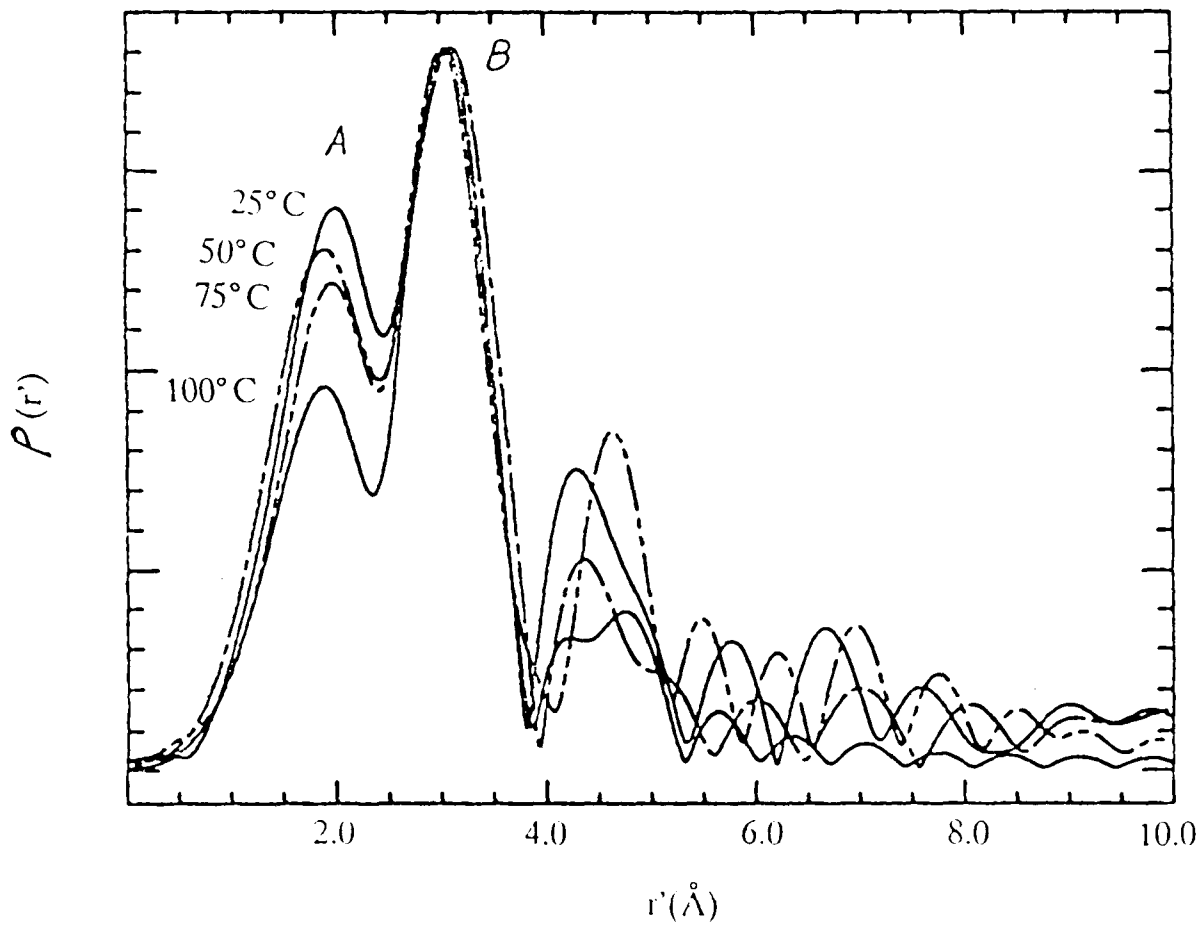


Figure 15. Fourier-transformed experimental data of PEO/KI (4:1) at 25°C, 50°C, 75°C, and 100°C. The amplitude distribution is plotted as a function of r in radial space. Peak A decreases with increasing temperature, while peak B is normalized.

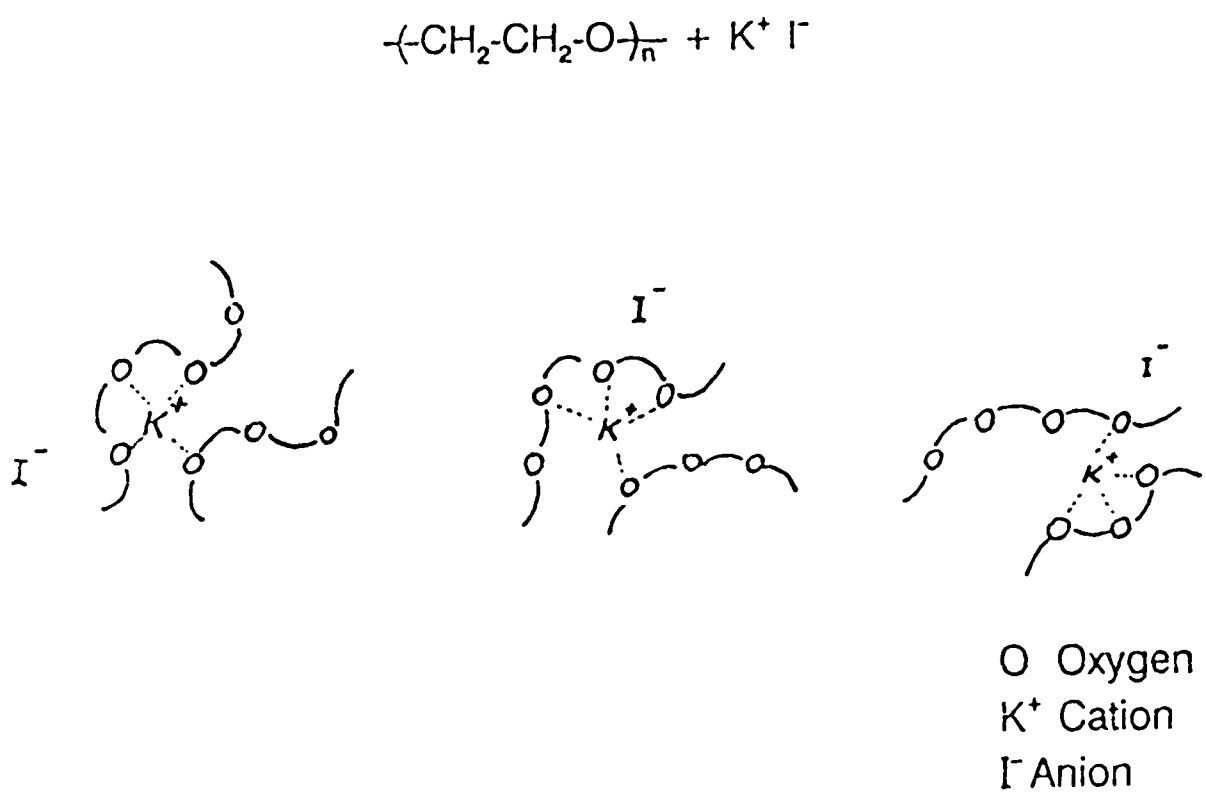


Figure 16. A schematic model of the structure of PEO/KI. The $K^+$ ion is coordinated by the oxygen atoms of the PEO [-$(CH_2$-$CH_2$-$O)_n$-] chains. The mobility of the $K^+$ ion is associated with ligand exchange.

activation energy for conductivity, and consequently, result in a phase transition in the conductivity of PEO/KI with temperature.

### 5.1.2. NEXAFS Study of PEO/KI

The technique of near-edge x-ray absorption fine structure (NEXAFS) spectroscopy is sensitive to local structural properties such as interatomic spacing and coordination number, even in the absence of long-range order. The technique is well suited to a study of the materials in amorphous phases, such as polymer-salt complexes. In order to have a better understanding of the ionic conductivity of the mixture of poly(ethylene oxide) and potassium iodide (PEO/KI), we used NEXAFS spectroscopy to study the microscopic structure of PEO/KI polymer complexes in the ratios of 4:1, 8:1, and 20:1 ethylene units to $K^+$ at the temperatures 25, 50, 75, and 100°C.

The temperature dependence of the NEXAFS spectra above the *K*-edge of potassium in the PEO/KI complex was systematically studied. The experimental results were obtained under the same environment as the EXAFS studies of PEO/KI (discussed in section 5.1.1). The observed NEXAFS spectra exhibit important changes in intensity with temperature and KI salt concentration, which we interpret by comparison with reference systems in which $K^+$ is coordinated with a well-defined number of oxygen atoms ranging from 3 to 6. We conclude that the observed changes in the near-edge region are due to breaking of the symmetry of the local electric field in the vicinity of the $K^+$ ion caused by a reduction in the oxygen coordination number with increasing temperature.

Figure 17 shows the x-ray absorption spectra above the *K*-edge of potassium in (a) KI, and (b) a PEO/KI complex with a 20:1 oxygen:potassium ratio at 25 and 100°C. The large "white line" feature evident above the edge is due to dipole-allowed transitions to final

states of *p* symmetry,[100,101] and its prominence indicates the high density of such states in the PEO/KI complex. The KI spectra are the same at both temperatures as expected, because the salt undergoes no phase transition in this temperature range. The spectra of the PEO/KI complex exhibit little temperature dependence, which indicates a lack of important structural or electronic changes with temperature in the vicinity of potassium at this low concentration.

In contrast to the lack of changes observed at low salt concentration, there are significant temperature effects at higher concentrations. Figure 18 shows the NEXAFS spectra of PEO/KI with an oxygen:potassium ratio of 4:1 at four different temperatures. The single broad white line in the 20:1 PEO/KI spectra has split into two peaks, labeled B and C, at about 4 and 7 eV above the absorption edge. The lower energy peak, B, increases with increasing temperature at the expense of the higher energy peak C; indeed, peak B becomes the dominant peak at 100°C. The feature labeled A remains unchanged from the spectrum corresponding to the 20:1 complex.

The NEXAFS spectra at four different temperatures for the intermediate salt concentration of 8:1 oxygen:potassium ratio are shown in Figure 19. The temperature dependence is similar to that observed in the 4:1 complex; that is, peak B increases with increasing temperature. However, the magnitude of these changes is significantly less in this case.

The interpretation of these spectral changes is complicated by the fact that it is not appropriate to assign individual spectral features to particular transitions for potassium *K*-edge NEXAFS spectra, as is commonly done for low Z atoms such as carbon and oxygen.[102] To relate these spectral changes to the microscopic structure of the PEO/KI complex, we examined the spectra of selected reference systems.[101] Figure 20 shows the

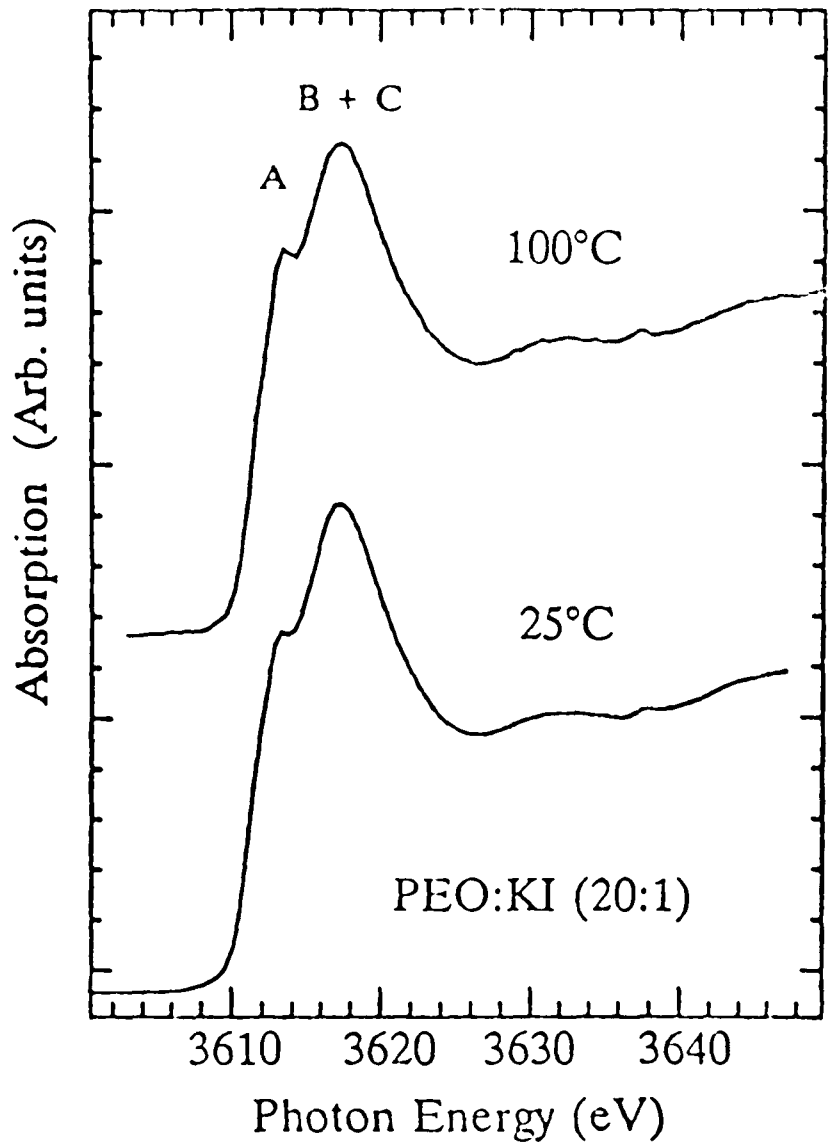


Figure 17. The NEXAFS spectra of the *K*-edge of potassium in $P(EO)_{20}/KI$ at 25°C and 100°C.

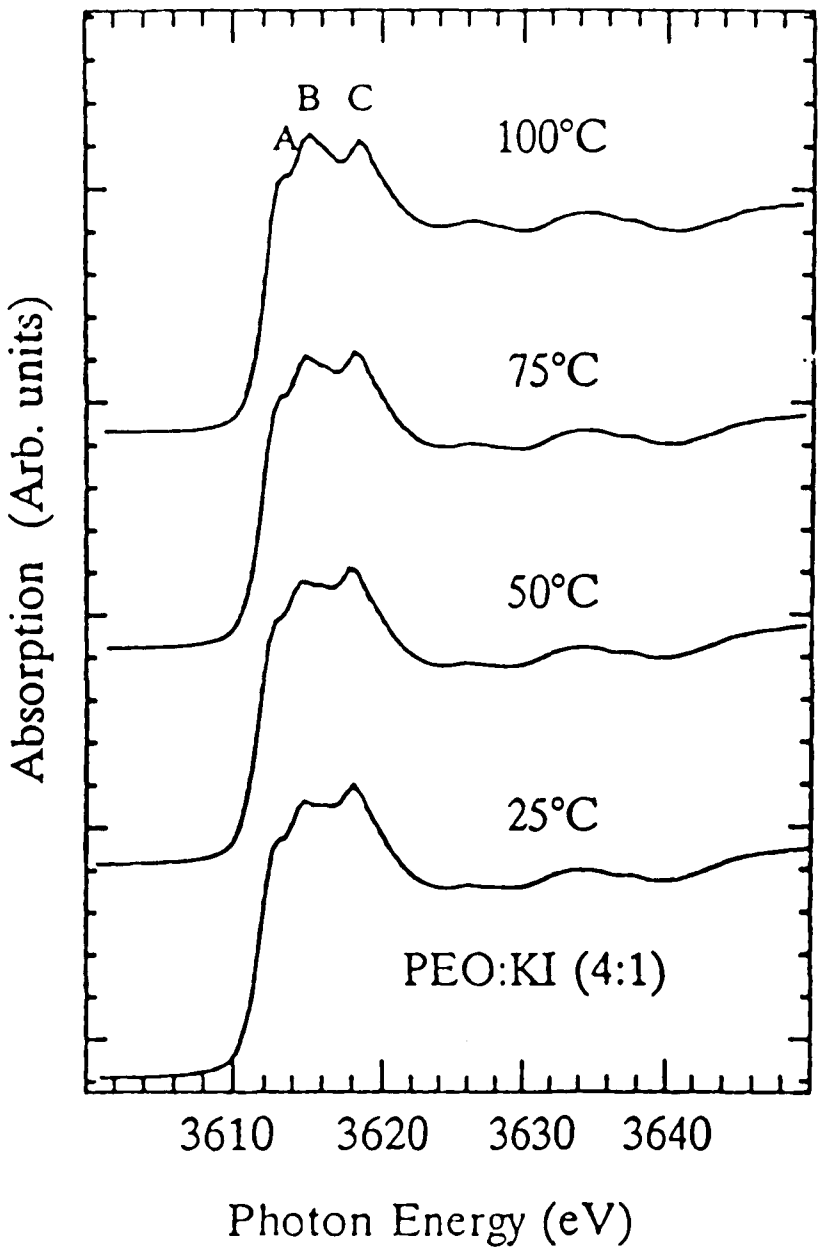


Figure 18. The NEXAFS spectra of the *K*-edge of potassium in $P(EO)_4/KI$ at 25°C, 50°C, 75°C, and 100°C.

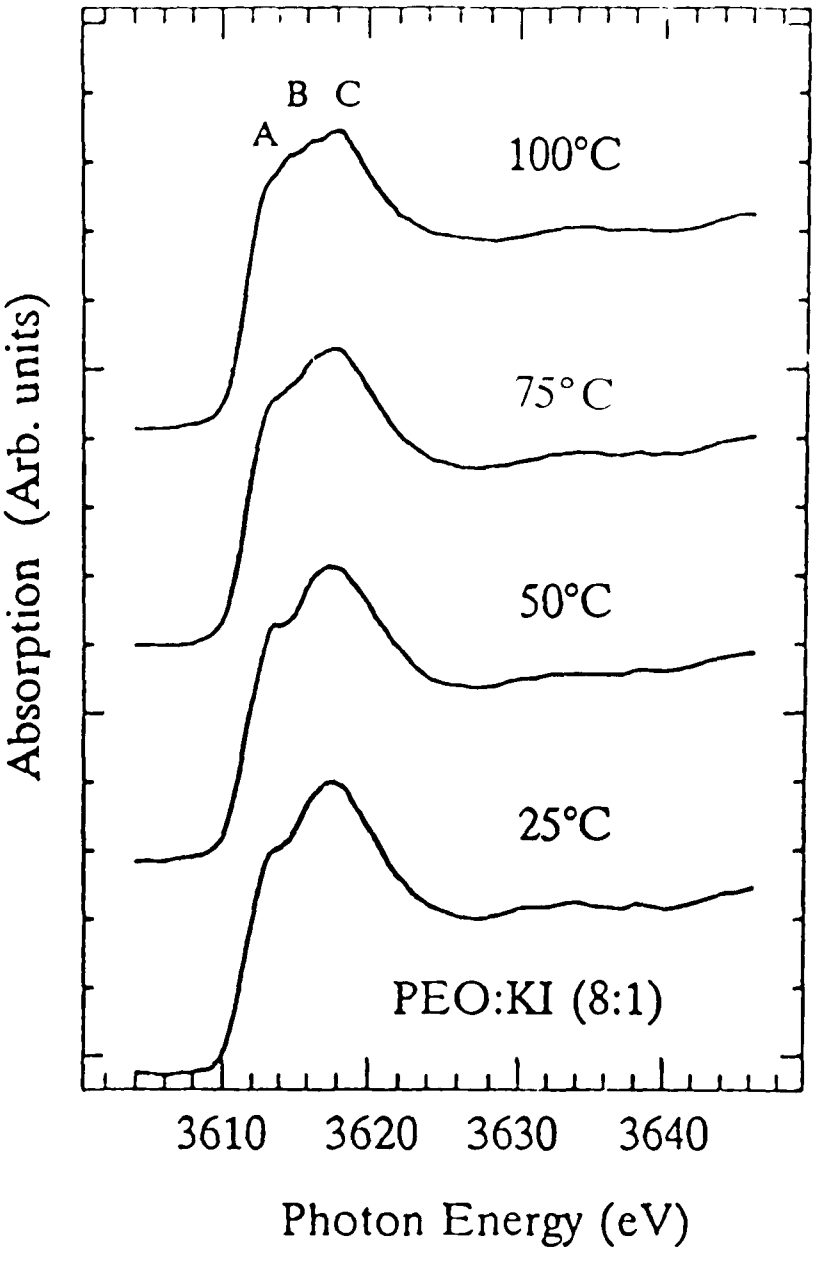


Figure 19. The NEXAFS spectra of the *K*-edge of potassium in $P(EO)_8/KI$ at 25°C, 50°C, 75°C, and 100°C.

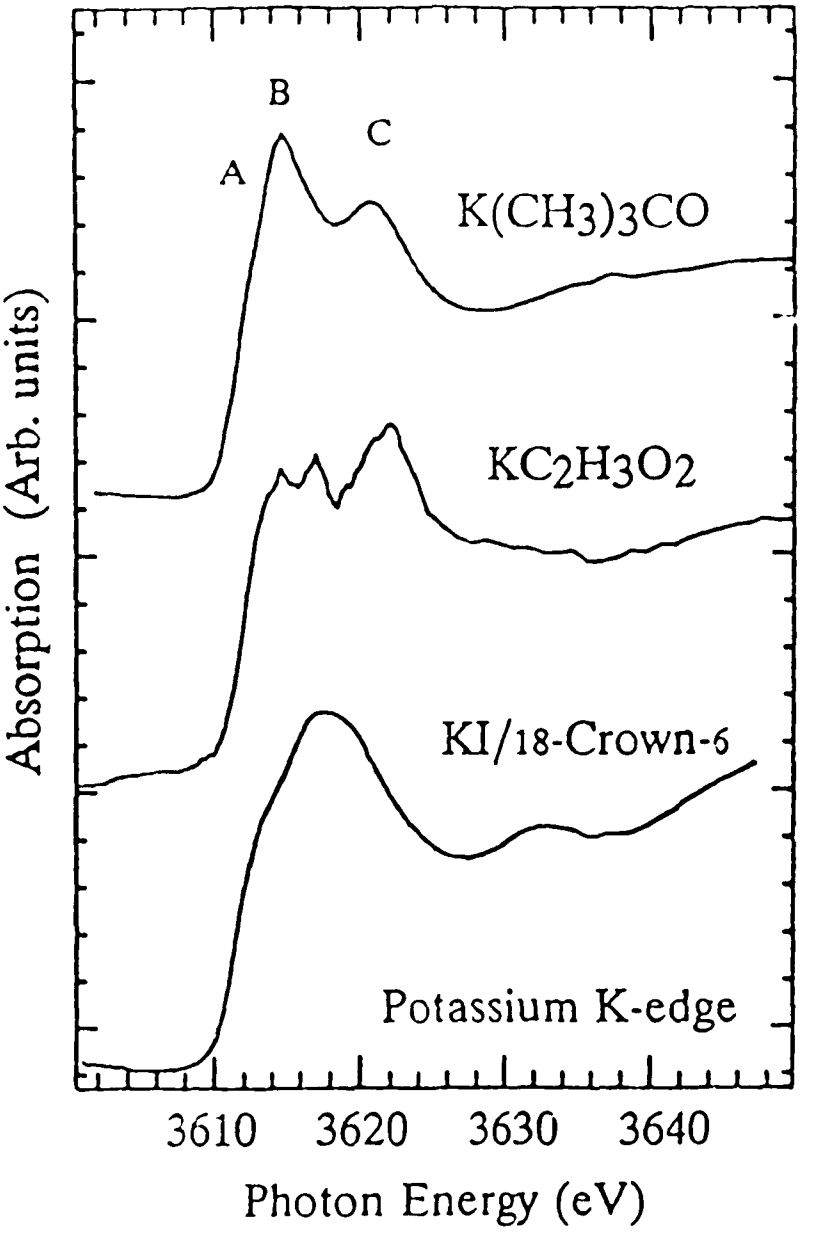


Figure 20. The NEXAFS spectra of the *K*-edge of potassium at 25°C in several reference compounds: $(CH_3)_3COK$, $C_2H_3O_2K$, and dibenzo-18-crown-6/KI.

spectra of three reference systems, namely $(CH_3)_3COK$, $KC_2H_3O_2$, and KI-18-crown-6 in which the potassium is coordinated with 3 to 6 oxygen atoms. The potassium *tert*-butoxide [$(CH_3)_3COK$] forms a terameric structural unit with potassium and oxygen atoms at alternate corners of slightly distorted cubes, surrounded by the *tert*-butyl groups along the diagonals.[103] The $K^+$ ion is coordinated with three oxygen atoms at the nearest corners of the cube with a 2.56 Å bond length. No detailed crystallographic study of potassium acetate ($KC_2H_3O_2$) is available. However, an x-ray diffraction study[104] of the related compound sodium acetate ($NaC_2H_3O_2$) shows that the $Na^+$ ion is surrounded by six oxygens at distances of 2.35 to 2.67 Å. Two of these six oxygens belong to the same acetate ion, while the other four belong to four different acetate ions. Assuming that the crystal structure is similar, in potassium acetate the $K^+$ ions are coordinated with two nearest oxygens and four next-nearest oxygens. In the dibenzo-18-crown-6-KI complex, the $K^+$ ion, located at the center of a nearly co-planar ring of six oxygens,[105] is coordinated with six oxygens. It is apparent from figure 20 that as the oxygen coordination number decreases from 6 to 3 in the sequence KI-18-crown-6, $KC_2H_3O_2$, $(CH_3)_3COK$, the intensity of the higher energy peak C decreases relative to that of the lower energy peak B. Similar changes in the near-edge white line features above the potassium *K*-edge as a function of oxygen coordination number were observed by Spiro *et al.*[101]

We now consider what we may conclude from the spectral changes with temperature (Figure 18). Purely electronic factors, such as a change in the oxidation state of the absorber, will affect the shape of the absorption edge.[106] Since potassium has only one ionization state $K^+$, this effect may be ruled out. Rather, the observed changes are probably due to variations in the local structural environment of the $K^+$, that is, changes in the number and kind of atoms in its vicinity. Such changes affect the NEXAFS both directly,

by modifying the multiple scattering which gives rise to the near-edge structure, and indirectly, as changes in the local structure alter the hybridization and the symmetry of the molecular orbitals. In view of the decrease observed in the higher energy peak, C, (Figure 20) with decreasing oxygen coordination number, we conclude that the primary effect of increasing the temperature of the PEO/KI system at high salt concentrations is to reduce the oxygen coordination number around the K cation. As this reduction occurs in the same temperature region over which the activation energy of conductivity decreases, we associate this structural change with a reduction in activation energy.

The changes in the oxygen coordination number are associated with the breaking of symmetry around the K ions. As pointed out, there is no simple correspondence between individual features in the absorption spectrum and the local environment of the absorption atom. Rather, the local environment indirectly affects the shape of the absorption spectrum. The photoabsorption matrix element is determined, in view of the dipole selection rule, by the spatial overlap of the initial $l=0$ (K) core state with the $l=1$ angular momentum components of the unoccupied K and ligand (O) orbitals. Changes in the local environment affect the intermixing (hybridization) of these orbitals, and thus, the overlap. Moreover, changes in the local environment affect the crystal field experienced by these orbitals. When the absorbing atom is in a highly symmetric site, these orbitals may be energy degenerate, but as the symmetry decreases, the crystal field experienced by each of the degenerate states will be different and the degeneracy will be lifted, giving rise to an energy splitting of the absorption edge. This effect was observed, for example, by Petiau and Calas,[107] who found a splitting of the *K*-edge of Fe in a series of compounds, which increases as the Fe site symmetry decreases, and by Balzarotti,[108] who observed a splitting of the Ti *K*-edge due to breaking of the degeneracy of the $t_{2g}$ and $e_g$ levels in several Ti-based compounds.

The effect of symmetry can be seen clearly in the three reference spectra of Figure 20. In the 18-crown-6/KI system, the K ion is located at the center of a sixfold ring of oxygen atoms, a relatively symmetrical arrangement in which there is little energy difference between the various orbitals. In this system, the near-edge region consists of a single broad peak. In crystalline $KC_2H_3O_2$, each K ion has two nearest neighbor oxygens and four next-nearest neighbor oxygens. Although the coordination number is still 6, the K site symmetry is reduced relative to the 18-crown-6/KI system, since all but two of the O atoms are further from the K ion. This broken symmetry splits the "white line" into two peaks B and C. In crystalline $K(CH_3)_3CO$, each K ion coordinates with three O ions which are all on one side of the K ion. In this highly asymmetric situation the intensity of peak C is decreased relative to peak B.

The near-edge spectrum of K complexed with PEO at a low concentration of 20:1 oxygen:potassium (Figure 17) most nearly resembles the 18-crown-6/KI spectrum of figure 20, indicating that, in this case, the K cations are similarly coordinated with oxygens in an arrangement which, statistically, has high symmetry. This conclusion agrees with the standard model of polymer-salt complexes, where intermolecular and intramolecular complexation by highly flexible polymer chains allows a variable degree of complexation.[109] At low salt concentrations, it is possible for the PEO polymer chains to provide enough oxygen atoms to preserve the high symmetry of the K site, even at elevated temperatures. Consequently, no splitting of the near-edge feature is observed and there is little change with temperature. On the other hand, at higher salt concentrations the number of oxygen atoms for each K ion is limited. Particularly at elevated temperatures the polymer chains cannot provide enough oxygen atoms to preserve the symmetry of the K site.The resulting asymmetry splits the degeneracy of the K-O orbitals, and correspondingly,

produces a split near-edge peak, as observed in the spectrum of the 4:1 PEO:KI complex of figure 18 at room temperature. As the temperature is increased, the increase in free volume associated with the increased local mobility of the polymer chains further reduces the number of oxygens adjacent to the K ion, and hence, the symmetry of the K site. The effect (Figure 18), is to increase the intensity of the lower energy peak B. Just as in the reference spectra of Figure 20, the intensity of the lower energy peak B increases as the site symmetry decreases.

The shoulder labeled A, on the other hand, does not change with the changing oxygen environment of the potassium ion, and therefore, is probably not associated with a degenerate state. A similar, but less dramatic, effect is observed in the intermediate concentration 8:1 complex of Figure 19, in which case the polymer chains have more ability to provide the K ions with oxygens, resulting in increased symmetry of the complexation. We conclude, therefore, that the oxygen coordination number of the $K^+$ ions decreases at elevated temperatures. This decreased coordination could increase the mobility of the $K^+$ ions and be responsible for the lower activation energy of conductivity of the PEO:KI complex at higher temperatures. However, there was no dissolution and recrystallization of the KI at such temperatures for the highly concentrated 4:1 system. The near-edge features, even at 100°C, do not resemble those of the pure salt. Moreover, our x-ray diffraction studies revealed no evidence of crystalline KI.

In conclusion, we have found that the primary effect of increasing the temperature of the PEO/KI complex, particularly at high salt concentrations, is to reduce the oxygen coordination number of the K ion. This reduced K-O complexation and chain interlinking may be responsible for the lower activation energy of ionic conductivity at elevated temperatures. These results demonstrate the power of the NEXAFS technique to

investigate amorphous systems.

### 5.1.3. A Comparison of EXAFS and NEXAFS Studies

EXAFS is a useful technique to probe the local environment of the absorber. By comparing the spectrum of the sample with the spectrum of model compounds of known structure, one can obtain structural information of the sample, such as the coordination number $N_o$, bond lengths r, Debye-Waller factor $\sigma$, and energy shift E. Unlike x-ray diffraction, which requires that the sample has a long-range ordered structure, the EXAFS technique can be used to study disordered materials. However, EXAFS has its limitations when it is used to study polymeric materials. Most organic compounds consist of light elements such as H, C, O, and N. These are weak backscatterers. Therefore, the amplitude of the structural oscillations in the spectrum declines rapidly within a very short energy range: this is a major difficulty in EXAFS studies of polymeric materials.

In contrast, the NEXAFS technique probes the probability of the transition from the ground state to partially occupied or unoccupied antibonding states. It provides information about local electron density, which can be used to determine the local geometry of atomic arrangements, such as interatomic spacing and coordination number. In our experiment, the method of comparing the NEXAFS spectra of the unknown sample, to the NEXAFS spectra of model compounds with known structures is similar to that of EXAFS. The assumption is that similar NEXAFS spectra are generated by similar structures. We observed that changes in the NEXAFS spectrum of PEO/KI at elevated temperatures correspond to the spectral changes of the model compounds with different coordination numbers of oxygen around the potassium ion. Therefore, we conclude that the coordination number of oxygen around potassium in PEO/KI changes with temperature, which explains

the change in the activation energy of conductivity. The results of the EXAFS studies of PEO/KI are also consistent with the oxygen coordination number about the K ion changing at elevated temperatures.

## 5.2. Langmuir-Blodgett Films

Langmuir Blodgett (LB) films have been studied extensively because of interest in their unique properties, such as a high degree of orientation on the molecular scale, and their potential applications as synthetic membranes, nonlinear optical elements, sensors and microelectronic devices. In our laboratory, Langmuir-Blodgett films have been fabricated with electrically conducting polymeric materials. The form has been on 3-alkylpyrrole and poly(3-alkylthiophene) mixed with stearic acid. The molecular orientation of LB films was studied with NEXAFS spectroscopy by comparing the spectra of LB films at normal incidence and nearly grazing angle incidence of the x-ray beam. The interaction between LB films and metallic substrates was observed using carbon *K*-edge NEXAFS spectra of 3-alkylpyrrole LB films on Pt-coated glass substrates. The superlattice structure of Y-type LB films was studied using x-ray diffraction. The temperature dependence of the layer structure of LB films was also studied by x-ray diffraction.

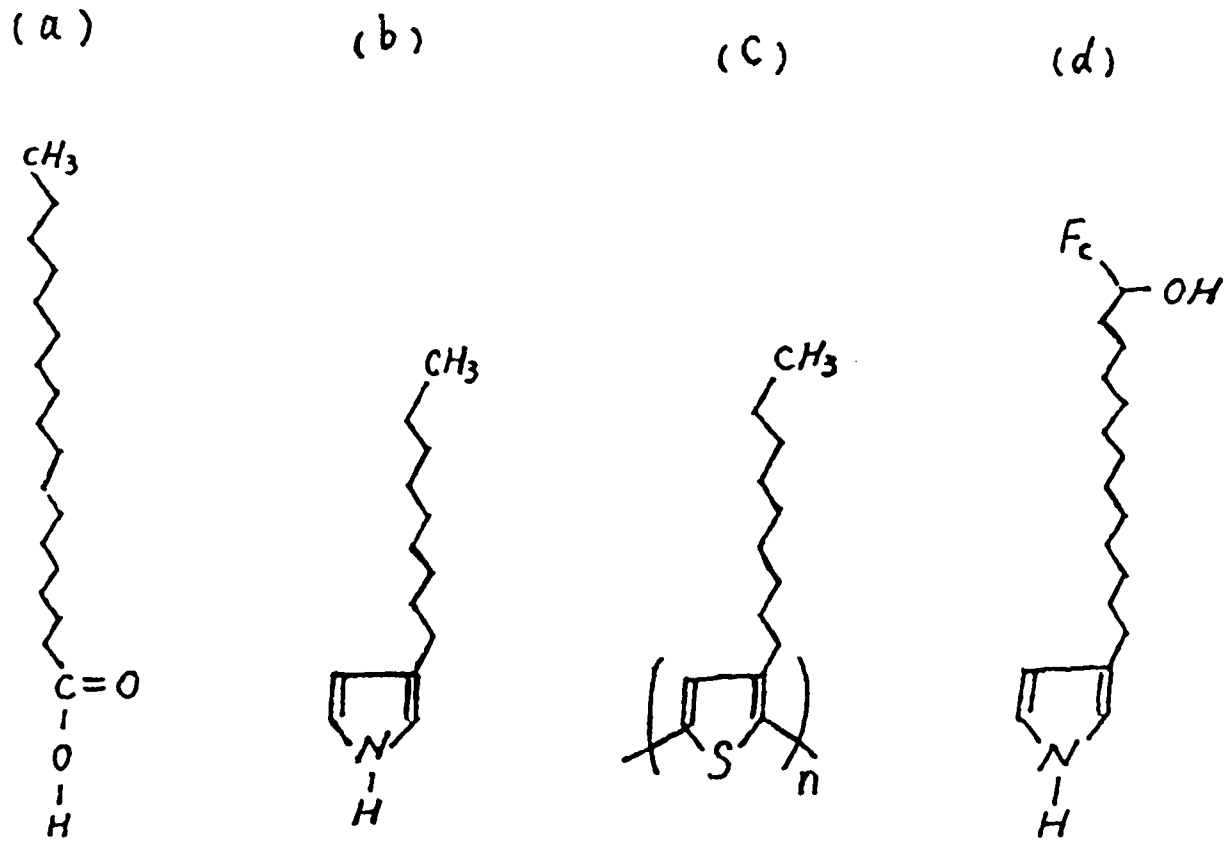


Figure 21. The molecular structure of (a) stearic acid, (b) 3-alkylpyrrole; (c) poly(3-alkylthiophene); and (d) ferrocene-derivatized 3-alkylpyrrole.

5.2.1. NEXAFS Study of the Orientation of LB Films

NEXAFS spectroscopy was used to probe the molecular orientation of LB films such as 3-n-hexadecylpyrrole (3HDP), 3-n-octadecylpyrrole (3ODP), copolymers of pyrrole and octadecylpyrrole, mixtures of poly(3-octadecylthiophene) (P3ODT) and stearic acid, and mixtures of poly(3-butylthiophene) (P3BT) and stearic acid.

The carbon K-edge NEXAFS spectra of hydrocarbon chains have been studied previously.[29,102] The resonance peaks corresponding to the $(C\text{-}H)^*$ and $(C\text{-}C)^*$ $\sigma^*$ transitionshave opposite polarization dependence. Comparing the spectra taken at normal incidence (**E** parallel to the substrate) and at grazing incidence (**E** perpendicular to the substrate), one can determine the orientation of the hydrocarbon chains with respect to the substrate, if the chains are highly ordered.

The NEXAFS studies were carried out on beam lines U-3 and U-14 at the National Synchrotron Light Source at Brookhaven National Laboratory. The NEXAFS spectra were obtained by total electron yield detection by measuring the sample current. The spectrum was normalized by the current from a gold grid placed in the incident beam.

3-n-hexadecylpyrrole (HDP)

The molecular structure of HDP is shown in figure 21b. The N-H bond in the pyrrole renders it surface active, which makes the pyrrole group a hydrophilic head group. There are sixteen C-C bonds along the hydrocarbon tail, and one C-C bond in the pyrrole head group. Therefore, the C-C bonds are predominantly oriented along the hydrocarbon tail, and the C-H bonds are perpendicular to the hydrocarbon tail. Figure 22a shows the carbon *K*-edge NEXAFS spectra of a single layer HDP monomer LB film with the incident x-ray beam at 90° (normal incidence), 45°, and 20° (nearly grazing incidence). In Figure

22a, with increasing incident angle of the x-ray beam the intensity of the 288.5 eV peak, which corresponds to transitions to the $(C\text{-}H)^*$ anti-bonding state, increases while the intensity of the 293.5 eV peak, corresponding to transitions to the $\sigma^*$ $(C\text{-}C)^*$ state, decreases. Table I lists the energies and proposed assignment of features in the carbon *K*-edge spectrum of HDP and ODP LB films. The observed intensity changes suggest that the hydrocarbon tails are highly ordered nearly normal to the sample's substrate. Figure 22b shows the C *K*-edge NEXAFS spectra of a 7-layer HDP monomer LB film. The orientational dependence of this multilayer film is similar to that of the single layer film, but the transition peaks of the multilayer film are more pronounced than that of the single-layer film, indicating that the multilayer film has a higher degree of angular dependence and that the hydrocarbon tails of the first layer may be tilted towards the substrate surface, as illustrated in Figure 23.

Octadecylpyrrole and Pyrrole/Octadecylpyrrole Copolymer

Figure 24 shows the carbon *K*-edge NEXAFS spectra of octadecylpyrrole (ODP) monomer (Figure 24a) and pyrrole/octadecylpyrrole copolymer (Figure 24b) LB films. Both samples are a single monolayer on a Pt substrate. The similarity of the spectra of ODP in figure 24a and the spectra of HDP in figure 22a indicates that the ODP monomer monolayer LB film is ordered but tilted from the surface normal, as is the HDP monomer LB film. However, the polarization dependence of the spectra for copolymer films has almost disappeared, suggesting that disorder was introduced during polymerization.

Ferrocene-derivatized Alkylpyrrole/3-hexadecylpyrrole

The carbon K-edge spectra of a 4-layer LB film of the mixture of ferrocene-

derivatized alkylpyrrole with a 12 carbon chain and 3-hexadecylpyrrole are shown in figure 25. The sample was made in a 1:5 ratio and deposited on a Pt substrate. Comparing the spectra taken with the x-ray beam at normal incidence and at grazing incidence, it is clear that the LB film is highly oriented. We note that the intensity of the $(C\text{-}H)^*$ peak increases with increasing incident angle of the x-ray beam while the intensity of the $(C\text{-}C)^*$ peak decreases. Since this mixture is composed of one ferrocene-derivatized alkylpyrrole to five hexadecylpyrroles, the hexadecylpyrrole must dominate the orientation dependence of LB film. The OH group at the ferrocene renders it less hydrophobic. Therefore, the initial orientation of the ferrocene-alkyl-pyrrole is unclear. However, NEXAFS spectra show a clear polarization dependence, indicating that both HDP and ferrocene-derivatized alkylpyrrole are well ordered, and the hydrocarbon tails are oriented nearly normal to the surface of substrate.

Poly(3-octadecylthiophene)/Stearic Acid and Poly(3-butylthiophene)/Stearic Acid

Figure 26 shows the carbon K-edge NEXAFS spectra of LB films of poly(3-ODT)/stearic acid (A) and poly(3-BT)/stearic acid (B) mixtures. The polythiophene is undoped. The energies and proposed assignments of the features are given in Table II. The spectra for poly(3-ODT)/ stearic acid in figure 26a show very strong polarization-dependence, with the highest intensity of the $(C\text{-}H)^*$ peak at normal incidence. This finding indicates that the hydrocarbon chains of the stearic acid are highly ordered and oriented along the surface normal.

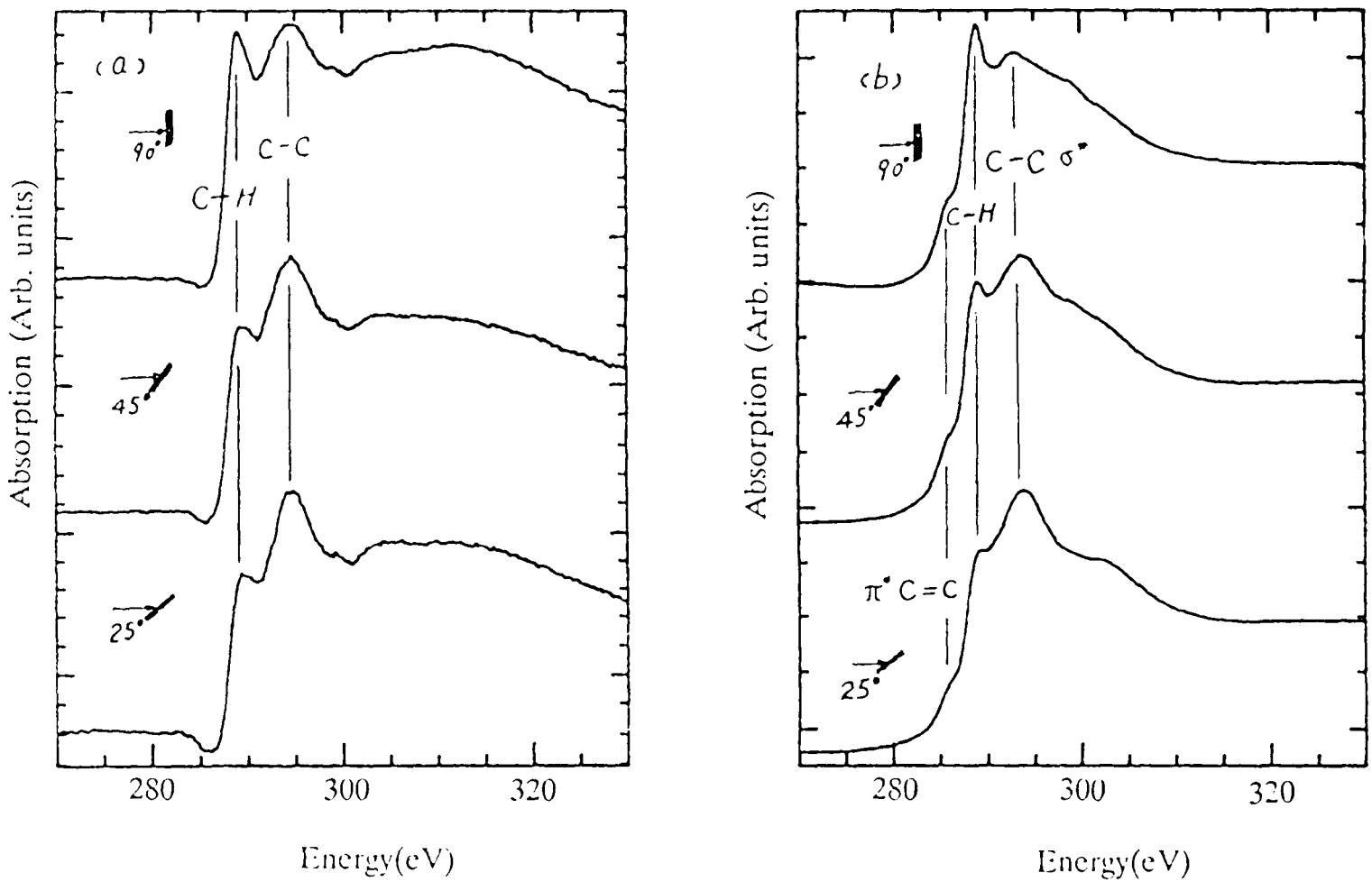


Figure 22. The carbon *K*-edge NEXAFS spectra of hexadecylpyrrole (HDP) LB film on Pt substrate (a) monolayer, and (b) 7 layers. The insets indicate the direction of the incident x-ray beam.

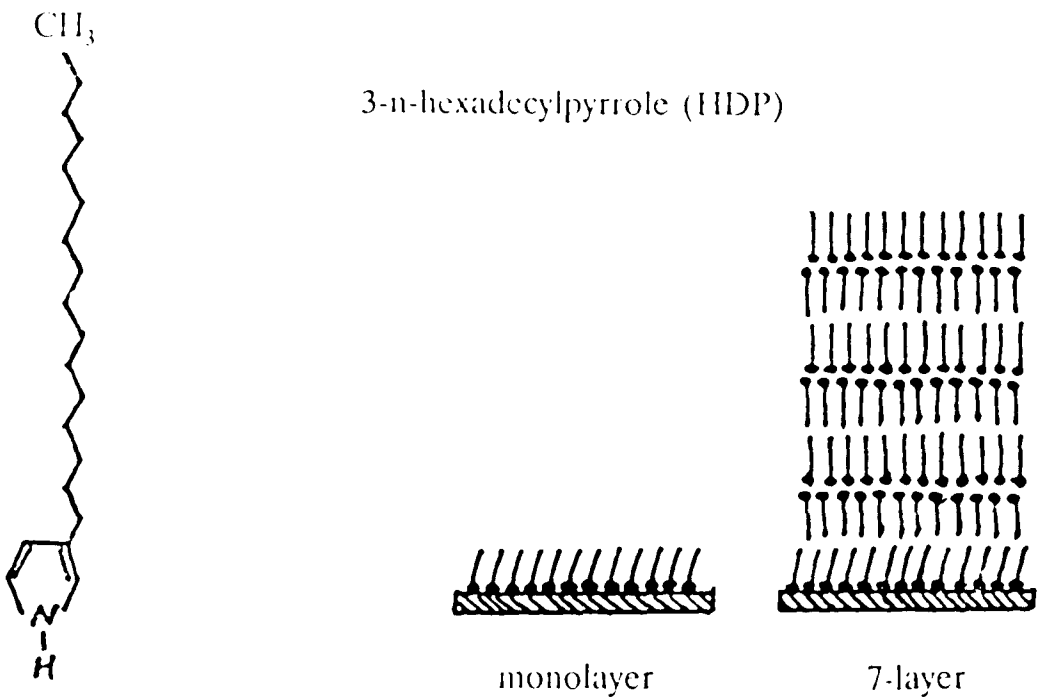


Figure 23. An illustration of LB films of a monolayer and a 7-layer HDP monomer films on Pt-coated glass substrates. In the first layer, the hydrocarbon tails are tilted from the surface normal, while the hydrocarbon tails on second layer and above are nearly normal to the substrate.

**Table I.** Energies and proposed assignment of features in the carbon *K*-edge spectrum of HDP and ODP LB Films.

| No. | HDP monolayer | | | HDP multilayer<br>ODP monolayer | | | Assignment (final orbital) | |
|---|---|---|---|---|---|---|---|---|
| | E (eV) | Intensity 90° | 20° | E (eV) | Intensity 90° | 20° | Ring | Hydrocarbon chain |
| 1 | | | | 285.5 | sh | sh | $\pi^*3b_1(C=C)$ | |
| 1' | 287.5[a] | | | | | | $\pi^*3b_1(C=C)$ | |
| 2 | 288.8 | s | m | 288.5 | s | m | $[\pi^*2a_2(C=C)]$ | $\pi^*(CH_2)$ |
| 3 | 294 | s | s | 294 | m | s | $\sigma^*(C\text{-}C)$ | $\sigma^*(C\text{-}C)$ |
| 4 | 298.5 | w | w | 298.5 | w | w | $\sigma^*(C\text{-}C)$ | $\sigma^*(C\text{-}C)$ |
| 5 | 303 | wm | m | 303 | wm | m | $\sigma^*(C=C)$ | |

s, strong; m, medium; wm, weak medium; w, weak; sh, shoulder.
[a] Energy upshifted from 285.5 eV owing to charge transfer interaction.

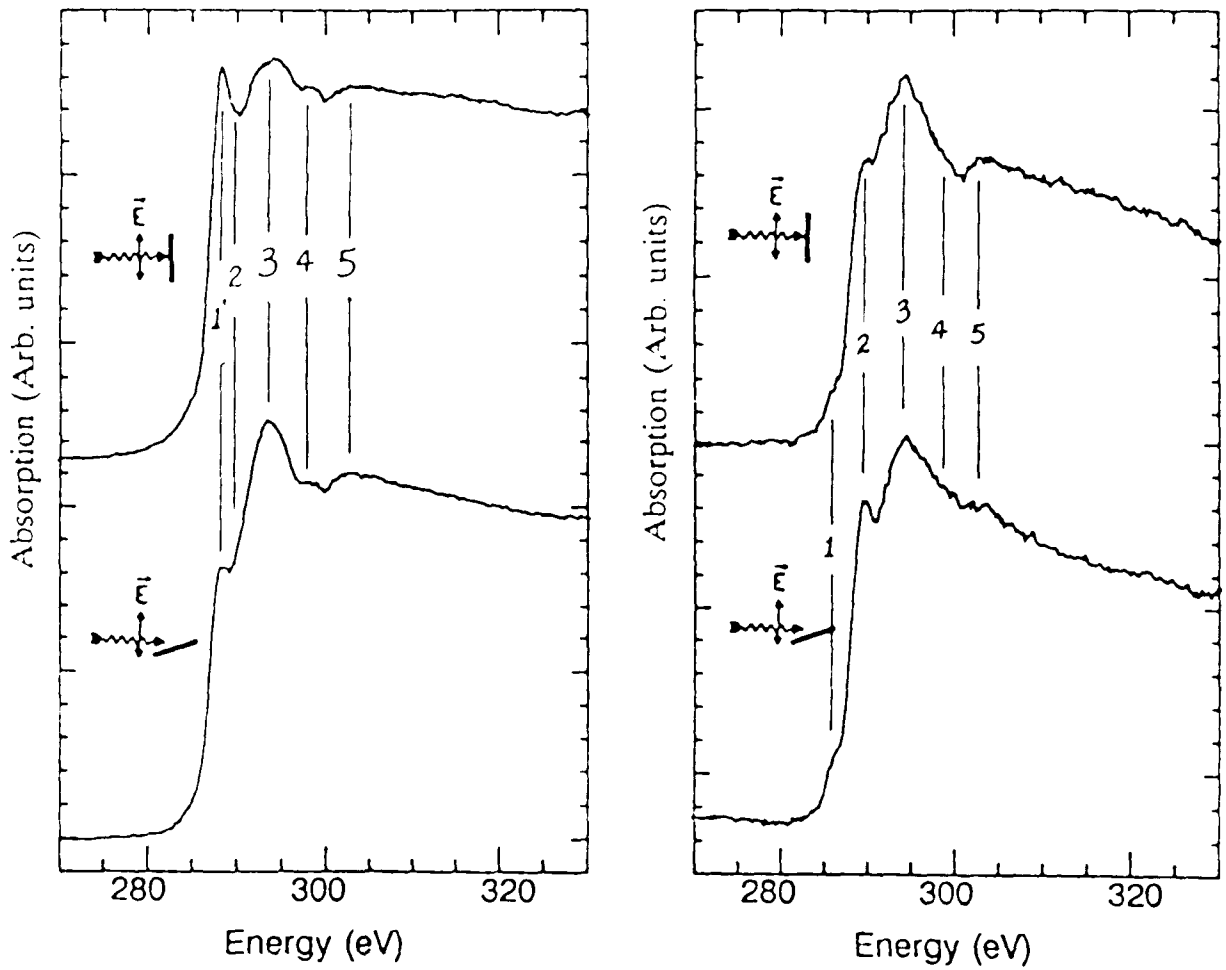


Figure 24. The NEXAFS spectra of (a) octadecylpyrrole (ODP) monolayer on Pt substrate, and (b) a monolayer of pyrrole/octadecylpyrrole copolymer on Pt substrate.

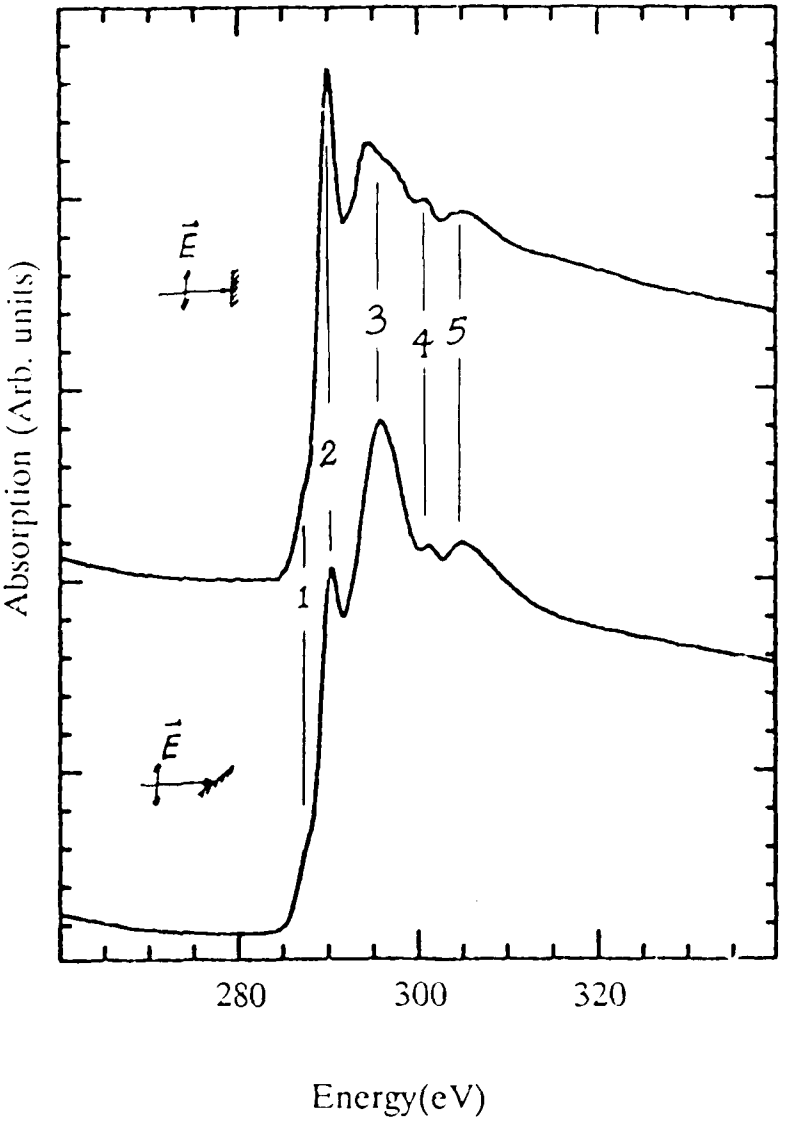


Figure 25. The carbon *K*-edge NEXAFS spectra of a 4-layer LB film of a mixture of ferrocene-derivatized alkylpyrrole and 3-hexadecylpyrrole (HDP) in a 1:5 ratio on a Pt substrate.

In the spectra of the LB film consisting of a mixture of poly(3-butylthiophene) and stearic acid (figure 26b), the polarization dependence is still clear but somewhat reduced, which can be seen by the increased intensity of the $(C\text{-}H)^*$ peak at grazing incidence. This pattern indicates some kind of disordering effect, possibly due to the random orientation of the shorter alkyl chains (4-carbon units compared to 18-carbon units in figure 26a) in the 3-butylthiophene. For the longer alkyl-chain compounds, such as octadecylthiophene, the alkyl chains might be oriented along the same direction as the hydrocarbon chains of the stearic acid (normal to the substrate surface), resulting in spectra exhibiting a higher degree of ordering. Therefore, the higher degree of ordering for the poly(3-ODT) may also be due to the bending the longer alkyl chains in the direction of the hydrocarbon chains of the stearic acid. The shorter chains are too short to reorient themselves along the stearic acid chains. Our results suggest that the poly(3-alkylthiophenes) are randomly oriented within layers of highly ordered stearic acid molecules. A periodicity of 50 Å for the bilayer spacing is maintained throughout the LB films, as determined by x-ray diffraction.

Figure 27 shows the carbon K-edge and sulfur L-edge spectra of a 10-layer film of a 1:1 mixture of poly(octylthiophene) and stearic acid. The energies and proposed assignment of the features are given in Table III. The carbon spectra show very strong polarization dependence, with the highest intensity of the $(C\text{-}H)^*$ peak occurring when the electric field vector is parallel to the substrate, indicating that the hydrocarbon chains are highly ordered and oriented along the surface normal. The octyl chains do not contribute any appreciable amount of disorder reflected in the spectra, which we interpret to mean that the octyl hydrocarbon chains are intercalated along the stearic acid chains. If the octyl chains were randomly oriented in a disordered fashion, the polarization dependence of the spectra would be dramatically reduced since the number of carbon atoms in the octyl chains

is comparable with that of the stearic acid chains.

The sulfur L-edge spectra in figure 27, however, exhibit no polarization dependence. Since the NEXAFS spectrum represents interactions between the absorbing atom and the nearest-neighbor atoms, the sulfur L-edge spectrum exclusively samples the thiophene ring, with no contribution from the alkyl chains. The absence of a polarization dependence of the sulfur spectrum means that the thiophene moieties are randomly oriented, i.e. there is no preferred orientation of the thiophene rings, which is reasonable for a soluble polymer. The carbon and the sulfur spectra, therefore, give independent information about the orientation of the alkyl chains and the polythiophene backbone.

### 5.2.2. Interaction between LB Films and Metallic Substrates

The geometry of an organic compound on metallic substrates is affected by the interaction between the organic compound and the metal surface. This interface was studied by various surface-science techniques (reviewed in chapter 2). In our experiment, the interaction between LB films and Pt substrates was also observed in the carbon *K*-edge NEXAFS spectra of hexadecylpyrrole LB films.

The energies and proposed assignments of features of the alkyl-substituted pyrrole monomer and copolymer LB films are listed in Table I. Figure 22 shows the NEXAFS spectra for the carbon K-edge of (a) a monolayer and (b) multilayer hexadecylpyrrole LB film. In both spectra, the $(C\text{-}H)^*$ peak has the largest intensity at normal incidence, where the **E** vector is parallel to the substrate, so the hydrocarbon chains must be nearly perpendicular to the substrate. However, the monolayer spectra in figure 22a show a reduced polarization dependence, which could be attributed to either a disordering or tilting of the hydrocarbon chains. It is more likely due to tilting caused by the interaction between

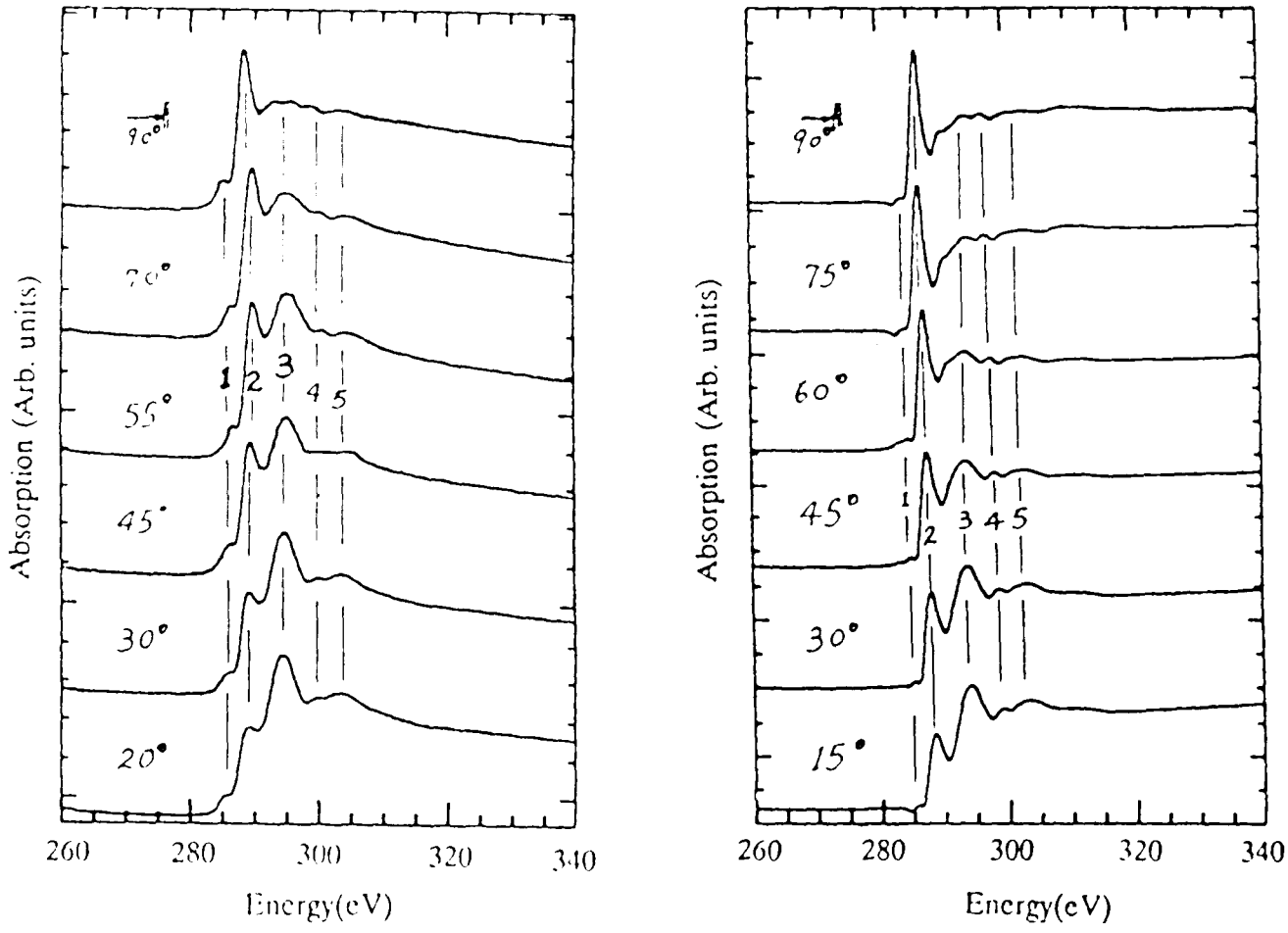


Figure 26. The carbon K-edge NEXAFS spectra of LB films. (a) mixture of poly(3-octadecylthiophene) and stearic acid; and (b) mixture of poly(3-butylthiophene) and stearic acid.

**Table II**. Energies and proposed assignment of features in the carbon *K*-edge NEXAFS spectrum of polythiophene/stearic acid LB film.

| | | Intensity | | Assignment (final orbital) | |
|---|---|---|---|---|---|
| No. | E(eV) | 90° | 20° | Ring | Hydrocarbon chain |
| 1 | 285.5 | sh | sh | $\pi^* 3b_1(C=C)$ | |
| 2 | 288.5 | s | m | $[\pi^* 2a_2(C=C)]$ | $\pi^*$ ($CH_2$) |
| 3 | 294 | s | s | $\sigma^*$ (C-C) | $\sigma^*$ (C-C) |
| 4 | 298.5 | w | w | $\sigma^*$ (C-C) | $\sigma^*$ (C-C) |
| 5 | 303 | w | w | $\sigma^*$ (C=C) | |

s, strong; m, medium; wm, weak medium; w, weak; sh, shoulder.

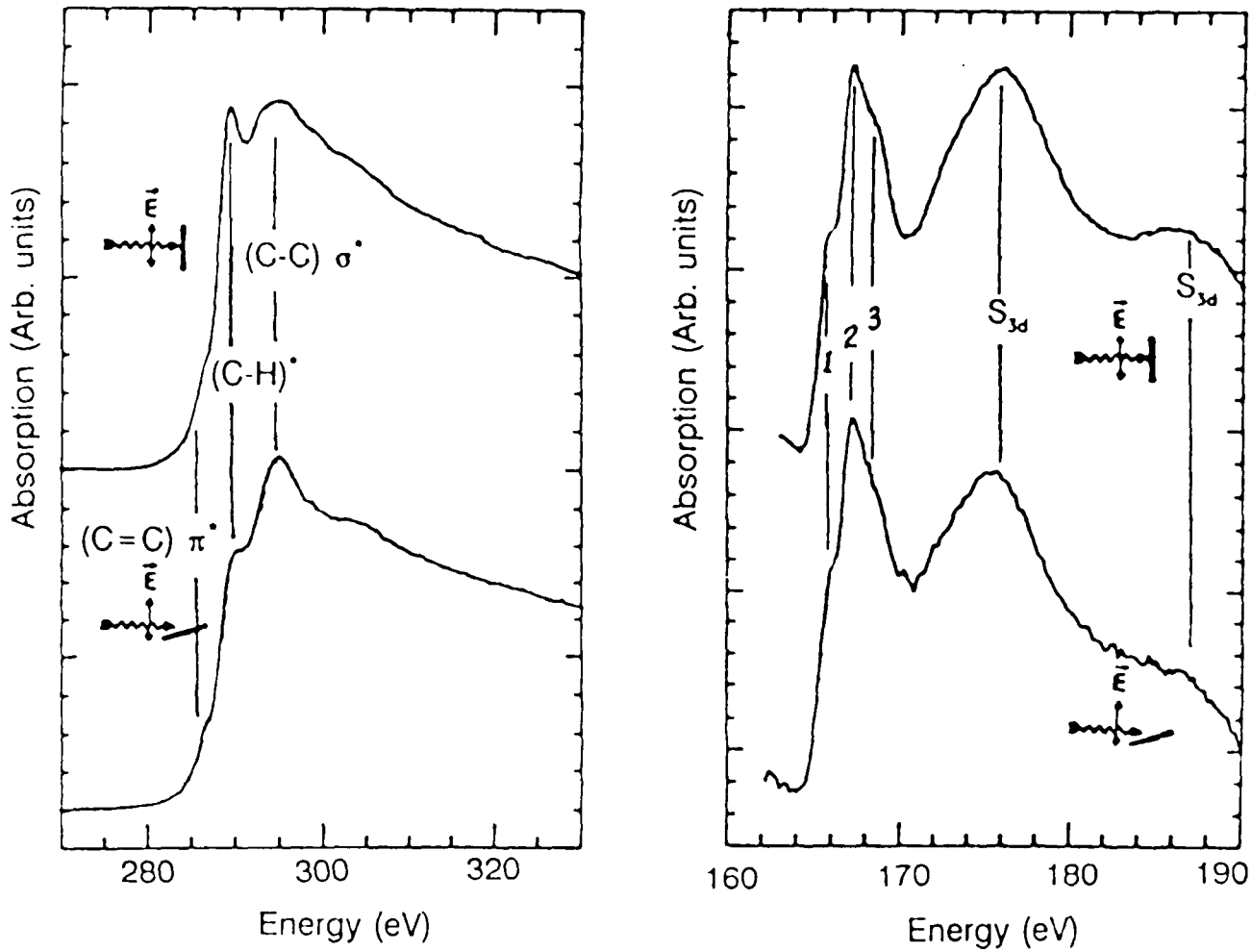


Figure 27. (a) The carbon *K*-edge, and (b) sulfur *L*-edge of a ten-layer LB film of poly(3-octylthiophene) (P3OT) mixed with stearic acid.

**Table III**. Energies and assignment of features in the S 2p spectrum of poly(3-octylthiophene)/stearic acid LB films.

| | PTSA 10 layers | Assignment | |
|---|---|---|---|
| No. | E(eV) | $2p_{3/2}$ | $2p_{1/2}$ |
| 1 | 165.5 | $\pi^* 8b_2$ (C=S) | |
| 2 | 167 | $\pi^* 2a_2$ | $\pi^* 8b_2$ (C-S) |
| 3 | 168.4 | $\sigma^* 12a_1$ | $\pi^* 2a_2$ |
| 4 | 175.5 | S 3d | |
| 5 | 187 | S 3d | |

the pyrrole head group and the Pt substrate, which would make the pyrrole ring orient nearly parallel to the substrate. From the second layer up, the chains orient normal to the substrate, since the pyrrole ring is no longer in contact with the substrate.

It also should be noted that the C=C $\sigma^*$ resonance peak (285.5 eV) (feature 1 in figure 22b) is not present in figure 22a for the monolayer film. Since there is no C=C bond in the alkyl chain, this feature is related solely to the pyrrole head group. When heterocycles are in intimate contact with a metal surface, there is a charge transfer to the metal, resulting in strong bonding or decomposition.[58,110] This charge-transfer interaction results in an energy upshift of the C=C $\pi^*$ feature (labeled 1' in Figure 22a), which cannot be resolved from the strong peak of $(C\text{-}H)^*$, and makes the center of the combined C=C $\pi^*$ and $(C\text{-}H)^*$ peak shift down.

Figure 24 shows the carbon K-edge NEXAFS spectra of (a) octadecylpyrrole monomer and (b) a copolymer of pyrrole and ODP monolayer LB films on Pt. The similarity of Figure 24a and Figure 22a indicates that the ODP monomer monolayer LB film is ordered but tilted from the surface normal, similar to the orientation of the HDP monomer layer LB film. However, the polarization dependence of the spectra for the copolymer LB films is severely reduced, suggesting that disorder was introduced during polymerization. The oxidized film contains anions, which are derived from the $FeCl_3$ in solution. Since the anions are water soluble, their most likely position would be underneath the compact alkylpyrrole film at the air-water interface. Subsequent to transfer, their most likely position would be between the pyrrole head groups and the metal substrate, which could cause the pyrrole moieties to separate from the metal substrate, preventing the charge-transfer interaction that occurs with intimate contact. Consequently, the transition to the unaltered C=C $\pi^*$ orbital (feature 1 in Figure 22b) is observed.

5.2.3. Superlattice Structure of LB Films Studied with X-ray Diffraction

Once a multilayer LB film is deposited on a solid substrate, the thickness of the multilayer film and its layer structure, as well as its in-plane structure, are the basic issues to be resolved. X-ray diffraction can easily provide evidence of the multilayer structure. The in-plane layer structure of LB films made of poly-hexadecylthiophene mixed with stearic acid also has been studied by grazing angle x-ray diffraction at different temperatures. For such studies, a high-intensity x-ray beam, such as a synchrotron radiation source, is necessary to obtain a good signal-to-noise ratio. To improve angular resolution, a crystal analyzer was placed in front of the detector, providing the opportunity to study small structural changes with temperature.

The x-ray diffraction studies were carried out on beam line X18A and X7B of the National Synchrotron Light Source, using a conventional four-circle Huber diffractometer with a two circle analyzer on the $2\theta$ arm. The incident beam was monochromated by a Si(200) double-crystal monochromator with the wavelength set at $\lambda = 0.94$ Å. The layer structure along the stacking direction was studied by taking $\theta$ and $2\theta$ scans simultaneously. The scattering geometry is sketched in Figure 28. A Ge crystal analyzer with the (220) Bragg reflection was used in front of a Na(I) scintillation detector to improve the angular resolution. The in-plane structure was studied by grazing angle diffraction with a fixed incidence angle at a nearly critical angle where the diffraction beam goes virtually along the layer. The in-plane diffracted beams were recorded by scanning the detector in the horizontal plane. A 0.1° Söller slit was used to improve angular resolution. The temperature was monitored by a platinum resistance thermometer attached to the sample.

A superlattice structure of 34 layers of LB film made of stearic acid with $Cd^{++}$ was observed in the x-ray diffraction pattern at 25°C and at 110°C. The diffraction patterns are

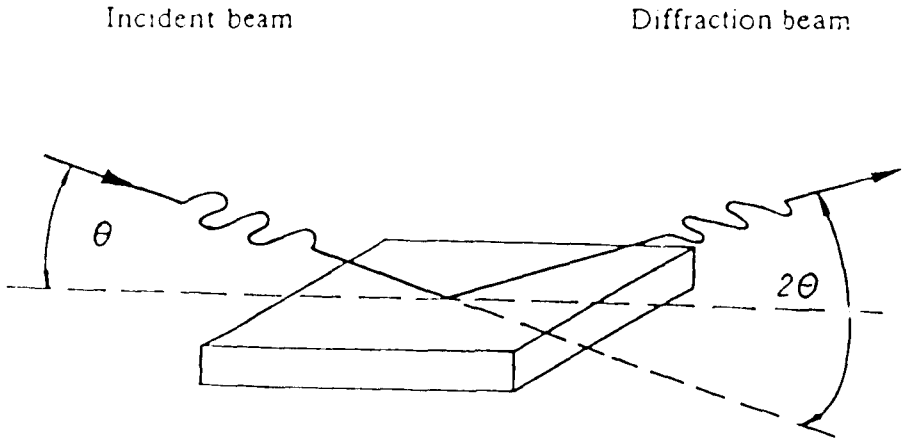


Schematic diagram for out-of-plane x-ray diffraction

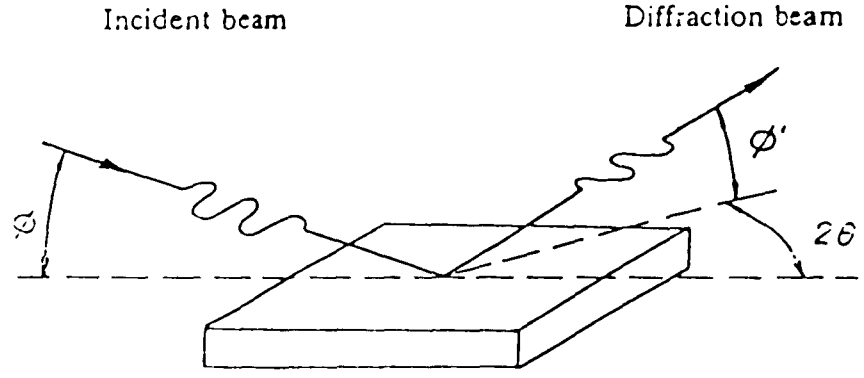


Schematic diagram for in-plane x-ray diffraction

Figure 28. Schematic diagram for (a) out-of-plane, and (b) in-plane x-ray diffraction. The out-of-plane measurements were taken by taking the $\theta$ and $2\theta$ scans simultaneously, and the in-plane measurements were taken by taking the $2\theta$ scan while the incident x-ray beam was set at nearly critical angle.

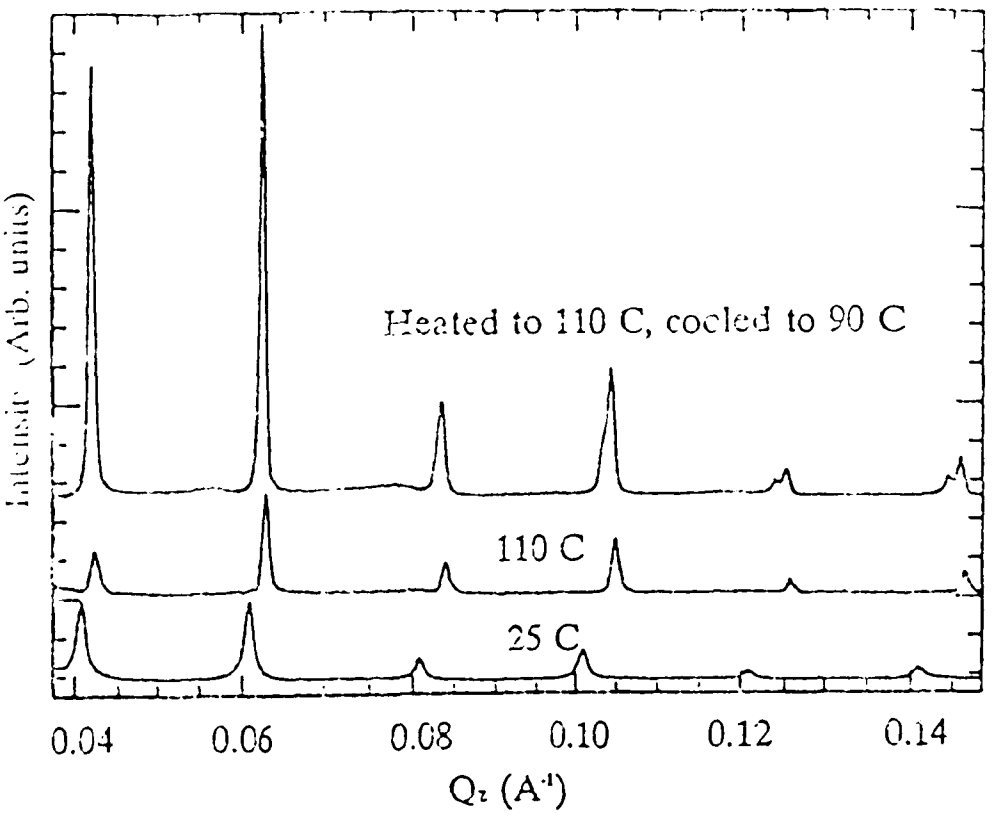


| | d | d' |
|---|---|---|
| 25°C | 49 Å | 49 Å |
| 110°C | 48.4 Å | 48.4 Å |
| Cooled to 90°C | 48.6 Å | 47.9 Å |

$d_T$ = 50.3 Å

Figure 29. X-ray diffraction patterns of a 34-layer LB film made of stearic acid with $Cd^{++}$ at different temperatures, in the sequence of 25°C, 110°C, and 90°C. The diffraction patterns are plotted as intensity in arbitrary units versus $Q_z(1/Å)$, while d=49 Å is the thickness of a single bilayer at 25°C, and $d_t$=50.3 Å is the theoretically calculated d-spacing value.

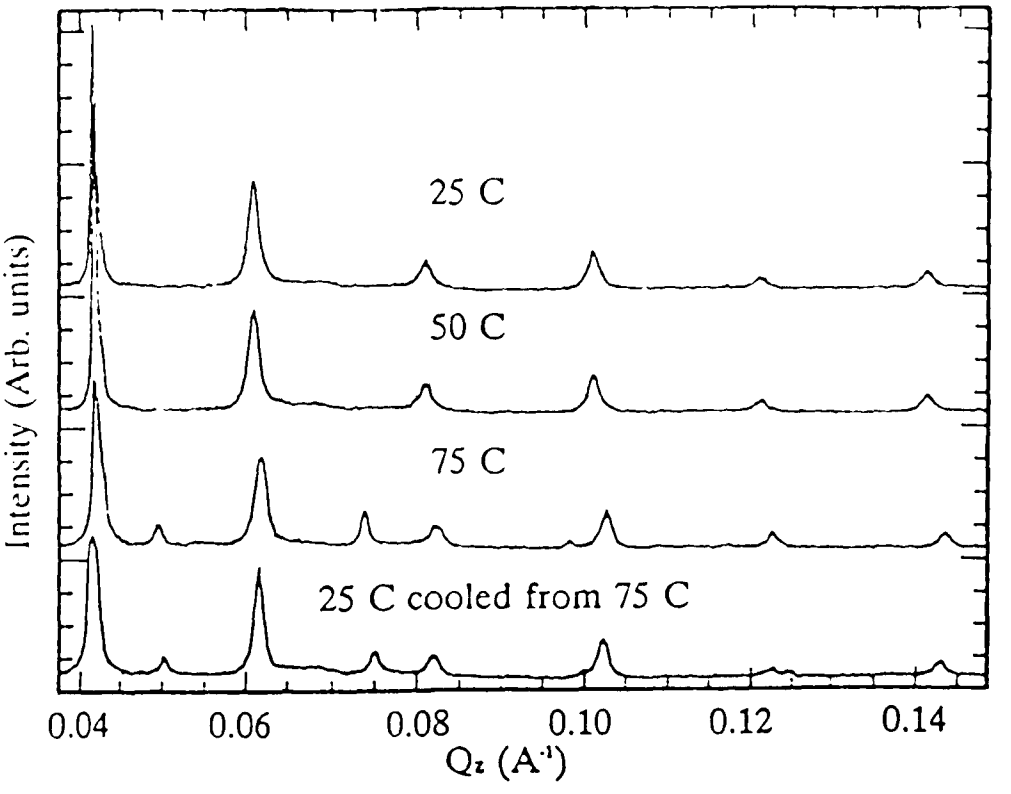


| | d | d' |
|---|---|---|
| 25°C | 49 Å | |
| 50°C | 48.95 Å | |
| 75°C | 48.8 Å | 40 Å |
| 25°C (cooled) | 48.95 Å | 39.9 Å |

Figure 30. The X-ray diffraction patterns of a 34-layer LB film made of a mixture of poly(3-hexylthiophene) and stearic acid in 1:2 ratio with $Cd^{++}$ at different temperatures, in the sequence of 25°C, 50°C, 75°C, and 25°C. The diffraction patterns are plotted as intensity in arbitrary units versus $Q_z(1/Å)$, while d = 49 Å is the thickness of a single bilayer at 25°C.

plotted as the intensity versus $Q_z(1/Å)$, which is defined as $Q_z = 2\sin\theta/\lambda$ (Figure 29). The 2nd, 3rd, 4th, 5th, 6th, and 7th order (001) type Bragg reflections peaks are shown in the figure. Evidently, the diffraction pattern consists alternately of intense peaks for odd orders of diffraction and weak peaks for even orders. This pattern indicates a superlattice structure in the material. The d-spacing of the layer corresponds to $49 \pm 0.05$ Å determined from the x-ray diffraction pattern. This value is only slightly smaller than the theoretically calculated value $d_T = 50.3$ Å by M. Sugi,[111] which is based on the assumption that there is no correlation between the layers. The hydrocarbon chains of stearic acid, therefore, are nearly normal to the sample substrate.

Similarly, a superlattice structure is observed in the x-ray diffraction pattern of a LB film made of conducting polymeric materials: poly(3-hexylthiophene) mixed with stearic acid in a 1:2 ratio (Figure 30). Both the diffraction pattern and the d-spacing of the LB layer are almost identical to that of the LB film made of pure stearic acid, which indicates that these two samples have a very similar structure in the direction of layer stacking at room temperature.

### 5.2.4. Temperature Dependence of the Structure of LB Films

To have a better understanding of the structure of multilayer films in 3-dimensions as well as their temperature-dependence, a 34-layer stearic acid LB film was studied at different temperatures using in-plane and out-of-plane x-ray diffraction. The structure of the LB film, which was made of a 34-layer mixture of poly(3-hexylthiophene) and stearic acid in a 1:2 ratio, was also studied by out-of-plane x-ray diffraction.

Figure 29 shows x-ray diffraction patterns of a 34 layer LB film made of stearic acid with $Cd^{++}$ at different temperatures in the sequence of 25°C, 110°C, and 90°C, plotted

as intensity versus $Q_z(1/Å)$. When the temperature of the sample was increased to 110°C, there was a clear peak position shift to a d spacing of 48.4 Å in the diffraction pattern. This reduction in d-spacing indicates that the hydrocarbon tails are tilted or disordered at elevated temperatures. By comparing with FTIR spectroscopic studies of similar LB multilayer films,[112] we conclude that this reduction is probably caused by tilted hydrocarbon tails.

Figure 29 shows that when the temperature is lowered down to 90°C from 110°C, there is a peak splitting in the x-ray diffraction pattern. The d-spacings of these two sets of peaks correspond to d'=47.9 Å and d=48.6 Å. This phenomenon indicates a phase separation due to a recrystallization of the sample at elevated temperatures. Buhaenso *et al.*[113] observed similar thermal behavior of another LB film, made of 40-layer docosanoic acid with $2.5\times10^{-4}$ M $CdCl_2$ concentration in the water subphase. The intensity of the x-ray diffraction pattern greatly increased at 90°C, indicating that the ordering of the layer structure of the LB film increased with as the temperature fell. We believe that this phase separation is due to the redistribution of the $Cd^{++}$ ions between the layers at elevated temperature, but it is still not well understood how the distribution of $Cd^{++}$ ions changes. However, it is important to note that the reproducibility of a LB film is still poor because of the accuracy of the $Cd^{++}$ ion concentration, and the pH of the water. These features will change the distribution of the $Cd^{++}$ in the LB film, resulting in a different thermal behavior of the films.

The in-plane x-ray diffraction pattern of a 34-layer stearic acid LB film also was studied. Figure 30 shows the in-plane x-ray diffraction patterns at different temperatures in the sequence of 25°C, 110°C, and 90°C, plotted as the intensity versus $Q_{xy}$ (1/Å). At 25°C, there is one broad peak. The d-spacing in the in-plane structure is calculated from

the diffraction pattern as 4.13 Å. Based on the electron diffraction studies from monolayers of fatty acids by Garoff *et al*[114] and Bonnerot *et al*,[49] the first layer of material deposited has a hexagonal symmetry, and there is little correlation between the layers.[54] Therefore, it is not unreasonable to assume that the stearic acid LB film also forms a hexagonal structure within a layer at 25°C.

At 110°C, two peaks were observed in the in-plane diffraction pattern, whose d-spacing corresponds to 4.26 Å and 3.83 Å. These d-spacing values are very close to the $d_{110}$=4.15 Å and $d_{020}$=3.71 Å values as observed by M. Bloch *et al.* for the orthorhombic structure in a multilayer film at room temperature. Evidently, the peak split indicates a phase transition in the in-plane structure, which corresponds to the phase transition observed in the out-of-plane x-ray diffraction in the same temperature range from 90 to 110°C. Therefore, the structure of the stearic acid LB film changes from a hexagonal possibly to an orthorhombic with increasing temperature. When the temperature is reduced to 90°C, the in-plane diffraction pattern remains unchanged (see Figure 31) except that its signal-to-noise ratio is reduced. In comparison with the out-of-plane diffraction pattern in Figure 29, the peak intensity is much higher at 90°C than at 110°C, implying that during recrystallization, the degree of ordering is increased between the layers (in the stacking direction) and decreased within a layer (in the plane). This change may still be the consequence of the redistribution of $Cd^{++}$ between the layers.

The temperature dependence of a undoped LB film was also studied with x-ray diffraction (Figure 30). The multilayer film consisted of 34-layers of the mixture of poly(3-hexylthiophene) and stearic acid in a 1:2 ratio. At 25°C, both the diffraction pattern and the d-spacing are the same as that of the stearic acid LB film (Figure 29), indicating that the stacking direction of the layer structure of the PHT/stearic acid LB film is similar to

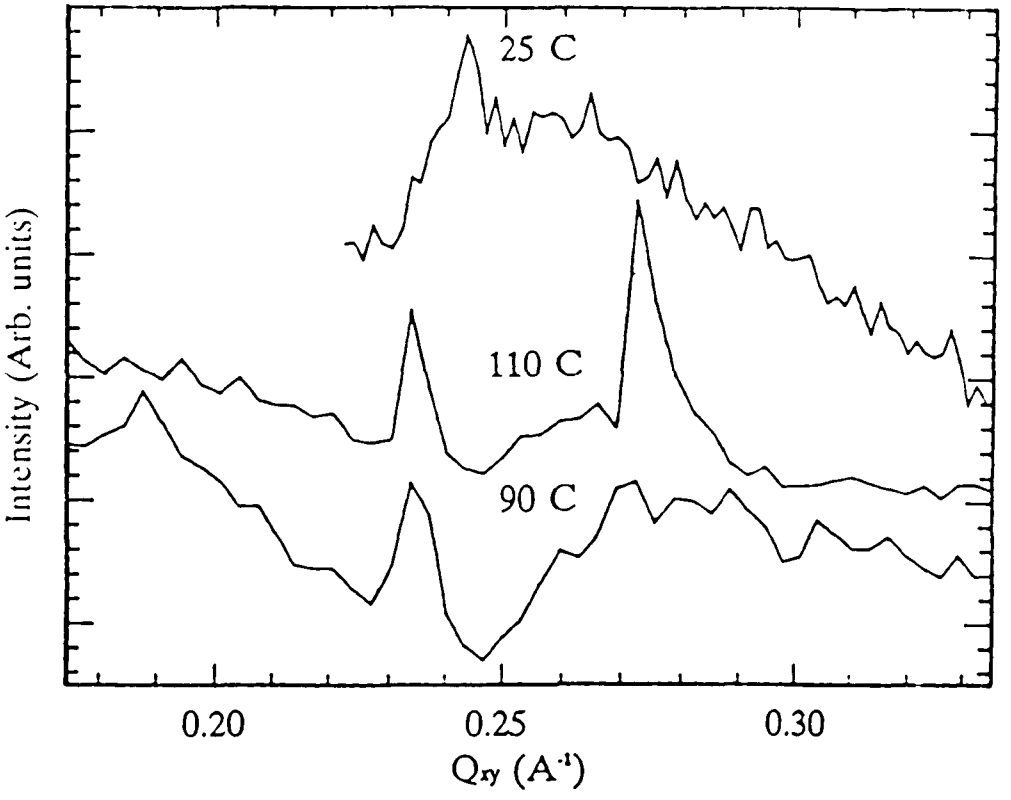


| | $d_{11}$ | $d_{02}$ |
|---|---|---|
| 25°C | 4.13 Å | 4.13 Å |
| 110°C | 4.26 Å | 3.83 Å |
| Cooled to 90°C | 4.26 Å | 3.83 Å |

Figure 31. The in-plane x-ray diffraction patterns of a 34-layer LB film made of stearic acid with $Cd^{++}$ at different temperatures, in the sequence of 25°C, 110°C, and 90°C. Intensity is plotted in arbitrary units versus $Q_{xy}$ (1/Å).

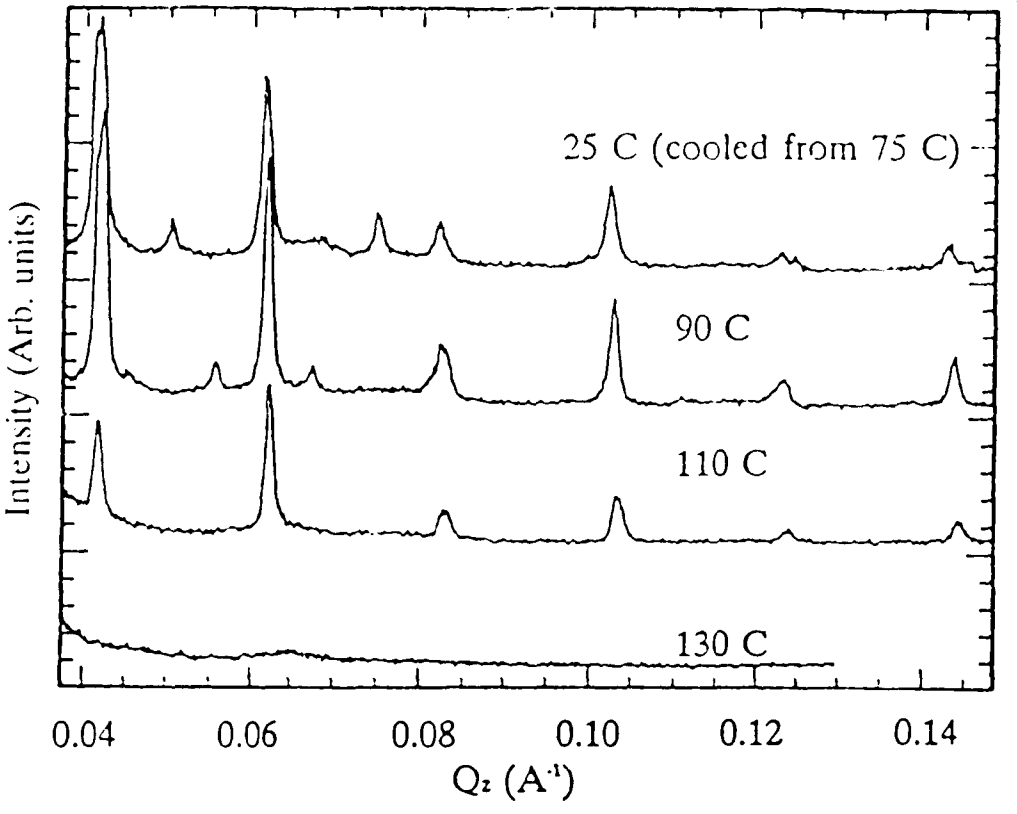


| | d | d' |
|---|---|---|
| 25°C (cooled) | 48.5 Å | 39.9 Å |
| 90°C | 48.3 Å | 37 Å |
| 110°C | 48.3 Å | peak disappeared |
| 130°C | no peaks | no peaks |

Figure 32. The X-ray diffraction patterns of a 34-layer LB film made of the mixture of poly(3-hexylthiophene) and stearic acid in 1:2 ratio with $Cd^{++}$ at different temperatures, in the sequence 25°C, 90°C, 110°C, and 130°C. The diffraction patterns are plotted as intensity in arbitrary units versus $Q_z(1/Å)$, where d = 49 Å is the thickness of a single bilayer at 25°C.

that of the stearic acid LB film at room temperature. At 50°C, the diffraction peaks shift towards a higher angle, corresponding to d=48.95 Å, indicating that the d-spacing of the LB film decreases with increasing temperature. At 75°C, a new set of peaks appears, corresponding to d'=40 Å, while the original set of peaks shifts slightly towards larger angle, corresponding to d=48.8 Å. When the temperature of the sample was reduced to 25°C, the d-spacing of the new set of peaks decreased continuously to d'=39.9 Å, while the d-spacing of the original set of peaks increased to d=48.95 Å.

When the temperature of the same sample is increased to 90°C(figure 32), the d-spacing of the new set of peaks continued to decrease to d'=37 Å, while the d-spacing of the original set of peaks decreased slightly to d=48.3 Å. At 110°C, the new set of peaks disappeared, while the positions of the original set of peaks remained basically the same. Finally, all diffraction peaks disappeared at 130°C, indicating that the film had melted.

It is clear that the original set of peaks and the new set have completely different thermal behaviors. The original set behaves like that of the stearic acid LB film. In contrast, the d-spacing of the new set of peaks decreased much faster than that of the original set during heating, and continued to during cooling. Furthermore, the new set of peaks disappeared at a temperature below the melting temperature of the film, implying that these two sets of peaks represent two different phases of the LB film.

For mixed polymer and monomer LB films, such as P3HT mixed with stearic acid, the polymers and the monomers normally are not homogeneously mixed, nor are the $Cd^{++}$ ions uniformly distributed between the layers. In some regions, that we call type A, stearic acid acts as a matrix into which the longer hydrocarbonic tails of P3HT can intercalate, with the $Cd^{++}$ ions located between layers. This structure was observed in our NEXAFS study. This part of the film consists of a combination of crystalline and amorphous phases. In other

regions, type B, where stearic acid with $Cd^{++}$ dominates, the film is in a crystalline phase that is determined by the stearic acid. When the temperature increases to 75°C, the thermal behavior of the film in a crystalline phase is very similar to that of a pure stearic acid LB film. The hydrocarbon tails become tilted with increasing temperature. The phase separation of the LB film observed in x-ray diffraction patterns at 75°C is mostly due to the redistribution of $Cd^{++}$ ions between the layers in both type A and B regions, and partially due to the rearrangement of P3HT in the stearic acid matrix in type A regions. The rearrangement of P3HT in the stearic acid matrix may cause a dramatic reduction in d-spacing between the layers in type A regions, which generates a new set of peaks the in x-ray diffraction pattern. When the temperature of the sample was reduced to 25°C, the orientation of the hydrocarbon tails of the stearic acid and the redistribution of $Cd^{++}$ are reversible in type B regions, but the conformation of P3HT and stearic acid is irreversible in type A regions due to the existence of the polymer P3HT. On the other hand, the thermal contraction of P3HT during cooling causes the d-spacing of the layers in type A to further decrease. However, when the temperature was increased to 110°C, the film in type A regions turned into a completely amorphous phase, while the film in type B regions remained in crystalline phase. Therefore, one set of peaks disappeared completely in the x-ray diffraction pattern at 110°C below the melting temperature of the film (Figure 32).

## 5.3. Electron-Conducting Polymeric Materials

The interaction of the electrochemically polymerized films with electrode surfaces and the orientation and structure of the first several layers are of importance to our understanding of how polymer films grow. The electroactive properties depend on the

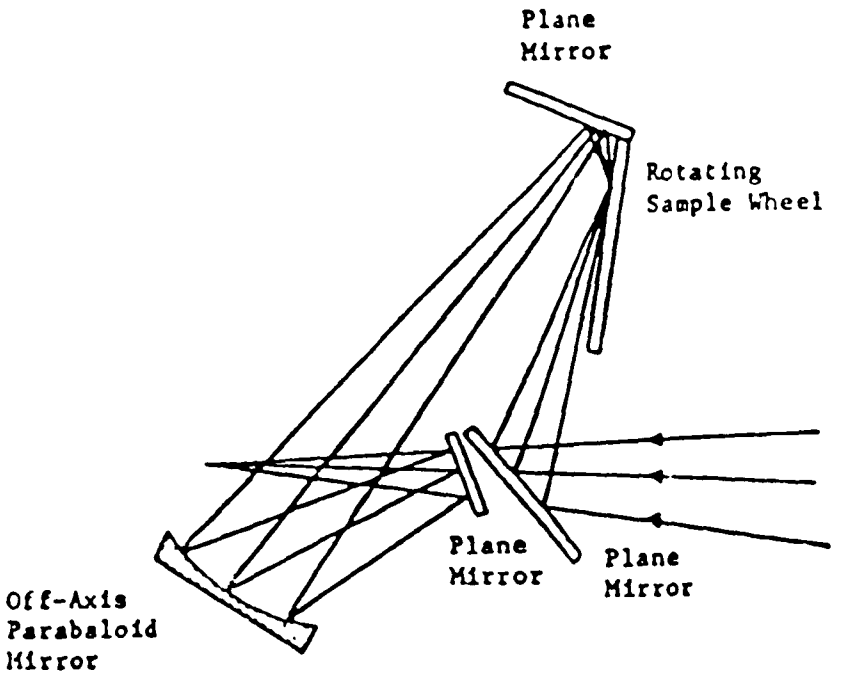


Figure 33. A schematic diagram of the grazing incidence reflection (GIR) attachment in FTIR experiment.

structure of the polymer film. Vibrational (EELS) and thermal desorption spectra (TDS) were used previously to investigate heterocyclic molecules such as pyrrole, furan, and thiophene adsorbed on Cu at 85 - 300 K. Very little work has been done on the interface of polymer films electrochemically deposited on metallic electrodes.

A series of poly(3-methylthiophene) (PMeT) films was studied by FTIR and NEXAFS spectroscopies. Different thicknesses of the PMeT films were electrochemically polymerized on Pt substrates (see chapter 4.2). The high degree of orientation of the thin films was clearly shown in both the FTIR and NEXAFS spectra. Evidently, for polymer films within a few hundred Angstrom, the thiophene rings are predominantly oriented parallel to the surface of Pt substrate. More highly ordered films were produced at lower polymerization potential than at higher potential.

### 5.3.1. FTIR Study of the Orientation and Ordering of Poly(3-methylthiophene) Films

The infrared spectra were taken with a Mattson Cygnus 100 IR spectrometer with a DTGS detector at room temperature. A modified specular reflection accessory was used. A sample wheel could be turned from outside the spectrophotometer to interchange the sample and the reference without breaking the purge. A schematic diagram of the grazing incident-angle reflection attachment is shown in Figure 33. This improvement reduced the problem of $H_2O$ and $CO_2$ bandsdue to the unnormalized background during sample changing. A platinum-coated microscope glass slide was used as reference. The sample chamber was purged continuously with nitrogen during the experiments. An incident angle of 85° was used for all the samples, and 2000 scans were averaged for improved signal to noise ratio.

Figure 34 shows the grazing incidence reflection (GIR) spectra of undoped PMeT

**Table IV.** Band Assignment for undoped poly(3-methylthiophene) in the C-H stretching region in FTIR spectrum from 3200 to 2800 ($cm^{-1}$) wavenumbers.

| Frequency ($cm^{-1}$) | mode | Polarization relative to the plane of the molecular ring |
|---|---|---|
| 3056 | $\nu$ (CH) at $\beta$ position | parallel |
| 2962 | $\nu_a(CH_3)$ in skeletal plane | parallel |
| 2950 | $\nu_a(CH_3)$ out of skeletal plane | perpendicular |
| 2920 | $\nu_a(CH_2)$ | both |
| 2865 | $\nu_s(CH_2)$ | both |

$\nu$ Stretch (a, asymmetric; s, symmetric)

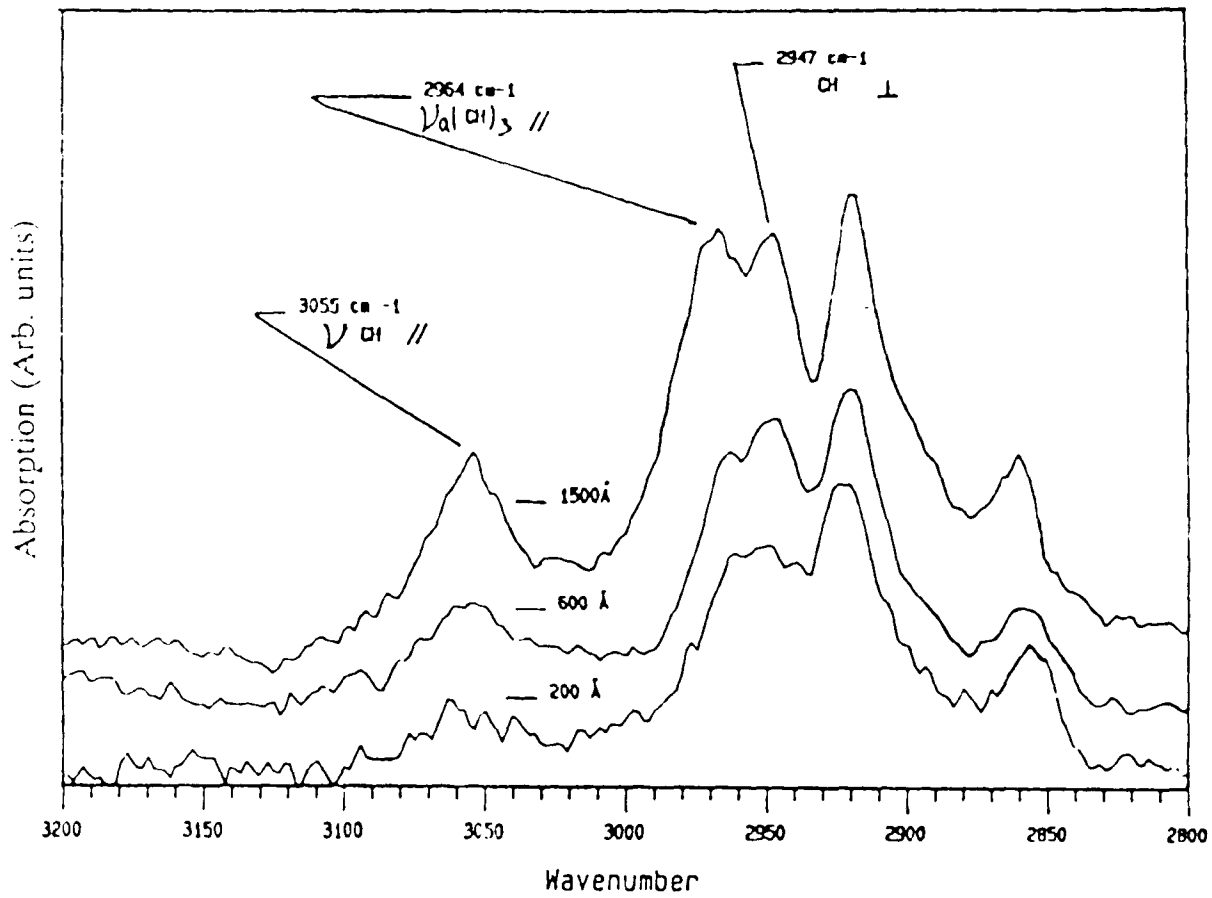


Figure 34. The grazing incidence reflection FTIR spectra of reduced poly(3-methylthiophene) polymerized at 1.8 V vs SCE in the C-H stretching region. The thicknesses of the samples are 1500 Å, 600 Å, and 200 Å.

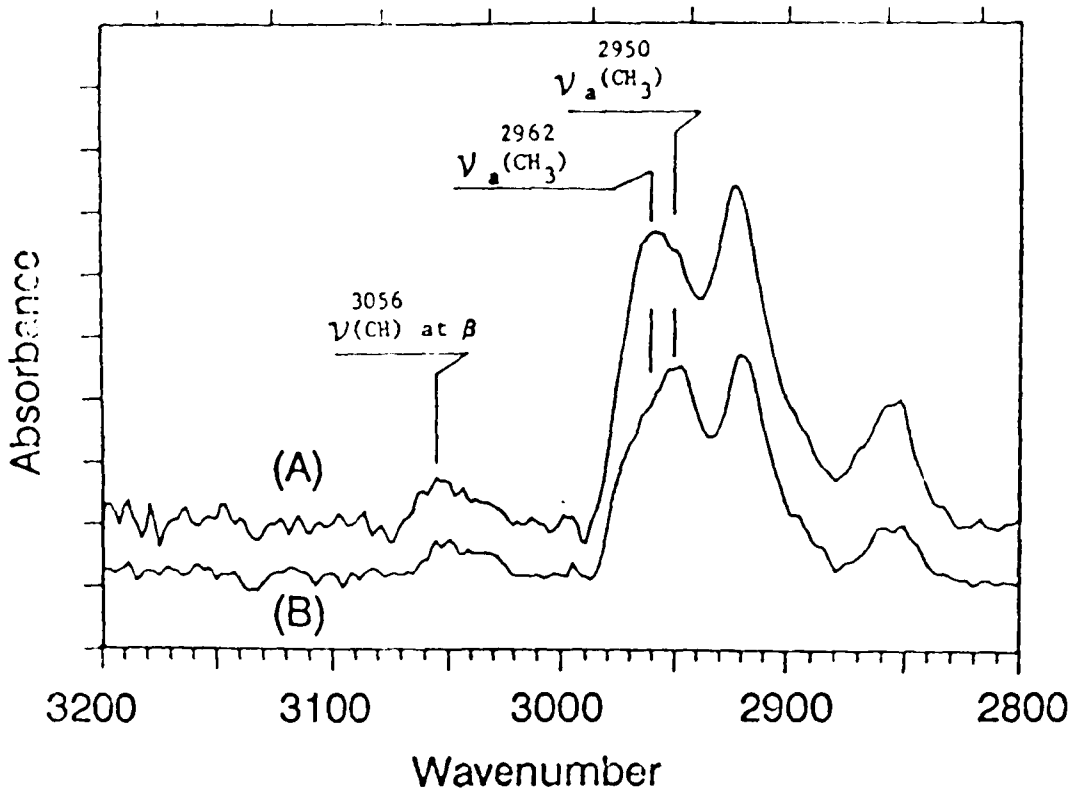


Figure 35. Grazing incident reflection FTIR spectra of reduced poly(3-methylthiophene) in the C-H stretching region. The two 250 Å thick films were polymerized (a) at 1.8 V vs SCE, and (b) at 1.4 V vs SCE.

films with various thicknesses in the C-H stretching region where the vibrational modes are well characterized.[115] The band assignments for the PMeT thin film in the C-H stretching region are listed in Table IV. The relative intensities of the peak at $\nu$ = 3055 $cm^{-1}$, due to the C-H stretch mode at the $\beta$ position, and the peak at $\nu$ = 2964 $cm^{-1}$, due to the in-plane $CH_3$ asymmetric stretch mode, decrease with decreasing film thickness. Since the dipole moment of these two modes is parallel to the thiophene ring, this result indicates that, in the thinner film, the thiophene rings are parallel to the Pt substrate.

Figure 35 shows the spectra of undoped PMeT films polymerized at two different potentials 1.8 V/SCE and 1.4 V/SCE. The relative intensities of the 3056 $cm^{-1}$ C-H stretch mode at the $\beta$ position and the 2962 $cm^{-1}$ in-plane $CH_3$ asymmetric stretch mode are weaker in the spectrum of the film polymerized at lower potential. The dipole moment change of these two modes is parallel to the thiophene ring. The suppression of these two modes in the spectra indicates a higher degree of ordering, with the thiophene ring parallel to the Pt substrate for the films polymerized at a lower potential.

### 5.3.2. NEXAFS Study of the Ordering of Poly(3-methylthiophene) Films

The NEXAFS study was carried out on beam line U-14 of the National Synchrotron Light Source. The NEXAFS spectra were obtained by total electron yield detection measuring the sample current and normalized to the current from a gold grid placed in the incident beam. The x-raybeam from a synchrotron radiation source is highly polarized in the horizontal plane. Therefore, one can determine the orientation of a sample by rotating the sample with respect to the incident x-ray beam. The background current has been removed in all the spectra presented here.

The orientation of PMeT observed in the FTIR spectrum is also observed with

**Table V.** Energies and proposed assignment of features in the carbon *K*-edge NEXAFS spectrum of poly(3-methylthiophene) LB Films.

| No. | PMET 1.4 V 30 Å | | | PMET 1.8 V 30 Å | | | Assignment (final orbital) |
|---|---|---|---|---|---|---|---|
| | E (eV) | Intensity 90° | 20° | E (eV) | Intensity 90° | 20° | Ring |
| 1 | 285.5 | sh | sh | 285.5 | sh | sh | $\pi^*3b_1(C=C)$ |
| 2 | 288.5 | m | s | 288.5 | m | s | $[\pi^*2a_2(C=C)]$ |
| 3 | 295 | s | s | 295 | s | s | $\sigma^*(C\text{-}C)$ |
| 4 | 298.5 | w | w | 298.5 | w | w | $\sigma^*(C\text{-}C)$ |
| 5 | 304 | wm | wm | 304 | wm | wm | $\sigma^*(C=C)$ |

s, strong; m, medium; wm, weak medium; w, weak; sh, shoulder.

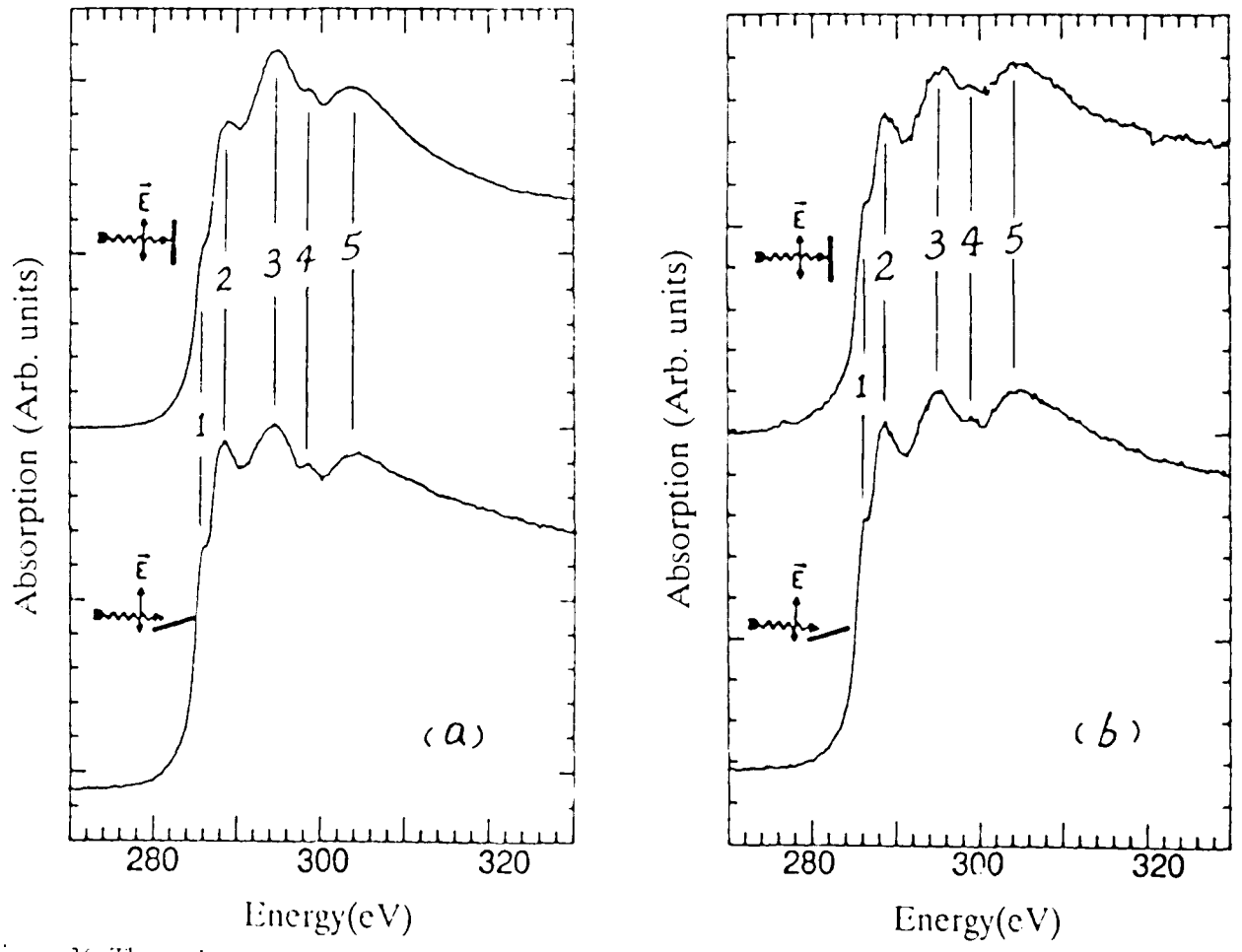


Figure 36. The carbon K-edge NEXAFS spectra of reduced poly(3-methylthiophene) polymerized at 1.8 V vs SCE. The thicknesses of the films are (a) 30 Å, and (b) 1000 Å on Pt. The insets indicate the direction of the incident x-ray beam.

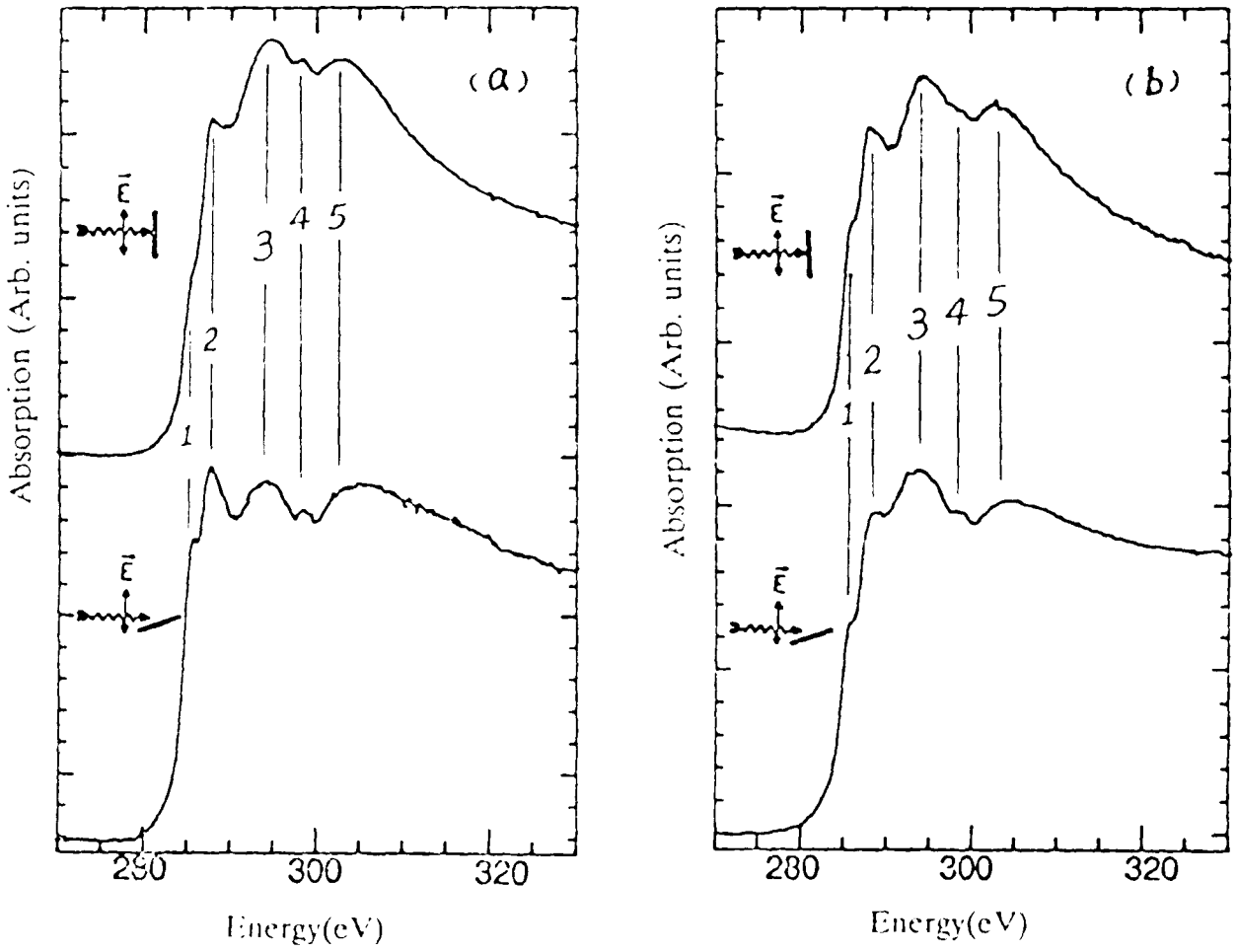


Figure 37. The carbon K-edge NEXAFS spectra of reduced poly(3-methylthiophene) polymerized on a Pt substrate. The two 250 Å thick films were polymerized (a)at 1.4 V vs SCE, and (b)at 1.8 V vs SCE. The insets indicate the direction of the incident x-ray beam

NEXAFS.[116] The NEXAFS spectra of a 30 Å thick PMeT film (Figure 36a) show a clear orientation at 90° and 20° incidence of the x-ray beam polarized in a horizontal plane. The proposed assignments are listed in Table V. As pointed out by Hitchcock *et al*,[117] the resonance peaks corresponding to the $\pi^*$ transition have a maximum intensity when the E vector is parallel to the direction of the $\pi$ orbitals (perpendicular to the C-C axis), while those corresponding to $\sigma^*$ transition will have a maximum intensity when the E vector is parallel to the direction of $\sigma$ orbitals (parallel to the C-C axis). One can determine that the thiophene rings are nearly parallel to the Pt substrate by comparing the $\sigma^*$ and $\pi^*$ transitionpeaks in the near-edge spectra. In contrast, this orientational dependence does not appear in the NEXAFS spectra of a 1000 Å thick PMeT film (Figure 36b), indicating that the thiophene rings are randomly oriented in the thicker film. The NEXAFS spectra of PMeT with the same thickness but polymerized at a different potential are shown in Figure 37. The spectra for the film polymerized at 1.4 V show more angular dependence than those for the film polymerized at 1.8 V, as clearly seen by comparing the peak intensity change with different incident angles of the x-ray beam. This difference suggests that the thin film polymerized at lower potential has a higher degree of ordering, with the thiophene rings predominantly parallel to the substrate. These results confirm the conclusions from the FTIR spectroscopic studies on the same samples.

### 5.3.3. A Comparison of NEXAFS and FTIR Results

NEXAFS spectroscopy is a powerful tool to probe the orientation of an organic compound. For a molecule with low atomic number, NEXAFS can be used to determine the molecular bond angles, based on the selection rule and its angular dependence. Therefore, it has been successfully used to study the orientation of LB films.

Experimentally, the NEXAFS measurement is carried out in a ultra-high vacuum system with a high intensity x-ray beam, which may cause radiation damage to organic material, as was observed in our experiments. In addition, NEXAFS spectroscopy also provides the information about local electron density, which can be used to determine the local geometry of atomic arrangements, such as interatomic spacing and coordination number. Empirically, a relationship between bonding length and photo-emission peak position was also observed, which could be used to determine the bonding length of an unknown compound.

FTIR probes the vibrational modes of asymmetric dipole moments. Based on angular dependence, the technique can also be used to determine the angle of orientation of a molecular bond. However, a molecular bond which has a symmetric dipole moment, is normally IR inactive. The advantage of using IR is that the experiment is carried out at low photon energy and does not require a vacuum.

# Chapter 6. Summary

The microscopic structure, bond length, orientation, and coordination number of conducting polymer films and Langmuir-Blodgett films made of monomers and conducting polymers was studied with several spectroscopic techniques. These techniques include extended x-ray absorption fine structure (EXAFS) spectroscopy, near-edge x-ray absorption fine structure (NEXAFS) spectroscopy, x-ray diffraction, and Fourier-transform infra-red (FTIR) spectroscopy. The techniques are independent and provide complementary information about the structure of disordered polymeric materials and thin films, as well as the orientation behavior of LB films.

The coordination number of oxygens around $K^+$ cations in the ionically conducting polymer mixture of poly(ethylene oxide) (PEO) and potassium iodide (KI) as a function of temperature was studied by EXAFS and NEXAFS spectroscopies. The conductivity of PEO complexes increases with increasing temperature. Both EXAFS and NEXAFS studies show that the primary effect of increasing the temperature, particularly at high salt concentrations, is to reduce the number of oxygen atoms around the $K^+$ ion. This reduced K-O complexation may be responsible for the lower activation energy at higher temperature.

NEXAFS spectroscopy has been shown to be a useful probe of the orientation of LB films by studying transitions from the ground state to $\sigma^*$ and $\pi^*$ anti-bonding states at different x-ray beam incident angles. In 3-alkylpyrrole LB films, the hydrocarbon tails are tilted in the first layer towards the substrate and are nearly normal to the substrate for the following layers. In carbon *K*-edge near-edge spectra of various LB films, a charge transfer interaction was also observed between a polymer thin film and a metallic substrate.

Therefore, orientational behavior may be affected by different metallic substrates due to changes in the valence band. In the LB films madeof the 1:2 mixture of poly(3-alkylthiophene) and stearic acid, the long alkyl chains of the thiophene, such as octadecylthiophene, are intercalated along the hydrocarbon tails of stearic acid, resulting in a highly ordered LB film.

The layer structure and in-plane structure of LB film, which was made of stearic acid with $Cd^{++}$, was studied by x-ray diffraction. Also the layer structure of LB films made of poly(3-alkylthiophene) mixed with stearic acid was studied using x-ray diffraction. A clearly defined superlattice structure was observed in both LB films. The temperature-dependence studies of x-ray diffraction show that (a) a phase separation was observed both in the in-plane structure and in the stacking direction of the LB film made of stearic acid with $Cd^{++}$ at about 110°C, the in-plane structure changing from hexagonal possibly to orthorhombic configuration at elevated temperature; and, (b) there are two separated phases in the LB film made of the mixture of poly(3-hexylthiophene) and stearic acid, one corresponding to the regions where stearic acid and $Cd^{++}$ dominate, and the other corresponding to the regions where stearic acid acts like an ordered matrix into which the hydrocarbon tails of P3HT intercalate.

The orientation behavior and ordering of the electron conducting polymer poly(3-methylthiophene) (PMeT) films were studied by FTIR and NEXAFS. The spectra showed that at the thickness of the polymer films within a few hundred angstroms, the thiophene rings are predominantly oriented parallel to the surface of the Pt substrate. Also, more highly ordered films were produced at lower polymerization potential (1.4V vs SCE) than at higher potential (1.8V vs SCE).

**References**


1. Leo Mandelkern, *An Introduction to Macromolecules*, 2nd Ed. Springer-Verlag, New York, 1982

2. D. E. Fenton, J. M. Parker and P. V. Wright, Polymers, 14, 589 (1973)

3. P. V. Wright, Br. Polymer J., 7, 319 (1975)

4. G. Feuillade and P. Perche, J. Appl. Electrochem., 5, 63 (1975)

5. R. G. Linford and S. Hackwood, Chem. Rev. **81**, 327 (1981).

6. D. O. Raleigh, in *Electroanalytical Chemistry*, edited by A. J. Bard (Dekker, New York) **6**, 88 (1973).

7. M. B. Armand, J. M. Chabagno and M. J. Duclot, in *Fast Ion Transport Solids*, edited by P. Vashishta, J. N. Mundy and G. K. Sherroy (North-Holland, New York, 1979), p. 131.

8. P. R. Sorenson and T. Jaacobsen, Polym. Bull. **9**, 47 (1983).

9. M. Grecki, R. Andreani, C. Berthier, M. B. Armand, M. Mali, J. Roos and D. Brinknann, Solid State Ion. **18**, 295 (1986).

10. M. Gauthier, M. Armand and D. Muller in, *Parotic Polymers Electrolytes and Their Applications*.

11. X. Q. Yang, J. M. Chen, T. A. Skotheim, Y. Okamoto, J. Kirkland and M. L. denBoer, Phys. Rev. B. **40**, 7948 (1989).

12. I. Langmuir, Trans. Faraday Soc., **15**, 62, (1920).

13. K. B. Blodgett, J. Am. Chem. Soc., **57**, 1007 (1935).

14. G. L. Gaines, Thin Solid Films, **99**, ix, (1983).

15. G. L. Gaines, *Insoluble Monolayers at Liquid-Gas Interface* (Inter-science, New York, 1966).

16. R. H. Baughman, J. L. Bredas, R. R. Chance, H. Eckhardt, R. L. Elsenbaumer, D. M. Ivoryl G.C. Miller, A. F. Preiaiosi and L. W. Shacklette, in *Macromolecular Metals and Semiconductors*, Conductive Polymers, (Plenum, New York, 1981), p. 137.

17. C. K. Chiang, S. C. Gau, C. R. Fincher, Y.W. Park, A. G. MacDiarmid and A. J. Heeger, Appl. Phys. Lett., **33**, 18 (1978).

18. Alan J. Heeger, in *Handbook of Conducting Polymers*, T. Skotheim (Ed.), (Dekker, New York, 1986), V. 2, pp. 729-751.

19. S. Pekker and A. Janossy in *Handbook of Conducting Polymers*, T. Skotheim (Ed.) Dekker, 1986, P. 45

20. J. R. Ellis, in *Handbook of Conducting Polymers*, T. Skotheim (Ed.), Dekker, 1986, V.1, p. 489 and p. 501

21. L. W. Shacklette, J. E. Toth, N. S. Murthy and R. H. Baughman, J. Electrochem. Soc., **132**, 1529 (1985).

22. N. Mermilliod, J. Tsanguy and F. Petiot, J. Electrochem. Soc., **133**, 1073 (1986).

23. J. F. Rabolt, F. C. Burns, N. E. Schlotter and J. D. Swalen, J. Chem. Phys., **78**, 946 (1983).

24. X. Q. Yang, J. M. Chen, P. D. Hale, T. Inagaki, T. A. Skotheim, Y. Okamoto, L. Samuelson, S. Tripathy, K. Hong, M. F. Rubner, M. L. denBoer, Synth. Met., **28**, C251 (1989).

25. J. P. Rabe, J. D. Swalen and J. F. Rabolt, J. Chem. Phys., **86**, 1601 (1987).

26. S. Garoof, H. W. Deckman, J. H. Dunsmuir, M. S. Alvarez and J. M. Bloch, J. Phys. (Paris), **47**, 701 (1986).

27. M. Seul, P. Eisenberger and H. M. McConnel, Proc. Natl. Head. Sci. USA, **80**, 5795 (1983).

28. D. A. Outka, J. Stöhr, J. P. Rabe, J. D. Swalen and H. H. Robermund, Phys. Rev. Lett., **59**, 1321 (1987).

29. D. A. Outka, J. Stöhr, J. P. Rave and J. D. Swalen, J. Chem. Phys., **88**, 4076 (1987).

30. E. Sauter, Z. Physik. Chem., B, **21**, 161, 1933.

31. W. H. Barnes, and S. Ross, J. Am. Chem. Soc., **58**, 1129 (1936).

32. W. H. T. Davison, J. Chem. Soc., 3270 (1955).

33. Y. Kuroda, and M. Kubo, J. Polym. Sci. **36**, 453 (1959).

34. P. A. Laurent, and E. Arsenio, Bull. Soc. Chim. France, 618 (1958).

35. A. A. Blumberg, and S. S. Pollack, J. Polym. Sci. A, **2**, 2499 (1961).

36. P. J. Hendra, and D. B. Powell, J. Chem. Soc., 5105 (1960).

37. C. Rossi and V. Magnaco, J. Polym. Sci. **58**, 977 (1962).

38. T. Yoshihara, H. Tadokoro, and S. Murahashi, J. Chem. Phys. **41**, 9, 2902 (1964).

39. J. L. Koenig and F. J. Boerio, J. Chem. Phys., **50**, 2823 (1969).

40. G. Zerbi and P. J. Hendra, J. Mol. Spectra. **27**, 17 (1968).

41. J. L. Koenig and A. C. Angood, J. Polym. Sci. A-2, **8**, 1787-1796 (1970).

42. C. R. A. Catlow, A. V. Chadwick, G. N. Greaves, L. M. Moroney and M. R. Worboys, Solid State Ionics 9&10, 1107-1114 (1983).

43. B. L. Papke, M. A. Ratner, and D. F. Shriver, J. Electrochem. Soc., **129** (7), 1434 (1982).

44. C. Holley and S. Bernstein, Phys. Rev. **49**, 403 (1936).

45. C. Holley and S. Bernstein, Phys. Rev. **52**, 525 (1937).

46. A. Matsuda, M. Sugi, T. Fukui, S. Iizimi, M. Miyahara, and Y. Otsubo, J. Appl. Phys. **48**, 771-774 (1977).

47. E. Havanga, J. de Wael, Rec. Trav. Chim. **56**, 375 (1937).

48. J. H. Germer, and K. H. Storks, J. Chem. Phys. **6**, 280 (1938).

49. A. Bonnerot, P. A. Chollet, H. Frisby, and M. Hoclet, Chem. Phys. **97**, 365-377, (1985).

50. S. Garoff, H. W. Deckman, J. H. Dunsmuir, M. S. Alvarez and J. M. Bloch, J. Physique **47**, 701-709, (1986).

51. R. M. Nicklow, M. Pomerantz and A. Segmuller, Phys. Rev. B **23**, 1081-1087 (1981).

52. W. Knoll, J. Rabe, M. R. Philpott and J. D. Swalen, Thin Solid Films, **99** 173-179 (1983).

53. C. Naselli, J. P. Rave, J. F. Rabolt, and J. D. Swalen, Thin Solid Films **134** 173-178 (1985).

54. M. Prakash, P. Dutta, J. B. Ketterson, B. M. Abraham, Chem. Phys. Lett. **111**, (4&5), 395 (1984).

55. J. Stöhr, J. L. Gland, and E. B. Kollin, R. J. Koestner, A. L. Johnson, E. L. Muetterties, and F. Sette, Phys. Rev. Lett. **53** (22), 2161 (1984).

56. Y. Jugnet, G. Tourillon, and Tran Minh Due, Phys. Rev. Lett. **56** (17), 1862 (1986).

57. G. G. McLeod, K. Jerrreys, J. M. R. MacAllister, J. Mundell, S. Affrossman and R. A. Pethrick, J. Phys. Chem. Solids, **48** (10), 921-926, (1987).

58. F. M. Pan, P. C. Stair, Surface Science, **177**, 1-13, (1986).

59. P. A. Christensen and A. Hamnett, J. Electroanal. Chem., **242**, 47-62, (1988).

60. D. Harradine and A. Campion, J. Vac. Sci. Technol. A **4** (3), 1467 (1986).

61. D. Gourier, and G. Tourillon, J. Phys. Chem. **90** (22), 5561 (1986).

62. B. A. Sexton, Surface Science **163**, 99-113 (1985).

63. G. Tourillon, E. Dartyge, A. Fontaine, R. Garrett, M. Sagurton, P. Xu, G. P. Willians, Europhys. Lett. **1** (12), 1391-1396 (1987).

64. C. A. Ashley and S. Doniach, Phys. Rev. B, **11**, 1279 (1975).

65. E. A. Stern, D. E. Sayers, and F. W. Lytle, ibid., **11**, 4836 (1975).

66. E. A. Stern, Phys. Rev. B, **10**, 3027 (1974).

67. P. A. Lee and G. Beni, Phys. Rev. B, **15**, 2862 (1977).

68. P. A. Lee and J. B. Pendry, ibid. **11**, 2795 (1975).

69. B. K. Teo and P. A. Lee, J. Am. Chem. Soc., **101**, 2815 (1979).

70. B. K. Teo, P. A. Lee, A. L. Simons, P. Eisenberger and B. M. Kincaid, J. Am. Chem. Soc., **99**, 3854 (1977).

71. P. A. Lee, B. K. Teo and A. L. Simons, ibid, **99**, 3856 (1977).

72. E. Sevillano, H. Meuth, and J. J. Rehr, Phys. Rev. B, **20**, 4908 (1979).

73. Edward A. Stern, in *X-ray Absorption: Principles, Applications, Techniques of EXAFS, SEXAFS and XANES*, K. C. Koningsberger and R. Prins (Eds.) Wiley-interscience, Chemical Analysis, **92**, 21, (1988).

74. E. A. Stern, in *X - ray absorption*, D. C. Koningsberger and R. Prins (Eds.) John Wiley & Sons, 1988, p. 45.

75. J. Stöhr, K. Baberschke, R. Jaeger, R. Treichler, S. Brennan, Phys. Rev. Lett. **47**, 381 (1981).

76. J. Stöhr and R. Jaeger, Phys. Rev. B, **26**, 4111 (1985).

77. P. J. Durham, J. B. Pendry, and C. H. Hodges, Computer Physics Communications **25**, 193-205, (1982).

78. P. J. Durham, J. B. Pendry and C. H. Hodges, Solid State Communications, **38**, 159-162.

79. J. B. Pendry, Comments Solid State Phys. **10** (6), 219-231 (1983).

80. J. F. Morar, F. J. Himpsel, G. Hollinger, G. Hughes, and J. L. Jordan, Phys. Rev. Lett. **54**, 1960 (1985).

81. J. A. Horsley, J. Chem. Phys. **76**, 1451 (1982).

82. J. Stöhr, and D. A. Outka, J. Vac. Sci. Technol. A **5** (4), 919 (1987).

83. R. G. Greenler, R. R. Rahn and J. P. Schwartz, *J. Catal.*, **23**, 42 (1971).

84. J. D. E. McIntyre and D. E. Aspnes, Surf. Sci., **24**, 417 (1971).

85. M. J. Diagnam, B. Rao, M. Maskovits and R. W. Stobie, Can. J. Chem. **49**, 1115 (1971).

86. E. B. Wilson Jr., J. C. Decius, and P. C. Cross, in *Molecular Vibrations*, New York, McGraw Hill Book Co., Inc., 1955.

87. J. L. Koening, in *Applied Infrared Spectroscopy* Ed. by D. N. Kendall, Reinhold, 1966, p. 247.

88. N. W. Ashcroft and N. D. Mermin, Solid State Physics, Holt, Rinehart and Winston, 1976, Chapt. 6.

89. I. K. Schüller, Phys. Rev. Lett. **44**, 1597 (1980).

90. W. Lowe, T. Barbee, Jr., T. H. Geballe, and D. B. McWhan, Phys. Rev. B **24**, 6193 (1981).

91. D. B. McWhan, in *Synthetic Modulated Structures*, Academic Press, PP. 43-74 (1985)

92. J. W. Lynn, J. K. Kjems, L. Passell, A. M. Saxena, and B. P. Schoenborn, J. Appl. Cryst. **9**, 454 (1976).

93. J. E. Hilliard, in *Modulated Structures* (J. M. Cowley, J. B. Cohen, M. B. Salamon, and B. J. Wuensch, eds.), p. 407. AIP Conf. Proc. 53, Amer. Instl. Phys. New York, 1979.

94. E. M. Gyorgy, D. B. McWhan, and J. R. Dillon, Jr., L. R. Walker, and J. V. Waszczak, Phys. Rev. B **25**, 6739 (1982).

95. C. Kittel, Introduction to Solid State Physics, 5th ed., Wiley, 1976, p. 64.

96. R. H. Tredgold, Rep. Prog. Phys. **50**, 1609-1656 (1987).

97. J. M. Chen, X. Q. Yang, D. Chapman, M. Nelson, T. A. Skotheim, S. N. Ehrlich, R. B. Rosner and M. F. Rubner, in press.

98. S. Allen, R. A. Hann, S. K. Gupta, P. F. Gordon, B. D. Bothwell, I. Ledoux, P. Vidakovic, J. Zyss, P. Bobin, E. Chastaing and J-C Dubois, SPIE Vol. 682, Molecular and Polymeric Optoelectronic Materials: Fundamentals and Applications (1986), p.97

99. H. Nakahara, K. Fukuda, and M. Sato, Thin Solid Film, **133**, 1-10 (1985).

100. M. Brown, R. E. Peierls and E. A. Stern, Phys. Rev. B **15**, 738 (1977).

101. C. L. Spiro, J. Wong, F. W. Lytle, R. B. Greegor, D. H. Maylotte and S. H. Lamson, Fuel **65**, 327 (1986).

102. J. Stöhr, D. A. Outka, K. Baberschke, D. Arvanitis and J. A. Horsley, Phys. Rev. B **36**, 2976 (1987).

103. E. Weiss, H. Alsdorf, H. Kuhr and H. F. Grutzmacher, Chem. Ber. **101**, 3777 (1968).

104. L. Y. Hsu and C. E. Nordman, Acta Cryst. C **39**, 690 (1983).

105. E. Weber and F. Vögtle, in *Topics in Current Chemistry*, edited by F. L. Boschke *et al.* (Springer-Verlag, Berlin, 1981), Vol. 98, p. 1.

106. J. Wong, F. W. Lytle, R. P. Messmer and D. H. Maylotle, Phys. Rev. B **30**, 5596 (1984).

107. J. Petiau and F. Calas, in *EXAFS and Near Edge Structure*, Vol. 27 of *Springer Series in Chemical Physics*, edited by A. Bianconi *et al.* (Springer-Verlag, Berlin, 1983), p. 135.

108. A. Balzarotti, in Ref. 107, p. 144.

109. M Gorecki, R. Andreani, C. Berthier, M. B. Armand, M. Mali, J. Roos and D. Brinkmann, Solid State Ion. **18**, 295 (1986).

110. G. Tourillon, S. Raaen, T. A. Skotheim, M. Sagurton, P. Xu, G. P. Williams, Surf. Sci. **184**, L345, (1987).

111. M. Sugi, Journal of Molecular Electronics, **1**, 3-17 (1985).

112. C. Naselli, J. D. Swalen, and J. F. Rabolt, J. Chem. Phys. **90** (7), 3855 (1989).

113. M. R. Buhaenko, M. J. Grundy, R. M. Richardson, and S. J. Roser, Thin Solid Films, **159** 253-256 (1988).

114. S. Garoff, H. W. Deckman, J. H. Dunsmuir, M. S. Alvarez and J. M. Bloch, J. Physique **47**, 701-709, 1986.

115. D. L. Allara and J. D. Swalen, J. Phys. Chem. **86**, 2700 (1982).

116. X. Q. Yang, J. M. Chen, P. D. Hale, T. Inagaki, T. A. Skotheim, Y. Okamoto, L. Samuelsen, S. Tripathy, M. L. denBoer, in press.

117. A. P. Hitchcock, J. A. Horsley and J. Stöhr, J. Chem. Phys. **85**, 4835 (1986).